

## Evaluation of chemistry and climate models using measurements and data assimilation

**Citation for published version (APA):**

Jeuken, A. B. M. (2000). *Evaluation of chemistry and climate models using measurements and data assimilation*. [Phd Thesis 1 (Research TU/e / Graduation TU/e), Applied Physics and Science Education]. Technische Universiteit Eindhoven. <https://doi.org/10.6100/IR534235>

**DOI:**

[10.6100/IR534235](https://doi.org/10.6100/IR534235)

**Document status and date:**

Published: 01/01/2000

**Document Version:**

Publisher's PDF, also known as Version of Record (includes final page, issue and volume numbers)

**Please check the document version of this publication:**

- A submitted manuscript is the version of the article upon submission and before peer-review. There can be important differences between the submitted version and the official published version of record. People interested in the research are advised to contact the author for the final version of the publication, or visit the DOI to the publisher's website.
- The final author version and the galley proof are versions of the publication after peer review.
- The final published version features the final layout of the paper including the volume, issue and page numbers.

[Link to publication](#)

**General rights**

Copyright and moral rights for the publications made accessible in the public portal are retained by the authors and/or other copyright owners and it is a condition of accessing publications that users recognise and abide by the legal requirements associated with these rights.

- Users may download and print one copy of any publication from the public portal for the purpose of private study or research.
- You may not further distribute the material or use it for any profit-making activity or commercial gain
- You may freely distribute the URL identifying the publication in the public portal.

If the publication is distributed under the terms of Article 25fa of the Dutch Copyright Act, indicated by the "Taverne" license above, please follow below link for the End User Agreement:

[www.tue.nl/taverne](http://www.tue.nl/taverne)

**Take down policy**

If you believe that this document breaches copyright please contact us at:

[openaccess@tue.nl](mailto:openaccess@tue.nl)

providing details and we will investigate your claim.

# Evaluation of chemistry and climate models using measurements and data assimilation

PROEFSCHRIFT

ter verkrijging van de graad van doctor aan de Technische Universiteit Eindhoven, op gezag van de Rector Magnificus, prof.dr. M. Rem, voor een commissie aangewezen door het College voor Promoties in het openbaar te verdedigen op woensdag 10 mei 2000 om 16.00 uur

door

**Adriaan Bernardus Marie Jeuken**

geboren te Venlo

Dit proefschrift is goedgekeurd door de promotoren:

prof.dr. H. Kelder  
en  
prof.dr. J. Lelieveld

Copromotor:  
dr.ir. F. Dentener

Foto omslag: Leif Rustand  
Druk: Universiteitsdrukkerij Technische Universiteit Eindhoven

CIP-DATA            LIBRARY TECHNISCHE UNIVERSITEIT EINDHOVEN

Jeuken, Ad

Evaluation of chemistry and climate models using measurements and data  
assimilation,-

Ad Jeuken,-

Koninklijk Nederlands Meteorologisch Instituut (KNMI),-

Technische Universiteit Eindhoven, 2000, - Proefschrift -

ISBN 90-386-0987-6

NUGI 819

Trefw.: ozon / aerosol / data-assimilatie / turbulent transport / natte depositie

Subject headings: ozone / aerosol / data assimilation / turbulent transport / wet  
deposition

# Contents

<b>1</b>	<b>Introduction</b>	<b>1</b>
1.1	Background . . . . .	1
1.2	Global models in atmospheric chemistry and climate research . . . . .	3
1.3	Measurements and model evaluation . . . . .	6
1.4	Data assimilation . . . . .	8
1.5	This thesis . . . . .	9
<b>2</b>	<b>Assimilation of meteorological analyses in a global climate model for the purpose of model validation</b>	<b>11</b>
2.1	Introduction . . . . .	11
2.2	Model Description . . . . .	12
2.3	Newtonian Relaxation . . . . .	13
2.3.1	Technique . . . . .	13
2.3.2	Choice of Relaxation Coefficients . . . . .	13
2.3.3	Influence on Model Physics . . . . .	14
2.4	Description of Method and Experiments . . . . .	15
2.4.1	Implementation in ECHAM . . . . .	15
2.4.2	ECMWF Data . . . . .	15
2.4.3	Experiments . . . . .	17
2.5	Results . . . . .	18
2.5.1	Agreement with Basic Observed Quantities . . . . .	19
2.5.2	Comparison of Derived Quantities . . . . .	21
2.5.3	Influence on the Model Physics . . . . .	23
2.6	Discussion and Conclusions . . . . .	27
2.7	Outlook . . . . .	28
<b>3</b>	<b>Assimilation of total ozone satellite measurements in a three-dimensional tracer transport model</b>	<b>29</b>
3.1	Introduction . . . . .	29
3.2	Assimilation Method . . . . .	32
3.3	Transport Model Description . . . . .	34
3.4	Chemistry Parameterization . . . . .	35
3.5	TOVS Observation Errors . . . . .	36
3.6	Horizontal Error Covariance . . . . .	37
3.7	Vertical Redistribution of the Ozone Analysis Increments . . . . .	39
3.8	Ozone Column Results . . . . .	41

---

3.9	Ozone Profile Results . . . . .	43
3.10	Discussion and Conclusions . . . . .	46
3.11	Outlook . . . . .	47
<b>4</b>	<b>Evaluation of vertical mixing and scavenging in a global tracer transport model using measurements of <math>^{222}\text{Rn}</math> and <math>^{210}\text{Pb}</math></b>	<b>49</b>
4.1	Introduction . . . . .	49
4.2	Parameterization of sub-grid scale vertical turbulent transport . . . . .	50
4.2.1	Limitations of the available meteorological data . . . . .	51
4.2.2	Vertical diffusion formulation . . . . .	54
4.2.3	Results . . . . .	56
4.3	Scavenging . . . . .	62
4.3.1	$^{210}\text{Pb}$ simulations . . . . .	66
4.4	Conclusions and Outlook . . . . .	72
<b>5</b>	<b>Modeling the global sulfur cycle with a global chemistry transport model and comparison with measurements</b>	<b>75</b>
5.1	Introduction . . . . .	75
5.2	Model description . . . . .	78
5.2.1	Chemistry . . . . .	78
5.2.2	Aerosol equilibrium model . . . . .	79
5.2.3	Emissions . . . . .	81
5.2.4	Dry deposition . . . . .	81
5.2.5	Wet scavenging . . . . .	82
5.2.6	Meteorological data . . . . .	83
5.3	Results . . . . .	84
5.3.1	Budgets and monthly averages . . . . .	84
5.3.2	Profiles . . . . .	88
5.3.3	Simulation of aerosol components and $\text{SO}_2$ for Europe . . . . .	92
5.4	Comparison of the simulated AOD with satellite measurements . . . . .	100
5.4.1	Satellite data . . . . .	101
5.4.2	Modeling the aerosol optical depth . . . . .	101
5.4.3	Results . . . . .	103
5.5	Discussion, conclusion and outlook . . . . .	105
<b>6</b>	<b>Conclusions and Outlook</b>	<b>111</b>
	<b>Bibliography</b>	<b>117</b>
	<b>Samenvatting</b>	<b>129</b>
	<b>Nawoord</b>	<b>133</b>
	<b>Curriculum Vitae</b>	<b>135</b>

# Chapter 1

## Introduction

### 1.1 Background

The composition of the atmosphere changes in time and space on a wide variety of scales. Much of the variability is due to natural influences. As a result of human activity, closely linked to economic development and population growth, mankind increasingly contributes to changes in the composition of the earth's atmosphere. The growing energy consumption, land use changes and industrialization cause an increase in the emission of the greenhouse gases like  $\text{CO}_2$ ,  $\text{CH}_4$  and  $\text{N}_2\text{O}$ . Also emissions of nitrogen oxides and carbon monoxide have reached higher levels than ever before. By means of the oxidation of  $\text{CH}_4$  and  $\text{CO}$  in the presence of  $\text{NO}_x$  a significant increase in ozone production takes place in the troposphere [Crutzen, 1973].

Ozone is an important constituent in the troposphere as well as in the stratosphere. In the stratosphere it absorbs a large part of the harmful UV radiation thus protecting life on earth. The drastic impact of anthropogenic emissions on the atmospheric composition became evident with the discovery of the ozone hole over Antarctica. Ozone destruction turned out to be the result of anthropogenic emissions of chlorofluorocarbons (CFC's). In the troposphere high levels of ozone can have a detrimental effect on human health and the vegetation. Moreover, ozone plays a controlling role in the oxidation capacity of the atmosphere because ozone and its photochemical derivative, OH, are the major oxidants for most reduced gases. Another aspect of ozone is the contribution to the radiation balance in the longwave part of the spectrum. Because of its strong absorption at  $9.6 \mu\text{m}$  within the so-called atmospheric window, ozone is an effective greenhouse gas, particularly in the upper troposphere where the temperature is low [Wang *et al.*, 1986]. Radiative forcing is often used as a measure for the effect of a change in concentration of an atmospheric constituent on climate. It is defined as the net radiative flux change at tropopause level [van Dorland, 1999]. The radiative forcing of tropospheric ozone is estimated at around  $0.4 \text{ W/m}^2$ , which is about 30% of the estimated value for the increase in  $\text{CO}_2$  [IPCC, 1995]. The increase of greenhouse gases is responsible for the enhanced greenhouse effect, i.e. the warming of the earth's surface and lower atmosphere due to a positive radiative forcing. The climate response to changes in atmospheric composition changes with altitude. For example a decrease of stratospheric ozone leads to a local decrease in UV absorption

and thus to a local cooling.

In particular CO<sub>2</sub> has received public attention, because of its large effect and its direct relation with energy use. However, many other species also contribute significantly. In order to understand and assess climate change, all contributions, natural and anthropogenic, positive and negative radiative forcings need to be investigated and their uncertainties should be assessed.

A major source of uncertainty is the effect of atmospheric aerosols. Atmospheric aerosols are all the particles in the atmosphere larger than a few nanometers and smaller than cloud droplets from various origin and with various composition [Veefkind, 1999]. Major natural sources of aerosols are: volcanic eruptions emitting sulfur dioxide which is chemically converted into sulfate aerosols, the production of sea-spray due to the interaction of ocean waves and wind and the production of mineral dust particles by wind erosion. The latter source is not strictly natural since erosion might be enhanced by human activities like deforestation. Other natural and anthropogenic aerosol sources are forest and savannah fires producing soot particles. Fossil fuel use and biomass burning are other anthropogenic sources of soot particles. From anthropogenic emissions of sulfur dioxide, nitrogen oxides, ammonia and volatile organic compounds, secondary aerosols are produced, through chemical reactions forming different combinations of sulphate, nitrate, ammonium and various organic condensates. Especially about this latter fraction little is known yet. Aerosols can be present in different states of mixing, anything between a pure externally mixed aerosol (e.g. pure sulfate) or a complete internally mixed aerosol (e.g. a homogeneous mix of all aerosol substances).

There are two ways in which aerosols affect the radiation balance of the atmosphere. The direct effect of aerosols is caused by scattering and/or absorption of sunlight. The direct radiative effect of aerosol therefore strongly depends on the size distribution and chemical composition of the aerosol population. For sulfate this effect is estimated to be negative and to lie in the range from -0.5 to -1.2 W/m<sup>2</sup> [IPCC, 1995]. Soot increases lead to a positive forcing. The second effect of aerosols on the radiation balance is indirect through the formation of clouds. This indirect effect acts in two different ways. Aerosols serve as condensation nuclei (CCN) for cloud droplets. An increase in CCN will lead to an increase in cloud droplet number and, with the same amount of water available, this leads to clouds with more but smaller droplets. These clouds scatter relatively more solar radiation back to space [Schwartz, 1996]. Due to the smaller droplets precipitation is less effectively produced resulting in a longer cloud lifetime [Albrecht, 1989]. The magnitude of the indirect radiative effect is very uncertain. Therefore, IPCC gives a value only for the uncertainty, ranging from 0 to -1.5 W/m<sup>2</sup>, indicating that these indirect effects might be very important.

Anthropogenic emissions of aerosols and aerosol precursors have increased rapidly over the last century. Whereas over the last two decades there has been a decrease in Europe and the United States, emissions are still increasing in the developing countries, like for example China and India.

In order to estimate the effect of the changes in radiative forcing on climate, the climate research community has developed general circulation models (GCMs). These models are based on the description of the state of the atmosphere from first principles. These climate models play a key role in assessments of the effects of anthropogenic emissions on climate. Therefore they should be carefully tested and evaluated with respect to their ability to simulate climate and its variability.

## 1.2 Global models in atmospheric chemistry and climate research

Models merely provide a limited, simplified description of reality. However, models can help gaining insight in the interaction between variables and processes in the real atmosphere. Therefore, models are important tools for supporting research on major scientific questions in atmospheric chemistry and climate research.

A wide range of models is used within the climate research community, ranging from energy balance models to the complex GCMs, from detailed process models to statistical models, from 0-dimensional to 3-dimensional models and from local area to global models. Depending on the spatial and temporal scale and the nature of the studied atmospheric phenomenon, different models will be appropriate. For example to understand a chemical reaction mechanism, a chemical box-model may provide good insight. However, if one would like to quantify the influence of a chemical reaction on the global ozone budget a global chemistry transport model (CTM) will be required.

Understanding processes is the first step. Quantifying the effect of a process is the next step. Since the climate problem is by definition a global problem, only these global models can be used to obtain reliable predictions for future climate. Then again, the GCM should represent all relevant processes acting on climate in sufficient detail. On the other hand the more complex the model, the more difficult it is to really understand the results, to see where the key uncertainties lie and to pinpoint the weak parts that need to be improved. Therefore, a whole range of models is needed to understand and predict the climate in a more reliable way. First of all, detailed process studies are needed in order to gain better understanding or new insights. Then, in a second step, these processes should be incorporated in the most optimal way in global models. A basic requirement of global chemistry and climate models is that they should be able to simulate the present-day and past composition of the atmosphere and climate.

### GCMs

In a GCM the basic fluid mechanical equations, that is the equation of motion, the equation of conservation of energy and the equation of conservation of mass, are solved usually in a spherical coordinate-pressure system. With these equations the evolution of the dynamical atmospheric variables wind, temperature and pressure can in principle be calculated. A separate module describes the conversion of solar and terrestrial radiative energy to heat in the atmosphere and at the earth's surface. Due to the strong gradient in solar radiation from equator to pole this is the main process that drives the global circulation. Another module is needed to describe the condensation and evaporation processes of moisture, which results in local warming or cooling rates.

The basic equations have to be solved numerically. This is done at a limited number of discrete intervals in space (a grid) and time. Consequently motions smaller than the grid size can not be solved explicitly. In the earth's atmosphere the transport and other processes in convective clouds and turbulent transport close to the surface are the most important examples of these unresolved motions. In GCMs these processes



are parameterized based on resolved quantities.

Starting from realistic initial conditions a GCM can describe the evolution in time and space of wind, temperature, moisture and clouds. In numerical weather prediction (NWP) GCMs are used to calculate the weather several days ahead. The initial conditions are crucial in NWP. This so-called analysis is provided by a data assimilation system (see section data assimilation) in which a “best guess” of the actual situation is created from various meteorological observations and a short term model forecast. When a GCM is used for climate simulations (of typically several years) it is often referred to as a climate model. Now, not the initial conditions, but long-term forcings, such as the energy input from the sun, the increase of CO<sub>2</sub> and the atmosphere-ocean interactions are crucial.

To be able to estimate the influence of changes in atmospheric trace gases and aerosols on climate, the transport, sources, sinks and trends of these constituents have to be included in GCMs. Interactions between the included constituents and atmospheric processes have to be included in order to calculate couplings with climate. For instance, for aerosols and ozone the absorption and scattering of solar and terrestrial radiation should be included. In addition, for aerosols the effect on clouds should be incorporated as well. Since a GCM without any additional chemical tracers already requires much computing power, it is clear that by including complex chemical systems we soon face the limits of our computer capacity, especially when simulations are made over many years. In practice, this means that only short-term simulations at relatively low resolutions are done or that chemical systems are considerably simplified. Until now only a few long-term climate simulations have been done to investigate the effects of projected increases of constituents other than CO<sub>2</sub> [e.g. *Roeckner et al.*, 1998; *Haywood et al.*, 1997; *Mitchell et al.*, 1995].

## CTMs

Chemical tracer transport models (CTMs) were developed for simulating global atmospheric chemistry only. Instead of calculating the meteorology on-line as is done in a GCM, in a CTM the meteorological fields are prescribed. This input meteorology (e.g. windfields to advect tracers, temperatures to calculate reaction rates) usually is taken from archived analyses from NWP-centers. Since the meteorological fields have been calculated by another model, CTMs are often termed “off-line” models. Whereas in a GCM many equations have to be solved, in a CTM basically only the chemical continuity equation [*Brasseur*, 1999] is solved:

$$\frac{\partial \mu}{\partial t} = -\vec{v} \cdot \vec{\nabla} \mu + \left\langle \frac{\partial \mu}{\partial t} \right\rangle_{conv} + \left\langle \frac{\partial \mu}{\partial t} \right\rangle_{diff} + \mathbf{S} \quad (1.1)$$

with  $\mu$  the tracer mixing ratio which is advected by the three-dimensional wind field  $\vec{v}$  and transported by parameterized convection and turbulent diffusion.  $\mathbf{S}$  is the net source term which can be subdivided in emissions, chemical production or destruction, the loss of a tracer by precipitation scavenging processes and the loss of a tracer by dry deposition at the surface,

$$\mathbf{S} = S_{emis} + S_{chem} + S_{scav} + S_{depo} \quad (1.2)$$

Depending on the complexity of the chemical schemes current CTMs may model the chemistry of a few to about 100 different tracers. Since many intermediate products

or radicals have lifetimes shorter than the model transport time step (typically one hour), these do not need to be transported. Typically, about 50% of the tracers in a CTM is transported.

Since they have quite different chemical regimes, tropospheric and stratospheric chemistry is usually simulated in separate CTMs. In simulating smog episodes mostly regional CTMs are used which vertically extend till the middle troposphere or top of the boundary layer only. When the full atmosphere is not entirely contained in the model boundary conditions need to be specified. For example, for studies of tropospheric ozone the magnitude and the spatial and temporal variation in the ozone flux from the stratosphere needs to be imposed. Often this is achieved by prescribing climatological ozone concentrations (e.g. derived from satellite observations) at a fixed level in the lower stratosphere and letting the model calculate the downward flux [Lelieveld and Dentener, 2000].

### GCMs versus CTMs

GCMs and CTMs partly have a different aim but are also often used for the same purpose: the simulation of global atmospheric chemistry. To list the main differences, advantages and disadvantages:

- The use of a CTM is restricted to the calculation of transport source and sink processes of tracers. In a GCM the coupling between chemistry and climate can be studied. For instance the changes in the radiation balance and in cloud droplet number concentrations caused by aerosols can only be studied with a GCM.
- Since meteorological analyses are used as input, CTMs give a good description of the observed state of the atmosphere so that it is possible to compare model output with instantaneous measurements, e.g. from field campaigns. However, by constraining the GCM with meteorological analyses using a relaxation technique, this is, with some restrictions, also possible for a GCM [Jeuken *et al.*, 1996]. This application is described in Chapter 2.
- A CTM needs less computer resources, since the “meteorology” does not have to be calculated. Because of the lower costs, more complex chemical simulation can be done. On the other hand the large amount of input data for a CTM requires a huge storage capacity. With computer speed increasing more rapidly than storage capacity the advantage of computer costs of CTMs over GCMs might disappear.
- The data time step for a CTM is limited by the availability of meteorological analyses. These fields are available typically every 6 hours. This might be insufficient for some processes with a strong diurnal cycle (see Chapter 4).
- Because of the lower complexity a CTM is easier to handle by an individual researcher or a small research group.

Currently, GCMs and CTMs complement each other well. Depending on if the issue is climate or chemistry related, either one has to be used. In recent years, hybrid versions in between GCMs and CTMs have also been developed. In some CTMs the

hydrological cycle is calculated on-line, instead of reading in cloud and precipitation fields [Rasch *et al.*, 1997]. This saves considerable storage space. The earlier mentioned relaxation method, which couples a GCM with meteorological analyses, also results in a sort of hybrid version, since the GCM is driven by off-line calculated meteorological fields.

### 1.3 Measurements and model evaluation

Measurements provide us with information about the current or past state of the atmosphere and about long-term trends. An important example of the latter is the observed decrease of stratospheric ozone. Measurements of atmospheric quantities are also necessary to evaluate the performance of chemistry and climate models. For this purpose, ideally, measurements would need to be available in each grid box, for each timestep and for each model variable. The reality is, however, far away from this ideal situation. Because they are usually complex and expensive, measurements are limited in time and space. Also, not all possible model variables can be adequately measured. It is fair to say that climate research is strongly “observation limited” and that this is particularly the case for chemical variables. For chemical variables we distinguish between measurements from:

- Monitoring networks
- Dedicated campaigns
- Satellites
- Laboratory

To begin with the latter, in laboratories chemical mixtures are analyzed, reaction rates are measured and optical properties of gases and aerosols are determined. The information obtained from these measurements is often used as input for chemical models or retrieval algorithms for satellite measurements.

#### Monitoring networks

At a number of surface stations around the world measurements are performed of key climate components like CO<sub>2</sub>, CH<sub>4</sub>, CFC's, N<sub>2</sub>O and O<sub>3</sub>. Measurements are performed on a regular basis to monitor trends in emission or chemical production. Networks for climate monitoring are the ALE/GAGE (Atmospheric Lifetime Experiment/Global Atmospheric Gases Experiment) and NOAA CMDL (Climate Monitoring and Diagnostics Laboratory) networks. There are also networks related to air quality monitoring. EMEP (Co-operative program for monitoring and evaluation of the long range transmission of air pollutants in Europe), DOE (US Department of Energy network) and CAPMON (Canadian Air and Precipitation Monitoring Network) are European and North American examples of such networks. O<sub>3</sub>, NO<sub>x</sub>, SO<sub>2</sub>, SO<sub>4</sub> and precipitation chemistry are the most important species that are measured. For aerosols a joint program exists for measuring aerosol optical depths (AOD's) called AERONET. No profiles are measured on a regular basis, with the exception of ozone. In addition, the global distribution of measurement stations is very irregular. There is

a clear North-South gradient in observation density of routine measurements of chemical species as they are mainly done in the industrialized western countries. Especially for highly variable species the density of a network is important.

A well organized network of meteorological measurements already exists. These measurements are used daily to initialize weather forecast models at many institutes around the world. The measurements are obtained from ground-based stations, radio sondes, ships and airplanes and more and more from satellite instruments. The World Meteorological Organization (WMO) has set up the standards for these measurements and exchange between meteorological centres is arranged through the global telecommunication system (GTS). In the chemical measurement community the coordination between measuring institutes is much less well developed. The WMO coordinates measurements of stratospheric ozone and has set up a database for ozone column amounts and ozone sonde measurements. A point of concern is that uncertainty estimates are not systematically provided with the measurement data and that many different methods are used which are not always directly comparable.

### Measurement campaigns

The aim of a measurement campaign is usually to study a particular region and period or process in detail. For example the ACE-1 (Aerosol Characterization Experiment 1) campaign aimed at studying aerosol formation in a remote unpolluted environment while the INDOEX (Indian Ocean Experiment) campaign was focused on transport of air pollution from India over the Indian Ocean. During a measurement campaign usually many different observational platforms are deployed at the same time, like satellites, balloons, aircrafts, ships, lidars and ground stations. In this way a relative complete set of data for the particular region and period can be obtained. Often measurement campaigns are aimed at achieving chemical closure, i.e. obtain a closed budget of all species in a chemical system. Measurement campaigns usually last a few weeks to a few months. Because of the short duration it is often difficult to obtain representative statistical averages from measurement campaigns. For modelers data from measurement campaigns are often difficult to obtain. Often only after a few years the data are publicly available. However data from measurement campaigns are of great importance to modelers. Especially profiles of chemical constituents are hard to get from other sources.

### Satellite measurements

Many measurements of atmospheric constituents from satellite instruments are nowadays available and this will increase in the future. For ozone many instruments have scanned the atmosphere for quite some years (e.g. TOMS, TOVS, GOME). These observations provided valuable information about ozone depletion, atmospheric chemistry and dynamics. Continuity of ozone measurements for the next decade will be guaranteed by GOME2, SCIAMACHY and OMI. The Upper Atmosphere Research Satellite (UARS) has provided a rich set of trace species concentrations (e.g. CFC's, N<sub>2</sub>O, HNO<sub>3</sub>, ClO, HCl) in the middle atmosphere. Not many satellite observations of aerosol properties are available yet. Only in recent years aerosol retrievals have improved considerably [Kaufman, 1995]. Retrieval of the aerosol optical depth is possible from instruments like GOME, AVHRR and ATSR2. Both the retrieval of the

optical depths over land and sea are possible now [Veefkind, 1999].

The most attractive feature of satellite instruments is that they can scan large areas in a short time, so that global coverage can be reached in one or a few days. This is in particular a nice feature with respect to the validation of global models. There are however also limitations. Most satellite instruments, used to detect trace gases or aerosols, are measuring scattered or emitted radiation coming from the earth-atmosphere at different wavelengths. Based on assumed optical properties of the earth's surface and atmospheric constituents, information about the abundance of a constituent can be retrieved. This is an indirect method. The value of satellite retrieved products therefore depends essentially on how well it can be validated against more direct in situ measurements, e.g. from campaigns. In addition the presence of clouds is strongly hampering detection of species in the lower troposphere. Perhaps the strongest limitation of satellite measurements so far is the limited vertical information that can be retrieved for the troposphere. Limb sounders offer the possibility of high-resolution vertical measurements but have a limited horizontal resolution and usually have difficulties in probing the troposphere. Nadir viewing instruments can reach a high horizontal resolution but only have restricted vertical resolution.

### Models versus measurements

There is always the problem of the representativity of the measurements when comparing models and measurements. Observations are usually done at one or a few single locations or times. Global models typically provide grid box averages. In order to be useful for comparison, the location where the measurement has been taken should be more or less representative for the whole volume of a model grid box. Especially for tracers with a short lifetime this criterion is seldomly met.

Chemistry-climate models have developed rapidly over the last 2 decades. Due to increased computer power the resolution has increased considerably, as well as the amount of detail in physical and chemical processes. However, the mismatch between the degree of detail of the model output and the observations necessary for validation is sometimes large. Further development of more sophisticated models will be of limited use until more observations have become available. Therefore there is a real need for more and well-organized measurements.

## 1.4 Data assimilation

Data assimilation goes one step further than simply comparing model and measurements. In data assimilation the most likely distribution of an atmospheric quantity is estimated based on observations and on physical laws that govern the time evolution of the given quantity. The observations can be taken from different sources irregularly distributed in space and time. The physical laws are contained in a model. Both models and measurements contain errors, which are correlated in time and space. Therefore in a data assimilation system model forecasts and measurements are weighted according to their respective error covariance estimates. Unevenly distributed observations in time and space are transported and transformed by the model and can be analyzed at regular time-intervals. Data voids are filled in, and using a good model can result in an analysis error which is significantly smaller than the error

of the measurement itself. In this way model and observation can benefit mutually from each other.

There is a long-term tradition of data assimilation in numerical weather prediction. The high quality of modern NWP would be unthinkable without data assimilation. The skill of weather forecasts has increased considerably over the last decade for a large part due to improvements in data assimilation methods and the processing of increasing amounts of satellite data in the assimilation systems.

Chemical data assimilation is a new topic. In recent years, however, it is getting growing attention [*Lary et al.*, 1995; *Riishøjgaard*, 1996; *Levelt et al.*, 1996]. Measurements of chemical species can be assimilated in both CTMs and GCMs. Satellite measurements are very appropriate for use in chemical data assimilation because of their good temporal and spatial coverage and the large amounts of data. The major advantages of such a system are:

- The information contained in the measurements can be consistently distributed in space and time in this way producing global synoptic maps.
- The information contained in a measurement also influences other model variables via the model equations. An example is the assimilation of ozone in a GCM. By assimilating ozone, the wind fields can be adjusted as well via the inverse transport equations [*Riishøjgaard*, 1996; *Stoffelen and Eskes*, 1999]. In a chemical model assimilated information for one tracer can be transferred to other species via chemical reactions. In this way an extensive chemical scheme can be constrained by measurements of a few key species [*Khattatov et al.*, 1999; *Elbern et al.*, 1997].
- In data assimilation the model is confronted systematically with observations. In this way systematic differences between models are revealed and model errors can be better estimated.
- Since the observation error is an important ingredient for data assimilation, quality control of measurements is an essential part of any assimilation system. By including more than one source of observation for the same model variable, observation error estimates can be improved.
- An interesting application is the combination of retrieval and assimilation within the same model. In retrieval methods, information about atmospheric variables is used, which is often taken from climatologies. Instead of using these climatologies, actual model variables can be used. In the ECMWF NWP model for example. TOVS irradiances are assimilated instead of retrieved temperature profiles. The conversion from irradiances to temperatures is done in the data assimilation itself using information from the model. This leads to a large improvement compared to the old situation where temperatures were first retrieved and then assimilated.

## 1.5 This thesis

The work for this thesis has been carried out within 3 substantially different projects. However, central in all three projects is the focus on the use of measurement data

for model evaluation. Within each of the following chapters the use of observational data to better understand and improve models will be emphasized. Whereas the research described in Chapter 2 and 3 is aimed at developing and improving methods for comparing models and measurements, Chapter 4 and 5 aim at development and improvement of model descriptions of atmospheric processes. Measurements are in these two chapters merely used for evaluating the model changes. In each chapter we want to answer different research questions and measurements are used to assist finding answers to these questions.

In Chapter 2 the possibility is investigated if the Newtownian relaxation method can be used to constrain the ECHAM model (climate model of the Max Planck Institute Hamburg) with meteorological analyses in order to make it possible to compare model output with instantaneous measurements. In this method the meteorological analyses serve as a sort of pseudo observations representing the actual state of the atmosphere. The main questions are: what should be the strength of the relaxation, does the model output indeed improve in comparison with measurements and what will be the influences of the additional model forcing on physical processes?

In Chapter 3 the statistical optimum interpolation (OI) data assimilation method is applied to the chemical tracer transport model TM3 for the assimilation of satellite measured total ozone columns. The main issue is how to assimilate 2-dimensional observations in a 3-dimensional model. Other questions are: do the analyses resulting from the data assimilation indeed present an improvement compared to the original data and model without assimilation? Or what do we learn about model transport and chemistry from systematic errors in the data assimilation. By comparing results from the assimilation with independent satellite measurements and with various ozone sondes we try to answer these questions.

In Chapter 4 major changes to the parameterization of vertical diffusion and precipitation scavenging within the TM3 model are made. Existing methods from other models will be implemented. The question is how these methods can be most optimally used within TM3, making use of the available meteorological data, and secondly if the model changes result in a better simulation of transport and non-chemical removal processes. Various measurements of Radon and Lead are used for this purpose.

Finally in Chapter 5 TM3 is applied for the simulation of the global sulfur cycle. Model results are compared with measurements on various temporal and spatial scales. Satellite measurements of aerosol optical depths are used for the evaluation of spatial patterns in the model aerosol field. The aim in this chapter is to understand the processes that govern the sulfur cycle.

Chapter 2 has been published in JGR 101, 1996 and Chapter 3 in JGR 103, 1999. Part of Chapter 4 has been published as co-author in Tellus 51B, 1999. Another part of Chapter 4 and part of Chapter 5 are in preparation for submission.

## Chapter 2

# Assimilation of meteorological analyses in a global climate model for the purpose of model validation

*Most of this chapter has been adopted from:*

*A. B. M. Jeuken, P. C. Siegmund, L. C. Heijboer, J. Feichter and L. Bengtsson, On the potential of assimilating meteorological analyses in a global climate model for the purpose of model validation, J. Geophys. Res., 101, 16,939-16,950, 1996*

### 2.1 Introduction

The four-dimensional data assimilation (FDDA) based on “nudging” or Newtonian relaxation is a method, which dynamically couples various observed variables using a general circulation model (GCM). Terms are added to the prognostic equations to force the model towards the observed state. FDDA was originally developed to insert synoptic data like satellite or aircraft measurements in numerical weather prediction (NWP) systems. It is widely used by both the research and operational meteorology communities for application in data assimilation systems in weather forecast models [Hoke and Anthes, 1976; Davies and Turner, 1977; Lyne et al., 1982; Ramamurthy and Carr, 1987; Krishnamurti et al., 1991]. In addition, FDDA is also a powerful tool to analyze the behavior of the atmosphere and to derive variables which cannot be observed.

A new application of Newtonian relaxation could be the validation of physical parameterization schemes of a GCM, whereby the large-scale component of the modeled circulation is adjusted towards meteorological analyses. Climate studies are performed using general circulation models which are integrated over long periods, typically 30 years, to obtain statistically significant averages. Such models are evaluated by comparing the model’s multiyear averages and interannual variability with synoptic observations. But for many meteorological parameters calculated by the



model, like cloud cover or cloud liquid water, no long-term observations are available. As the cloud feedback is a key issue for climate dynamics [Cess *et al.*, 1990] there is a real need to carefully evaluate the parameters of the hydrological cycle. Moreover, due to an increasing interest in recent years on the possible impact of enhanced emissions of radiatively active gases and aerosol precursors on climate, chemistry modules have been implemented in GCMs to study feed back mechanisms between climate and atmospheric chemistry. As the database of chemical species is much smaller than for meteorological parameters, validation of the model's chemistry is only possible for short periods like during measurement campaigns where sufficient observations are available. To be able to use data covering shorter periods for model validation, one could apply the relaxation to force a GCM to simulate a specific episode.

The main objective of this study is to develop a practical and simple method which can be applied in validating climate models. Use is made of the above mentioned Newtonian relaxation technique. We have investigated which model variables should be adjusted toward the analyses and what time scale of the forcing should be applied for the different variables.

In section 2.2 the model used for our study is described. In section 2.3, a theoretical overview is given of the various aspects of the "nudging" method which are important for our application, and in section 2.4 the currently used implementation of the method and the setup of the experiments are described. In section 2.5 the results of the experiments are presented.

## 2.2 Model Description

The GCM used in the present study, the Hamburg climate model ECHAM, is a general circulation model based on the numerical weather prediction model of the European Center for Medium-Range Weather Forecasts (ECMWF) with a new physical package adapted for climate studies [Roeckner *et al.*, 1993]. The prognostic variables of ECHAM are the vorticity, the divergence, the temperature, the logarithm of surface pressure, water vapor, cloud water, and several chemical species. For its representation of the dynamic fields, the model adopts expansions in terms of spherical harmonics with triangular truncation at a specified wavenumber. Nonlinear and physical terms are calculated on a Gaussian grid. Positive definite quantities, like water vapor, cloud liquid water and chemical species, are advected by a semi-Lagrangian scheme [Rasch and Williamson, 1990]. The model can be run with the resolutions T21 ( 500 km), T42 ( 250 km), and T106 ( 100 km). Discretization in the vertical is done by using a hybrid coordinate system with 19 levels with its uppermost level at about 30 km. The temporal finite difference scheme is semi-implicit with a time-step of 40 min. (T21), 24 min. (T42), or 12 min. (T106). The radiative transfer model is based on a two-stream method by Fouquart and Bonnel [1980] for the solar part and by Morcrette [1991] for the terrestrial part. The frequency spectrum is separated into two short-wave and six long-wave intervals. The stratiform cloud scheme is based on the approach of Sundquist [1978] who developed a method for including subgrid-scale condensation and cloud formation within the framework of a cloud liquid water transport equation. Convective clouds are parameterized by the mass flux scheme of Tiedtke [1989]. Turbulent exchange in the boundary layer is parameterized by using the Prandtl-Kolmogorov formulation of the eddy diffusivity as a function of the

turbulent kinetic energy (TKE-closure) [*Brinkop and Roeckner, 1995*].

## 2.3 Newtonian Relaxation

### 2.3.1 Technique

The “nudging” method relaxes the model state toward observational data during the assimilation period by adding a non-physical relaxation term to the model equations:

$$\frac{\partial X}{\partial t} = F_m(X) + G(X_{obs} - X) \quad (2.1)$$

Here  $X$  represents any prognostic model variable and  $F_m$  is the model forcing, describing the dynamical and physical processes that determine the evolution of  $X$ . The relaxation term  $G(X_{obs} - X)$  is expressed as the product of the relaxation coefficient  $G$  ( $s^{-1}$ ) and the difference between the observational and the model calculated value of  $X$ . As observational data, both raw observations and analyzed observations can be used.

When using a spectral model, a simple opportunity is offered to exclude smaller scales from relaxation, by not adjusting the higher wave number spectral components. This can be particularly helpful in high-resolution experiments when the smaller-scale variations are for a large part determined by the physical or parameterized quantities and are not represented by the observations.

Observational data are generally not available for each model time step. To obtain data for every model time step, data have to be interpolated. The simplest way to do this is linear interpolation. As mentioned by *Brill et al.* [1991], such an interpolation is allowed for data intervals up to 6 hours. It should be realized that for higher-resolution experiments, linear interpolation becomes more questionable since, as mentioned before, more smaller temporal scales are resolved. This is another reason to restrict the relaxation to low-order spectral components.

### 2.3.2 Choice of Relaxation Coefficients

The choice of the right value of  $G$  forms a main difficulty of the “nudging” technique [*Stauffer and Seaman, 1990*]. If  $G$  is chosen too large the relaxation term will dominate the model forcing. In this case, possible dynamical imbalances in the observations may be spuriously amplified. On the other hand, if  $G$  is chosen too small, the observations will have little effect on the solution. Various considerations concerning the choice of  $G$  can be found in literature. *Hoke and Anthes* [1976] suggest that the optimal value should depend on the observational accuracy, the kind of variable being adjusted, and the typical magnitude of the model forcing. This means that  $G$  may vary both in space and time since observational accuracy as well as the magnitude of model forcing vary in space and time. Nevertheless, in most applications the variation of  $G$  in time and space is not taken into account. In some recent studies the values of  $G$  are calculated for each grid point separately using a parameter estimation procedure which makes use of the adjoint equations of the numerical model [*Zou et al., 1992; Stauffer and Bao, 1993*].

Different approaches exist with respect to the choice of the variables to be adjusted. One question is whether to adjust the wind field (and let the mass field adjust to it by

Exp.	$G_T$	$G_D$	$G_{Vo}$	$G_{lnsp}$
0	0.0	0.0	0.0	0.0
1	$1.10^{-4}$	$0.5.10^{-4}$	$1.10^{-4}$	$1.10^{-4}$
2	0.0	$0.5.10^{-4}$	$1.10^{-4}$	$1.10^{-4}$
3	$1.10^{-4}$	0.0	$1.10^{-4}$	$1.10^{-4}$
4	0.0	$0.5.10^{-4}$	$1.10^{-4}$	0.0
5	$1.10^{-5}$	$0.5.10^{-4}$	$1.10^{-4}$	$1.10^{-4}$
6	$1.10^{-5}$	$0.5.10^{-5}$	$1.10^{-5}$	$1.10^{-5}$
7	$1.10^{-3}$	$0.5.10^{-3}$	$1.10^{-3}$	$1.10^{-3}$

Table 2.1: *Specification of the assimilation experiments.  $G_D$ ,  $G_{Vo}$ ,  $G_T$  and  $G_{lnsp}$  are the relaxation coefficients ( $s^{-1}$ ) for divergence, vorticity, temperature and surface pressure respectively.*

the model equations) or to adjust the mass field (and let the wind field adjust to it) or both. *Kuo and Guo* [1989] conclude that simultaneous assimilation of both mass and momentum yields the best results. A second question is whether to adjust the rotational part of the wind field alone or both the rotational and divergent part. The rotational part of the wind is considered to be more important to adjust than the divergent part, for several reasons. The divergent part is relatively poorly observed [*Holopainen*, 1987] and is closely associated with gravity waves. The rotational part of the wind, on the other hand, represents the slow manifold of quasi-geostrophic motion [*Daley and Puri*, 1980]. Quasi-geostrophic theory is capable to describe the evolution of Rossby wave type flow for time scales up to a few days. Adjusting the vorticity field of the model is, therefore, an efficient way to adjust the large-scale flow in the extratropics. In many applications the relaxation coefficient for vorticity is therefore larger than the coefficient for divergence. *Brill et al.* [1991] also adjusted the surface pressure. They argue that adjusting the predicted variables only above the surface can lead to an accumulation of errors at the surface. Adjusting the moisture field in the surface layer to improve the diabatic forcing has been applied by a few investigators [*Douglas and Warner*, 1987; *Krishnamurti et al.*, 1988, 1991; *Brill et al.*, 1991].

Derivation of mathematically optimal relaxation coefficients would require a method similar to the variational approach as used by *Zou et al.* [1992]. Variational methods require, however, huge computer memory and power, which make them impractical to use in a large global model.

### 2.3.3 Influence on Model Physics

As an example to illustrate the influence of relaxation on the parameterized part of the model, we examine the thermodynamic energy equation including a relaxation term:

$$\frac{dT}{dt} = \frac{Q}{c_p} + \omega \frac{\kappa T}{p} + G(T_{obs} - T), \quad (2.2)$$

where the symbols have their conventional meteorological meaning. The symbol  $Q$  denotes the diabatic heating, which mainly consists of the release of latent heat due to the condensation of water vapor, the flux of sensible heat from the Earth’s surface into the atmosphere, and the radiative heating. In the model these heating components are parameterized in terms of the large-scale dynamical quantities, like wind and temperature. Therefore, the relaxation term not only modifies the temperature, but also indirectly modifies the diabatic heating in the model. Without relaxation, a physically consistent balance between the parameterized and the dynamical quantities exists in the model. The relaxation in Equation 2.2, therefore, not only forces the modeled temperature toward the observations, but also hinders the parameterized quantities to reach a balanced state. Similar arguments apply to the equations for momentum and moisture.

This problem is analogous to the spin-up problem in weather prediction models, in which assimilation of observations causes an initial imbalance in the model physics. This imbalance disappears a short time after the assimilation. However, in a setup in which the model is relaxed toward new observational data every time step, there will be a continuous spin-up.

## 2.4 Description of Method and Experiments

### 2.4.1 Implementation in ECHAM

A model integration step (Eq. 2.1) is solved using a semi-implicit finite difference scheme and is carried out in two steps. First, the model forcing  $F_m$  is calculated yielding a new value for prognostic variable  $X_{t+\Delta t}^m$ . Next the relaxation term is calculated:

$$\frac{X_{t+\Delta t} - X_{t+\Delta t}^m}{2\Delta t} = G(X)[X_{t+\Delta t}^{an} - X_{t+\Delta t}] \quad (2.3)$$

in which  $X_{t+\Delta t}^{an}$  are the meteorological analyses of prognostic variable  $X$  to which the model is relaxed.  $G(X)$  is the relaxation coefficient which in the present study depends only on the variable which is relaxed.  $X_{t+\Delta t}$  finally is the value of  $X$  after the assimilation step and can be easily calculated from Equation 2.3.

Since ECHAM is a spectral model assimilation is done in the spectral space. The resolution used in all of the experiments described in this paper is T21. For this coarse T21 model version, all spectral components are equally adjusted. However, one exception has been made: to conserve mass and momentum, the first spectral component, which represents the global average, is not adjusted.

### 2.4.2 ECMWF Data

In our study we have used ECMWF data for two purposes: the assimilation itself and for comparison afterwards with ECHAM model results.

#### Data for Assimilation.

As input data for the assimilation we have used spectral ECMWF first guess fields, which are the 6-hour forecast, of vorticity, divergence, temperature and surface pres-

Variable	Type	Period	Interval	Averaging	Interp
200 hPa zonal wind	FG	6h	6h	no	no
500 hPa geopotential height	FG	6h	6h	no	no
700 hPa specific humidity	FG	6h	6h	3x3 gridcells 3 time steps	no
850 hPa temperature	FG	6h	6h	no	yes
Surface pressure	FG	6h	6h	no	yes
Precipitation	FC	12h-36h	12h	3x3 grid cells	no
Evaporation	FC	12h-36h	12h	3x3 grid cells	no

Table 2.2: *ECMWF Data used for comparison. Type FG (first guess) or FC (forecast), period of forecast, output interval, averaging in time and/or space and vertical interpolation to mean orography have been indicated.*

sure. We have simulated 2 months, January and July 1989, by relaxing the ECHAM model toward the ECMWF analyses for these periods. The model runs have been started from initial files from a January and a July month. The input fields for the relaxation are only available every 6 hours. To obtain data for each model time step, we have linearly interpolated the data in time. We found that cubic spline interpolation did not show any improvement for our application. Before applying the relaxation, the ECMWF data, which originally are in T106 resolution, are truncated to T21. In 1989 the ECMWF model used the same vertical hybrid coordinate parameters as the ECHAM model uses. The orographies used in the two models, however, are different. ECHAM uses a mean orography, whereas the ECMWF model uses an envelope orography in which the sub-grid scale variance is added to the mean orography of a grid box [Simmons, 1987]. Differences between the two may amount to a few hundreds of meters. Since close to the surface the hybrid levels are terrain-following, this means that when data are used over mountainous areas, the levels on which they are valid are different for the ECHAM and the ECMWF model. To avoid errors, caused by these nonmatching orographies, we vertically interpolate.

The following procedure has been applied (M. Hortal, personal communication, 1995): the input spectral ECMWF data are truncated to the desired output resolution and transformed to grid point space, where instead of vorticity and divergence, the wind components are calculated. The input (envelope) orography (grid point data) is interpolated to the desired output resolution, by transforming it to spectral space, next truncating it to the new resolution and then transforming it back to grid point space. Next the desired output (mean) orography is constructed from the high-resolution original U.S. Navy data set. In the new orography we compute the logarithm of the surface pressure from the interpolated data. From this we compute the pressures at the model levels corresponding to the output resolution. Then we interpolate (or extrapolate) the wind components and the temperature linearly in pressure. Finally, we transform the wind components to vorticity and divergence in the spectral space.

Owing to this vertical interpolation, one can expect inaccuracies in areas where the difference between the surface pressure in the envelope and mean orography is

large. One should realize that the ECMWF data used for assimilation can be seen as a good approximation for the observed atmospheric state in data-rich areas. In large parts of the tropics, however, meteorological observations are sparse and the ECMWF data for these areas rather reflect the model prediction than the observations and, therefore, may not be very accurate.

#### Data for Comparison.

The following ECHAM model variables have been compared with the corresponding ECMWF fields (see also Table 2.2: surface pressure, the temperature at 850 hPa, the zonal wind at 200 hPa, and the 500 hPa geopotential height. Further, we compare the specific humidity at 700 hPa. Although this is a prognostic variable and therefore transported by the model resolved large-scale flow, it is mainly determined by parameterized sub-grid scale processes. Therefore we cannot expect perfect agreement between the ECHAM humidity field and the ECMWF data.

When using ECMWF model fields of precipitation and evaporation, one should realize that there is a spin-up in the short-range forecast of these fields. The duration of the spin-up depends on the model and on the area for which the variables are calculated [Krishnamurti *et al.*, 1988], [Arpe, 1991]. Arpe [1991] argues that ECMWF forecasts of daily mean precipitation and evaporation for day 0.5-1.5 provide the best compromise between spin-up and forecast error. He further concludes that for the northern hemispheric extratropics the short-range forecasts of evaporation over the oceans and precipitation are probably accurate estimates of the truth, not only for monthly means but also for the day to day variability. In the tropics and southern hemisphere, the distribution seems realistic but there is a strong spin-up in the data. Therefore we have used the day 0.5-1.5 forecast period when comparing time series at individual grid points. For the comparison of global averages, however, fields should be free of bias and for this purpose we compare the ECHAM fields with a range of ECMWF forecasts up to 3 days.

The grid point values of precipitation and 700 hPa specific humidity and evaporation have been smoothed in space (3x3 grid points) and 700 hPa specific humidity has been also smoothed in time (running average over three intervals of 6 hours each). This filters out much of the quasi-random small-scale variations that otherwise might prevent a useful comparison of the two fields obtained from different parameterizations.

#### 2.4.3 Experiments

Like others [Krishnamurti *et al.*, 1988] we decide by “trial and error” which relaxation coefficients give the best results for our application. A series of assimilation experiments (shown in Table 2.1) has been performed, in which the relaxation coefficients are varied according to physical arguments as described in section 3.2 and within a range observed in literature. Moisture has not been included in our experiments because the moisture field is determined by diabatic processes rather than dynamical processes. An assimilation technique based on dynamical adjustment would therefore not be very beneficial. As outlined in section 2.3.2, the rotational part of the wind is considered most important to adjust. For this reason vorticity has been included in each of the assimilation experiments.

In judging which set of relaxation coefficients would be most useful, we look upon two different aspects: validating model parameterizations or chemistry modules with measurements requires in first instance that the basic flow, temperature, and moisture pattern from which most sub-grid scale parameterizations are derived and which determine transport and reaction rates of chemical tracers, is represented well by the relaxed model.

A second requirement is that the model physics work without too much restrictions imposed by the relaxation. It is desired that the model physics adapt to the, by the relaxation imposed, flow and temperature distribution without being too much suppressed by the relaxation. This aspect is more complicated to investigate. Three different approaches are used: first, the precipitation (convective and large-scale) and evaporation are compared with the corresponding ECMWF fields. Since the ECHAM and ECMWF model use different parameterization schemes, again we may not expect good quantitative agreement. A comparison can, however, be useful to see if the relaxed model produces realistic fields from parameterized subgrid-scale processes. A second approach is to directly compare the forcing of the temperature by parameterized processes with the forcing by relaxation. The distribution of the forcing in time and space is also considered. In this way some qualitative understanding can be gained in where and when the forcing by relaxation could dominate the normal model forcing. A third, more quantitative approach, is the comparison of the vertical exchange of tracers in an undisturbed experiment with a series of relaxation experiments in which the relaxation forcing is systematically increased. The bulk of the vertical exchange of longer-lived tracers from the surface to the free troposphere and from the lower to the upper troposphere is in the model controlled by parameterized processes. The systematic change in the amount of vertically exchanged tracer mass in this approach therefore can be used as a measure for the influence of the relaxation on the model physics.

Comparison between ECHAM produced fields and ECMWF fields has been done using various statistical measures like the anomaly pattern correlation, the tendency correlation, the bias and the root mean squared difference/error (RMSE). The anomaly pattern correlation is calculated as the spatial correlation between the ECMWF and ECHAM anomaly fields. The anomaly is calculated with respect to an ECHAM monthly mean field from a climatological run. The tendency correlation is calculated as the correlation between ECHAM and ECMWF timeseries at individual grid points and gives us some insight in how well ECHAM adjusts in time to the ECMWF data. Also, the RMSE is calculated for time series of individual grid points and provides insight in the magnitude of differences between the two models.

## 2.5 Results

In this section we will address three subjects. First, the agreement between the model simulations and the ECMWF data set for the basic observed quantities (the first five variables in Table 2.1) will be quantified. Second, some ECHAM-derived, parameterized quantities (precipitation and evaporation) will be compared with ECMWF forecasts. Finally, we will investigate the impact of the assimilation on the model's parameterized quantities.

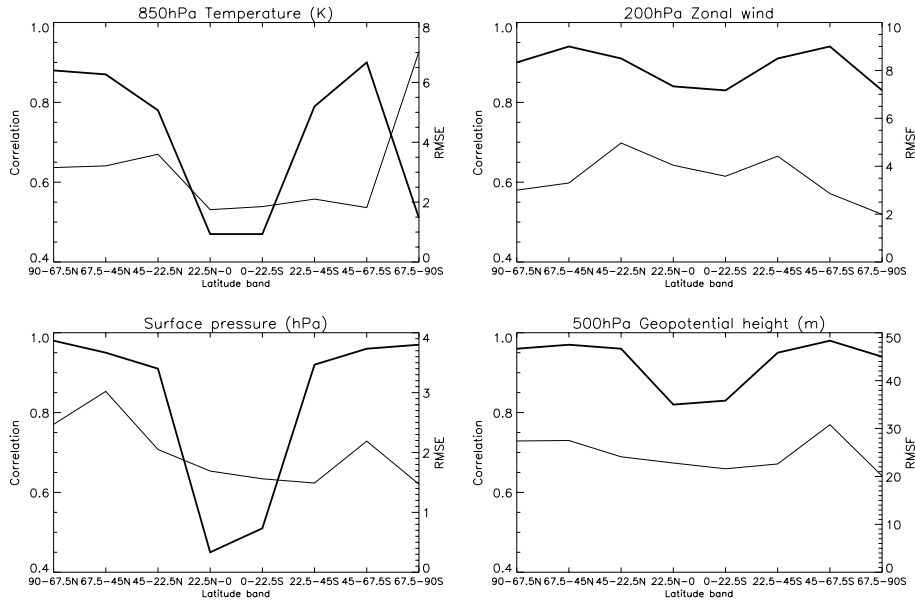


Figure 2.1: Comparison of assimilation experiment 5 and ECMWF first guess fields: Zonal mean tendency correlation (thick line) and root mean squared error (RMSE) (thin line) for January 1989.

### 2.5.1 Agreement with Basic Observed Quantities

As a first indication of what agreement can be obtained, in Table 2.3 the global averaged statistics are presented for the comparison of ECHAM output fields (assimilation experiment 5 from Table 2.1) with corresponding ECMWF fields for January 1989. From these global mean results it appears that ECHAM, when relaxed toward ECMWF analyses, is well capable to reproduce these analyses. As can be seen in Table 2.3, the anomaly pattern correlations are extremely high. This means that the spatial patterns of the ECMWF fields are almost exactly reproduced by the ECHAM simulation. The agreement for the specific humidity is somewhat less; the magnitude of the RMSE is about 25 % of the value of the globally averaged specific humidity. Since, as explained earlier, the specific humidity has not been adjusted in the relaxation experiments and for a large part is determined by the model parameterized moist processes which are different between the two models, this lesser agreement is not surprising. We should, however, consider the spatial variability of the statistical parameters as well. Figure 2.1 gives information about the latitudinal dependence of the tendency correlation and the RMSE. It can be clearly seen that the relaxation technique yields less satisfying results in the tropics than in the extratropics. Tendency correlations generally are much lower in the tropics, particularly for the 850 hPa temperature and surface pressure. The RMSE is not higher in the tropics. In fact for all variables, except the zonal wind at 200 hPa, it is lower in the tropics. Relative to the low temporal variability of the presented variables, the error is larger in the tropics. Figure 2.2 shows the dependence of tendency correlation and the RMSE on the choice of relaxation coefficient. The tropics (between 22.5°N and 22.5°S) and



Variable	Mean	Bias	RMSE	TC	APC
850 hPa temperature (K)	279.183	-0.260	1.203	0.801	0.975
200 hPa zonal wind (m/s)	16.053	-0.004	3.862	0.883	0.975
500 hPa geopotential height (m)	5549.37	18.56	24.18	0.909	0.985
700 hPa specific humidity (g/kg)	3.160	0.238	0.794	0.657	0.680
Surface pressure (hPa)	985.565	0.583	1.911	0.759	0.974

Table 2.3: Statistics for Experiment 5, Global Averages for January 1989. The Bias is calculated as ECHAM-ECMWF and mean values are taken from ECHAM. TC stands for tendency correlation and APC for anomaly pattern correlation

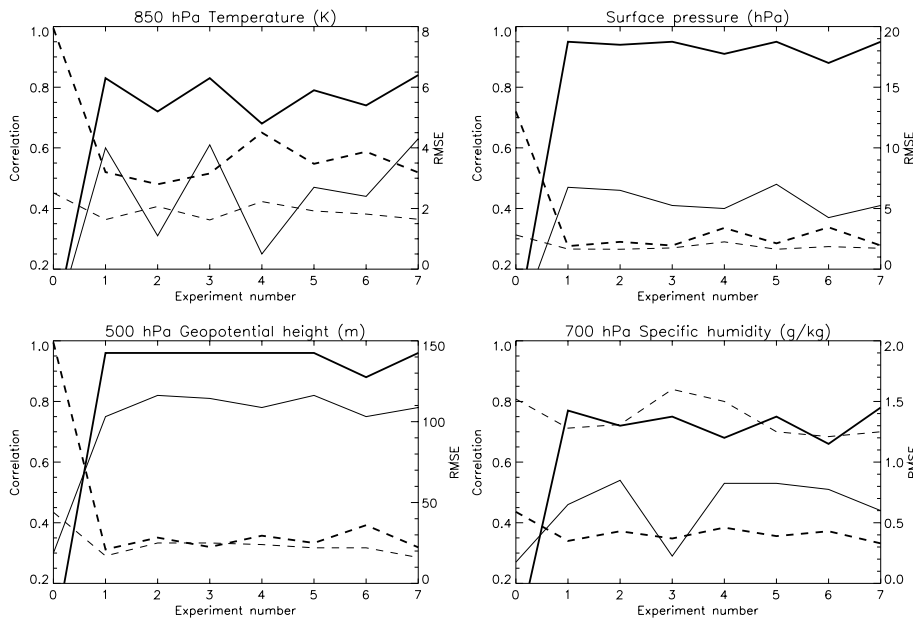


Figure 2.2: Correlation (solid line) and RMSE (dashed line) between ECMWF first guess fields and the assimilation experiments outlined in Table 2.1 for January 1989. Thick lines represent averages over the extratropics and thin lines over the tropics.

extratropics are analyzed separately. Experiment 0 is the control run in which no relaxation has been applied. It can be seen in Figure 2.2 that the results are not very sensitive to the choice of the relaxation coefficients for the range of values applied. The variability among the experiments is low except for the 850 hPa temperature.

Most of this variability for the 850 hPa temperature can be explained by whether or not temperature has been relaxed. In experiment 2 and 4 the temperature has not been included and the relaxation coefficient for temperature has a low value in experiment 5 and 6. These experiments differ significantly from experiments 1, 3, and 7 in which temperature has been relaxed with the same coefficient as vorticity.

For the 500 hPa geopotential height the values of the RMSE and the tendency correlation have about the same value for almost all experiments, except for exper-

iment 6. This experiment has low values for the relaxation coefficients. The only important variable for a realistic simulation of 500 hPa geopotential height seems to be the vorticity. Excluding other variables from assimilation does not influence the results. The same behavior with respect to assimilation experiment is observed for the 200 hPa zonal wind (not shown), with the only exception that the correlations are slightly lower.

Almost the same can be concluded for the surface pressure. Not adjusting the surface pressure (experiment 4) worsens the statistics only slightly. A negative effect of the same order of magnitude can be detected for experiment 6.

The agreement of the ECHAM specific humidity field at 700 hPa with ECMWF data is considerably less than for the other variables shown in Figure 2.2. Adjusting the divergence appears to be important for the humidity field, because not including the divergence in the assimilation (experiment 3) results in a significant increase in RMSE and a decrease of correlation in the tropics.

As was already shown by Figure 2.1, Figure 2.2 again shows that the relaxation technique yields the best results in the extratropics. It also shows that there is hardly any improvement in the RMSE to be observed compared to the control run in the tropics.

For July 1989 (not shown) the results for the basic observed quantities are similar. The moisture field, however, has improved considerably in the tropics. RMSE's have been reduced to values below 1.0 g/kg and the tendency correlation now is similar to the correlation for the extratropics. The change to the Tiedtke scheme [Tiedtke, 1989] as convection scheme of the ECMWF model in May 1989 is probably the reason for this improvement since ECHAM also uses the Tiedtke scheme.

### 2.5.2 Comparison of Derived Quantities

In a similar manner as has been done in previous section, the ECHAM precipitation and evaporation from the different relaxation experiments are compared with the appropriate ECMWF forecasts (see section 4). In Figure 2.3 the dependence of the correlation and RMSE on the choice of relaxation coefficients is shown for evaporation and precipitation. The improvements obtained by assimilation in comparison with the reference experiment are smaller than the improvements seen in section 2.5.1 for the basic observed quantities. The maximum improvements obtained in RMSE are 35 and 50 % for precipitation and evaporation, respectively. Correlations are considerably lower. Differences in statistics between the tropics and extratropics are smaller than diagnosed for the observed quantities. Some important differences among the experiments can be seen. Not adjusting the temperature (experiment 2 and 4) worsens the statistics for both evaporation and precipitation. The difference between the RMSE of experiment 2 and 5, for example, is about 0.4 mm/d and 0.2 mm/d for precipitation and evaporation, respectively. Not adjusting the divergent part of the windfield (experiment 3) has a negative effect on the statistics for both precipitation and evaporation. This is shown most clearly for the precipitation in the tropics. The strong relation between large-scale convergence and convection used in the convection parameterization is probably the reason for this effect. Provided that the ECMWF model output is realistic, we learn from this comparison two things: First, the influence of relaxation on the derived variables in the tropics is beneficial. Second, temperature and divergence are important variables to assimilate in order

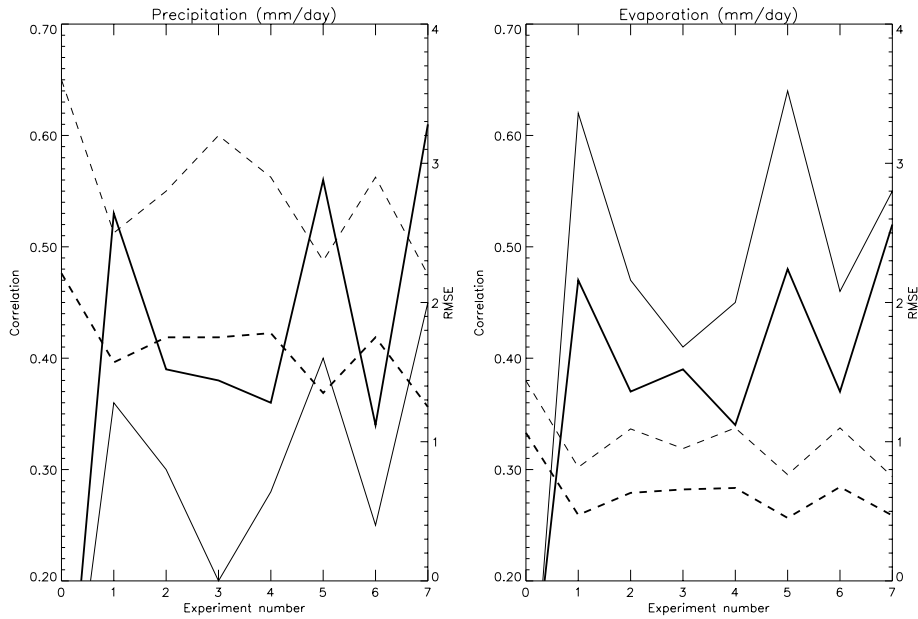


Figure 2.3: Correlation (solid line) and RMSE (dashed line) between ECMWF 12-36h forecast fields and the assimilation experiments outlined in Table 2.1 for July 1989. Thick lines represent averages over the extratropics and thin lines over the tropics.

to improve the precipitation and evaporation field. Figure 2.4 shows a comparison between the total precipitation and evaporation fields from assimilation experiments 0, 5, and 7 and several ECMWF forecast intervals up to 3 days. It can be seen that a forecast period of more than 2 days is needed to reduce the spin-up to an acceptable level. Further, Figure 2.4 shows that the global hydrological balance for the relaxation experiments is well simulated. The difference between evaporation and precipitation is less than 0.1 mm/day. The global mean evaporation and precipitation simulated by experiment 5 and 7 also compare both well with the ECMWF 2-3 day forecast. Whereas the bias (ECHAM-ECMWF) for the basic observed quantities (not shown) does not vary much with the relaxation coefficients chosen, there seems to be a systematic change in both the bias for precipitation and evaporation. It can be seen that by increasing the strength of the relaxation coefficients (from experiment 0 via 5 to 7) the globally averaged values of precipitation and evaporation decrease with about 0.25 mm/day, which is about 10 % of the global mean values.

Figure 2.5 shows the latitudinal dependence of ECHAM precipitation from relaxation experiments 5, 1, and 7 compared to the control run and to precipitation data from the Global Precipitation Climatology Center (GPCC). These data are a mix of land-based observations and microwave, radar, and satellite measurements over the sea and where no data are available, the ECMWF short-range forecast is used [Rudolf, 1995]. In general, the ECHAM produced precipitation patterns look realistic. Especially in the northern hemispheric extratropics the differences with the observational GPCC data are small. Large differences of more than 1 mm/day can be observed in the southern hemispheric subtropics, near the tropical maximum in the Northern

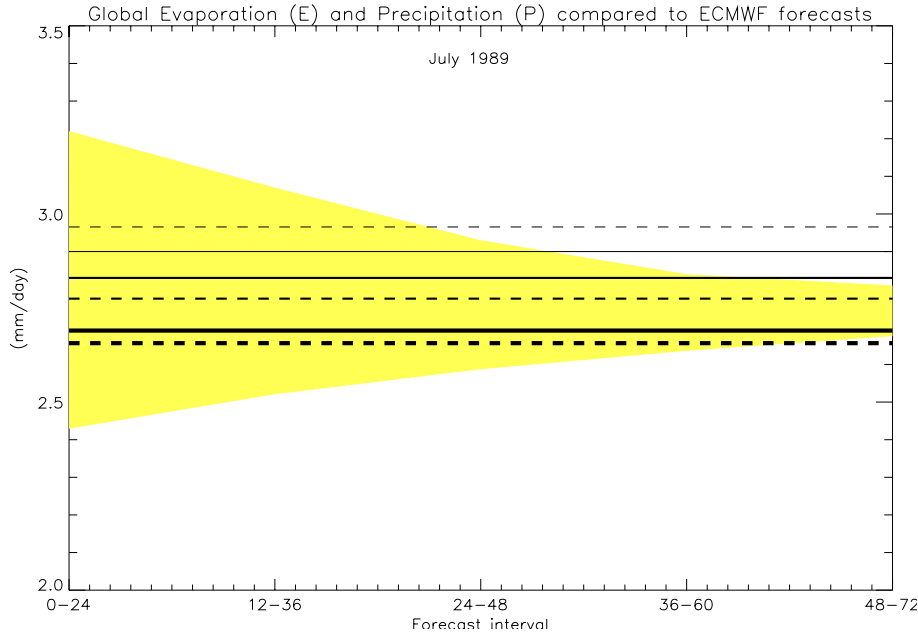


Figure 2.4: *ECMWF global mean precipitation (upper boundary of shaded area) and evaporation (lower boundary of shaded area) as a function of forecast interval. The horizontal lines represent in order of increasing thickness the precipitation (solid) and evaporation (dashed) for assimilation experiments 0, 5, and 7.*

Hemisphere and near  $35^\circ$  N where the ECHAM data show another precipitation maximum and the GPCC data do not. Since the satellite measurements are not available south of  $30^\circ$  S and since there are not many land-based observations in the southern hemisphere, the GPCC curve south of  $30^\circ$  S is mainly determined by the ECMWF short-range forecast. It can be seen that the ECHAM relaxation experiments follow the same pattern for this area but that there is a clear offset. This might be due to spin-up in the ECMWF shortrange forecast which is shown by Figure 2.4 for the global mean field. It appears that in the tropics and subtropics, the precipitation is reduced with increasing relaxation strength but in the extratropics, especially in the northern hemisphere, the opposite is true. However, due to the larger area of the tropical grid cells, which is taken into account when calculating global averages, the global value is reduced, which is shown in figure 2.4. This aspect will be further discussed in the following section.

### 2.5.3 Influence on the Model Physics

As outlined in section 3.3, the addition of an extra term to the model equations can influence the performance of the physical parameterizations. We have shown in section 2.5.2 that when using strong relaxation coefficients, the global averaged precipitation and evaporation is slightly reduced. The most serious effects of relaxation can be expected when the relaxation term is large compared to the other terms in the

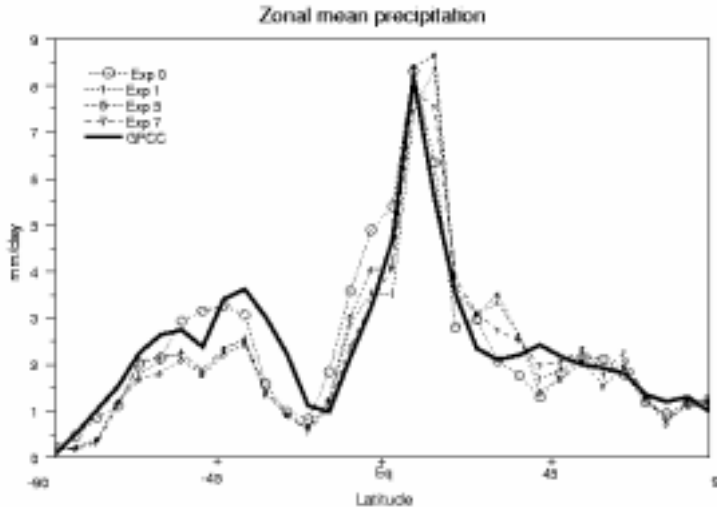


Figure 2.5: Zonal and monthly mean precipitation (millimeters per day) from assimilation experiments 0, 1, 5, and 7 compared to the Global Precipitation Climatology Center (GPCC) precipitation data [Rudolf, 1995] for July 1989.

equations. Figure 2.6 shows the magnitude of the relaxation term for temperature and its geographical distribution compared to the magnitude of the diabatic heating term, that is the third right-hand side term of Equation 2.2 compared to the first right-hand side term. The diabatic heating rates are calculated from ECMWF initialized analyses by *Siegmund* [1993]. The values for the relaxation term are obtained from relaxation experiment 5.

The absolute values of the diabatic heating are generally larger than the relaxation term. The difference is largest at the 850 and 500 hPa levels, where the heating is an order of magnitude larger than the relaxation term. The relaxation term hardly depends on latitude. The diabatic heating, on the other hand, is largest in the inter-tropical convergence zone and decreases toward the poles. The peak over Antarctica is probably due to errors in the ECMWF model see *Siegmund* [1993]. To gain a more quantitative insight in how much the model physics are affected by the relaxation process, we also considered the dependence of the vertical motions on the strength of relaxation. For this purpose we released a passive tracer at the model's surface with a constant source strength and a lifetime of 10 days. Since the source is distributed uniformly over the entire globe, changes in the vertical distribution of the tracer are mainly due to vertical transport. Figure 2.7 shows the ratios between the tracer concentrations at 250 hPa level and the surface, and the 750 hPa level and the surface, respectively. The values are averages over 15 day-simulations for July 1989

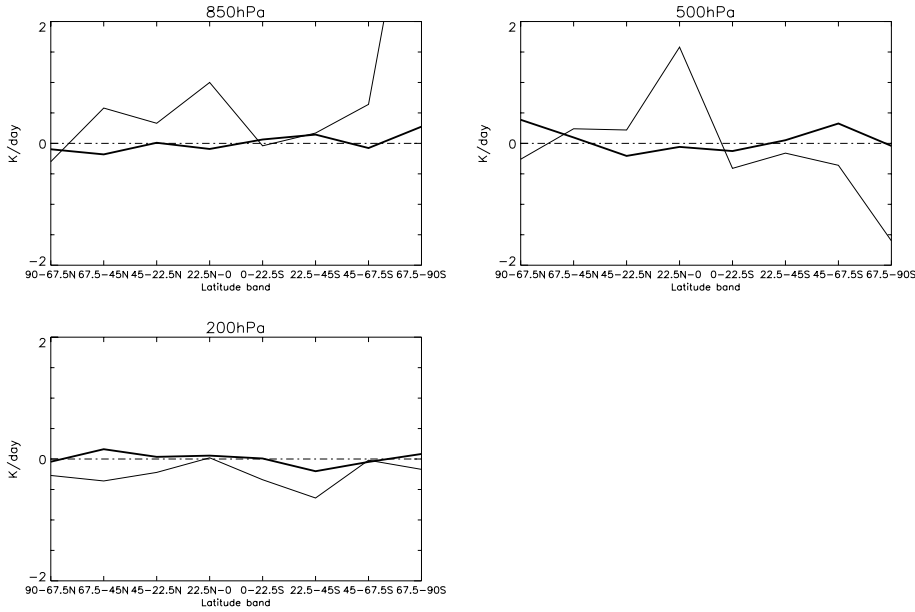


Figure 2.6: Zonal mean temperature (for July 1989) forcing (bold line) caused by relaxation compared to the diabatic heating (thin line) as calculated by Siegmund [1993] from ECMWF analyses (average over three July months).

Exp.	$G_T$	$G_D$	$G_{V_o}$	$G_{lnsp}$
A(=0)	0.0	0.0	0.0	0.0
B	$1.10^{-6}$	$0.5.10^{-5}$	$1.10^{-5}$	$1.10^{-5}$
C(=5)	$1.10^{-5}$	$0.5.10^{-4}$	$1.10^{-4}$	$1.10^{-4}$
D(=1)	$1.10^{-4}$	$0.5.10^{-4}$	$1.10^{-4}$	$1.10^{-4}$
E	$1.10^{-4}$	$0.5.10^{-3}$	$1.10^{-3}$	$1.10^{-3}$
F(=7)	$1.10^{-3}$	$0.5.10^{-3}$	$1.10^{-3}$	$1.10^{-3}$

Table 2.4: Specification of the relaxation coefficients used for the experiments plotted in Figure 2.7.  $G_D$ ,  $G_{V_o}$ ,  $G_T$  and  $G_{lnsp}$  are the relaxation coefficients ( $s^{-1}$ ) for divergence, vorticity, temperature and surface pressure respectively. The numbers between the brackets refer to Table 2.1.

(A-F on the horizontal axis are six assimilation experiments described in Table 2.4. The ratio of the tracer concentrations between 750 hPa and the surface is a measure of the vertical exchange of tracer by boundary layer processes, and the ratio of tracer concentrations between 250 hPa and the surface is a measure for the vertical exchange through convective processes. Figure 2.7 shows that the convective exchange of tracers over sea is quite sensitive to the relaxation coefficient for temperature since there is a large drop in ratio when going from experiment C to D. The only difference between experiment C and D is a factor 10 in the relaxation coefficient for temperature. The

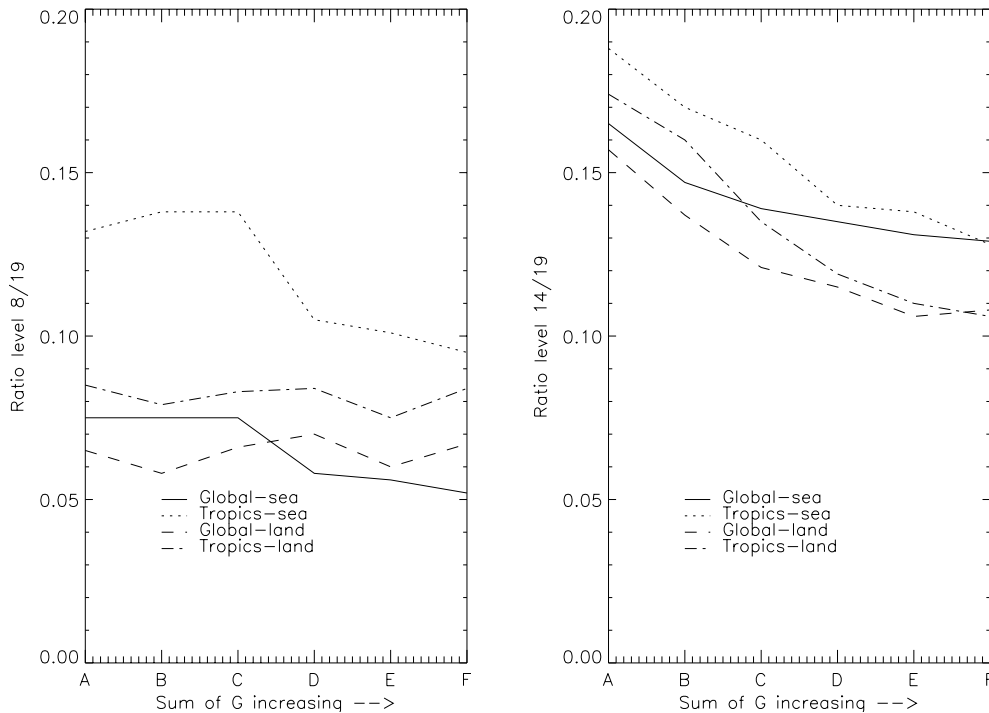


Figure 2.7: *The ratio of tracer concentrations between model level 8 ( 200 hPa) and the surface (left) and model level 14 ( 750 hPa) and the surface (right) after a 15 day-run for July 1989. The ratios are calculated separately for sea and land and tropics and extratropics*

convective exchange over land is hardly influenced by the strength of the relaxation. Apart from the magnitude of the ratio, the behavior is similar for the tropics and the extratropics.

Figure 2.7 also shows that the boundary layer exchange decreases when increasing the strength of relaxation. This decrease is largest for the tropics over land where it is almost 40 % between experiment A and F. A difficulty with interpreting Figure 2.7 is that we do not know the real vertical exchange. It is, however, unlikely that there is such a large difference between the vertical exchange in ECHAM and the ECMWF model since both models apply similar boundary layer diffusion and convection schemes. We therefore think that a main reason of the observed systematic decrease of vertical tracer exchange is the spin-up effect which becomes stronger with increasing relaxation strength. This effect apparently has a stronger influence on the boundary layer exchange than on the convective exchange. Since we want to maintain the intensity of parameterized processes in the ECHAM model, it implies that we should use as weak relaxation coefficients as possible.

## 2.6 Discussion and Conclusions

We have shown that in the extratropics, good agreement between ECHAM fields from model simulations with relaxation and ECMWF analyses is obtained for the basic observed quantities. For example, tendency correlations between ECMWF analyses and ECHAM simulation are higher than 90 %. The agreement in the tropics is poor. This is a major drawback of the proposed method. As model results in the tropics are strongly determined by the model physics we have to expect differences due to different parameterizations. Additionally, the relaxation method which is based on geostrophic adjustment of dynamical processes, will have little effect in tropical regions.

Since ECHAM and ECMWF have different physical parameterizations, the agreement of the derived variables is not as good as for the observed ones. Moreover, the ECMWF model output is, due to the long spin-up time, quite sensitive to the choice of the forecast interval. We found that only after 2.5 days the spin-up error in the ECMWF precipitation forecast is reduced to an acceptable level. The bias of the precipitation and evaporation between ECHAM and ECMWF as simulated in the assimilation experiments is within the range of the ECMWF spin-up error. However, validation of derived variables can only be done properly by comparison with measurements. This has been done by comparing with the GPCC data set [Rudolf, 1995], which is one of the most reliable precipitation data sets. The zonal averaged precipitation pattern is well simulated by the ECHAM relaxation experiments, although locally some large differences exist.

The problem of selecting satisfying relaxation coefficients for assimilation is a key issue. We have shown that too strong relaxation coefficients reduce the global averaged precipitation and evaporation and the vertical exchange of tracers. This implies that the model physics should not be too much dominated by the relaxation process. On the other hand, too weak relaxation, as in experiment 6, will worsen the agreement with the observational data. We consider the relaxation coefficients as used in experiment 5 to be a good compromise. In this experiment we used a value of  $1.10^{-5} s^{-1}$  for temperature,  $0.5.10^{-4} s^{-1}$  for divergence and  $1.10^{-4} s^{-1}$  for vorticity and surface pressure. The model performs better if the relaxation coefficient for temperature is relatively small, since the precipitation and the vertical exchange in convective clouds appear to be sensitive to the magnitude of this coefficient. It has been shown in Figure 2.6 that with a temperature relaxation coefficient of  $1.10^{-5} s^{-1}$ , the relaxation forcing does not dominate the diabatic heating term.

Inconsistencies between the ECMWF first guess data and the ECHAM model may have produced some artificial forcings. Close to mountainous terrain the flow will be different for an envelope orography model than for one using mean orography. These differences are not entirely canceled out by simple vertical interpolation. The ECMWF data used for the assimilation have been generated by T106 model runs. Although truncated to T21, these data will contain more information about smaller scales than ECHAM which has been run at T21 resolution. Therefore by using these data for assimilation, ECHAM is forced to adjust to scales which it in principle cannot reproduce. Better agreement can be expected if the resolution of the model and the analyses are the same. Results of higher-resolution experiments will be discussed in forthcoming papers.

Despite the fact that the proposed method has some major drawbacks, we think



that it is promising comparing specific episodes during measurement campaigns with climate models. The method is very simple and practical to apply. Only little additional computer time is required. Additional research should be done to improve results for the tropics. In its current setup the method is appropriate to validate ECHAM data with measurement in the northern hemispheric extratropics.

## 2.7 Outlook

Since the publication of this work [*Jeuken et al.*, 1996], the relaxation method has been successfully applied in several other studies. In a study by *Dentener et al.* [1999] the ECHAM model has been applied in “nudged” mode to simulate the radioactive  $^{222}\text{Rn}$ . Result were compared with instantaneous measurements and simulated  $^{222}\text{Rn}$  concentrations from the off-line tracer transport model TM3. The agreement with the measurements was quite well and similar as the agreement of TM3 with the measurements. Considering that the TM3 model is driven by ECMWF analysis this means that the actual transport is well simulated. *Feichter and Lohmann* [1999] go one step further and try to use the relaxation technique with ECHAM to validate derived variables like clouds and sulfate and sulfur dioxide concentrations. This is a severe test for the usefulness of the method, since these variables not only depend on transport but also heavily on the hydrological cycle in the model. Results are however encouraging and show that the use of the relaxation improves the agreement between model and measurements. In a IGAC/WCRP model intercomparison exercise, in which the sulfur cycle was tested, it was concluded that GCMs that used the relaxation technique performed better in comparisons with measurements than models without [*Lohmann et al.*, 1999]. ECHAM in “nudged” mode stood out as one of the best among the 10 participating models. Finally, *de Laat et al.* [1999] used ECHAM in “nudged” mode and with a complete tropospheric chemistry scheme successfully to simulate ozone profiles over the Indian Ocean. Because the ECMWF and ECHAM model have developed separately since the time the optimal nudging coefficients were derived, it might be wise to re-evaluate the coefficients. Also since the representation of the moisture field has been greatly improved in both models, it should be considered to use moisture for the relaxation as well, especially with respect to a better performance in tropical areas.

## Chapter 3

# Assimilation of total ozone satellite measurements in a three-dimensional tracer transport model

*This chapter has been adopted with minor modifications from: A. B. M. Jeuken, H. J. Eskes, P. F. J. van Velthoven, H. M. Kelder and E. V. Hólm, Assimilation of total ozone satellite measurements in a three-dimensional tracer transport model, J. Geophys. Res., 104, 5551-5563, 1999.*

### 3.1 Introduction

Satellite measurements of ozone have become increasingly available in recent years. Ozone data are obtained both from nadir-viewing (looking downward) instruments like the Total Ozone Mapping Spectrometer (TOMS) and Global Ozone Monitoring Experiment (GOME), and limb-viewing (looking at the zenith) instruments like the Microwave Limb Sounder (MLS). Nadir viewing instruments have the advantage of high spatial and temporal resolution in the horizontal domain. The main disadvantage, however, is an intrinsic low resolution in the vertical related to broad weighting functions used in the retrieval algorithm. Limb sounders do have a good vertical resolution in the stratosphere but are, in practice, not able to measure the lower parts of the atmosphere, that is, the troposphere. In addition, the horizontal and temporal resolution of limb sounders is usually poor. The bulk of the retrieved satellite ozone measurements consist of total column data.

Data assimilation provides a powerful tool to analyze sparse satellite data of chemical tracers, which are unevenly distributed in time and space. A model is used to describe the transport and chemistry of the tracers. It provides a constraint in time: combining a single measurement with the model leads to a prediction along the trajectory of an air parcel. In this way data voids are filled in, and using a good model can result in an analysis error that is significantly smaller than the error of the mea-

surement itself. On the other hand a data assimilation system can provide useful information about the errors and weaknesses in the model.

In this chapter an Optimum Interpolation (OI) data assimilation scheme is discussed for assimilating satellite ozone measurements in a three-dimensional global tracer transport model. We will restrict ourselves to ozone column measurements. The central question we address is whether assimilation of two-dimensional data into a three-dimensional model can provide us with a good three-dimensional analysis. A two-step procedure is derived, and column and profile results are discussed separately.

The main problem here is the lack of vertical information: how should the mismatch in total ozone between the model prediction and the measurements be distributed over the vertical model layers? Different approaches to this problem are proposed. Using a global tracer advection model with a simple chemistry parameterization, the results of these approaches are compared. The ozone column measurements that are used in this study are from the TIROS Operational Vertical Sounder (TOVS) instrument [*Planet et al.*, 1984]. This nadir-viewing instrument measures in the infrared part of the spectrum and for this reason is not restricted to daylight.

Assimilation of trace gas satellite data into atmospheric models is receiving increased attention in the recent literature. *Fischer and Lary* [1995]; *Sutton et al.* [1994]; *Lary et al.* [1995] analyzed limb measurements in stratospheric models with and without chemistry. *Elbern et al.* [1997] discuss variational assimilation of surface data into a tropospheric chemical model. *Levelt et al.* [1996] have focused on the assimilation of ozone columns, using a two-dimensional (latitude-longitude) tracer advection model. This latter approach avoids the problem of distributing ozone in the vertical. However, the restriction to two dimensions leads necessarily to relatively large model errors. To obtain a good model forecast as well as information about the vertical distribution of ozone, a three-dimensional model is necessary. In the work of *Riishøjgaard* [1992], ozone columns are used to initialize a three-dimensional general circulation model. The tropopause pressure and a predefined stratospheric ozone profile are used to distribute the ozone column amount in the vertical. *Riishøjgaard* [1996] uses data assimilation to investigate the possibility to extract dynamical information from satellite ozone measurements. He concludes that assimilation of ozone into a dynamical model has the potential to improve the analysis of the wind field. The influence on the ozone profile is not directly studied.

The benefits of data assimilation are demonstrated in Figure 3.1. The scattered collection of 24 hours of TOVS measurements, with considerable data gaps, is turned into global maps of the ozone distribution at any moment required. The synoptic ozone features in the assimilated field compare favorably with gridded TOMS measurements of the same day. For instance, despite the sparsity of the TOVS data, the ozone peak near Japan is well captured by the assimilation.

This chapter is organized as follows. In section 3.2 we formulate the statistical framework for the data assimilation method. The ozone transport model and the chemistry parametrization are described in sections 3.3 and 3.4, respectively. Three subsequent sections discuss the assumptions and estimations of the error matrices necessary to implement the assimilation method. The results are discussed for the columns in section 3.8 and for the profiles in section 3.9. Conclusions are given in section 3.10.

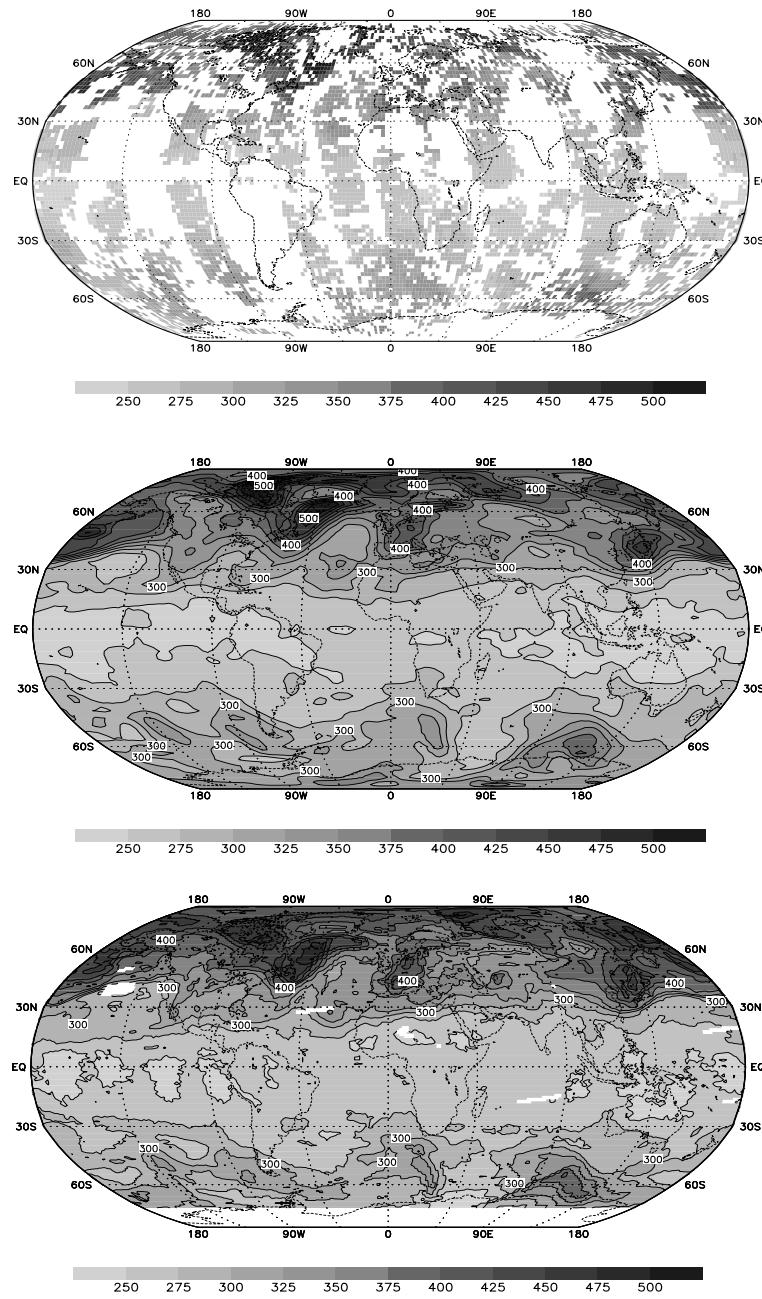


Figure 3.1: (a) Raw TOVS data , (b) assimilated TOVS and (c) gridded TOMS data for April 16, 1992. Both the TOVS and TOMS data are a compilation of 24 hours of measurements. The assimilated model field is shown at 1200 UT.

## 3.2 Assimilation Method

The assimilation approach is based on the optimal interpolation (OI) also called statistical interpolation technique [Daley, 1991]. Starting from the assumption that the model error covariance can be separated in a horizontal and vertical part, the analysis step consists of two steps. First, the two-dimensional total ozone column field is analyzed using the total ozone measurements. Then in the second step the analysis increment is distributed over the vertical layers in the model. This procedure is attractive, as it allows us to study these two aspects separately.

In each model time step (of 40 minutes in our case) the available TOVS total ozone values are analyzed. The set of ozone column observations (expressed in Dobson Units (DU)) are written in vector notation  $\vec{Q}^{\text{obs}} = \{Q_k^{\text{obs}}; k = 1, K\}$ .  $K$  is the number of ozone retrievals in the current time step. This number is highly variable, ranging from 0 to about 1600 TOVS pixels. The subscript  $k$  (or  $l$ ) is used as index for the observations. The three-dimensional model ozone field  $\vec{q} = \{q_{im}\}$  is labeled by two subscripts:  $i$  (or  $j$ ) identifies the horizontal lat-lon position, and  $m$  (or  $n$ ) is the vertical model layer index. We choose to express the ozone field  $q_{im}$  in Dobson units. This implies that the model ozone columns are simply the vertical sum of the model grid values  $Q_i = \sum_m q_{im}$

A linear observation matrix  $\mathbf{H}$  will give a set of model predicted total ozone values  $Q_k$  at the positions of the measurements (note the difference between  $Q_k$  and  $Q_i$ )

$$Q_k = \sum_{im} H_{k;im} q_{im} \quad (3.1)$$

Because  $q_{im}$  is expressed in DU, the matrix  $\mathbf{H}$  will be independent of  $m$ , or  $H_{k;im} = H_{k;i}$ . Note that  $\mathbf{H}$  projects a vector from the model space onto the observation space. Consequently the transpose,  $\mathbf{H}^T$ , distributes quantities defined at the observation positions over the surrounding model grid points.

Using these definitions, we can write down a cost function [Lorenz, 1988] which measures the departure of an ozone distribution  $q$  from both the model forecast  $q^f$  as well as the measurements  $Q^{\text{obs}}$ :

$$\begin{aligned} \mathcal{J} = & \frac{1}{2} \left( \mathbf{H}\vec{q} - \vec{Q}^{\text{obs}} \right)^T \mathbf{O}^{-1} \left( \mathbf{H}\vec{q} - \vec{Q}^{\text{obs}} \right) \\ & + \frac{1}{2} \left( \vec{q} - \vec{q}^f \right)^T \mathbf{B}^{-1} \left( \vec{q} - \vec{q}^f \right). \end{aligned} \quad (3.2)$$

The ozone field  $q_{i,m}$  which minimizes the cost function  $\mathcal{J}$  is the optimal analysis  $q_{i,m}^a$ . The closeness of the optimal analysis field to either the model forecast or the measurements is determined by the combined instrument, retrieval and representativeness error covariance matrix  $\mathbf{O}$  (with elements  $O_{kl}$ ), and the forecast error covariance matrix  $\mathbf{B}$  with elements

$$B_{im;jn} = \langle (q_{im}^{\text{true}} - q_{im}^f)(q_{jn}^{\text{true}} - q_{jn}^f) \rangle \quad (3.3)$$

Here  $q_{im}^{\text{true}}$  is the true ozone distribution, which of course is unknown. The angular brackets denote the average with respect to time.  $\mathbf{B}$  describes the horizontal and vertical correlations between forecast errors on the model grid. Note that by defining

a quadratic cost function we have implied that all errors can be described by Gaussian probability functions.

The analysis field  $q_{im}^a$  is found by requiring that the derivatives of  $\mathcal{J}$  with respect to  $q_{im}$  are equal to zero. This derivation leads to the well-known optimal interpolation equation

$$\bar{q}^a = \bar{q}^f + \mathbf{B}\mathbf{H}^T (\mathbf{H}\mathbf{B}\mathbf{H}^T + \mathbf{O})^{-1} (\bar{Q}^{\text{obs}} - \mathbf{H}\bar{q}^f) \quad (3.4)$$

The last term between brackets is the set of departures, the differences between the observations and the model predictions. These departures are multiplied by weight factors which are essentially given by  $\mathbf{B}/(\mathbf{B} + \mathbf{O})$ . For small model errors the correction will be small, while for small observation errors the model is forced to reproduce the measurements ( $\mathbf{B}/(\mathbf{B} + \mathbf{O}) = 1$ ). The departures and the matrix inversion involve quantities defined at the observation positions. The term  $\mathbf{B}\mathbf{H}^T$  puts the analysis increments on the model grid and distributes them over an area determined by the model correlation length.

The covariance matrix  $\mathbf{B}$  is modeled by the following form:

$$B_{im;jn} = \sigma_i \sigma_j \rho(|\vec{r}_i - \vec{r}_j|) \beta_{mn}^{(i)(j)} \quad (3.5)$$

The term  $\rho(|\vec{r}_i - \vec{r}_j|)$  is a homogeneous horizontal correlation function which depends only on the distance between the lat-lon positions  $i$  and  $j$ , and  $\rho(0) = 1$ . The vertical covariances between the layers  $m$  and  $n$  are described by  $\beta_{mn}^{(i)(j)}$ . These are normalized by  $\sum_{mn} \beta_{mn}^{(i)(j)} = 1$ . With these normalization conventions the quantity  $\sigma_i$  may be interpreted as the uncertainty of the model total-ozone column  $i$ . The superscripts  $(i)(j)$  indicate that the vertical covariances maybe weakly dependent on the horizontal coordinates.

To simplify the notation, let us introduce an analysis increment vector, with values defined at the observation points  $k$

$$\vec{v}^{\text{incr}} = (\mathbf{H}\mathbf{B}\mathbf{H}^T + \mathbf{O})^{-1} (\bar{Q}^{\text{obs}} - \mathbf{H}\bar{q}^f) \quad (3.6)$$

Using the expression (3.5) for the model covariance matrix, the following expression is obtained for the analyzed model ozone

$$\begin{aligned} q_{im}^a &= q_{im}^f + \sum_{jn} B_{im;jn} [\mathbf{H}^T \vec{v}^{\text{incr}}]_{jn} \\ &= q_{im}^f + \sum_j \sigma_i \sigma_j \rho(|\vec{r}_i - \vec{r}_j|) \sum_n \beta_{mn}^{(i)(j)} [\mathbf{H}^T \vec{v}^{\text{incr}}]_{jn} \end{aligned} \quad (3.7)$$

Because the observation matrix  $\mathbf{H}$  does not depend on the vertical index  $n$ , the analysis equation for the ozone columns simplifies to ( $Q_i^a = \sum_m q_{im}^a$ )

$$Q_i^a = Q_i^f + \sum_j \sigma_i \sigma_j \rho(|\vec{r}_i - \vec{r}_j|) [\mathbf{H}^T \vec{v}^{\text{incr}}]_j \quad (3.8)$$

With the assumption that  $\beta_{mn}^{(i)(j)}$  is homogeneous (does not depend on the horizontal coordinate; i.e.,  $\beta_{mn}^{(i)(j)} = \beta_{mn}$ ), the new model ozone profile can be expressed in terms

of the column analysis  $Q_i^a$

$$\begin{aligned} q_{im}^a &= q_{im}^f + F_m \left[ Q_i^a - Q_i^f \right], \\ F_m &= \sum_n \beta_{mn}, \quad \sum_m F_m = 1 \end{aligned} \quad (3.9)$$

This rewritten form of the analysis equation (3.4) defines the two-step procedure. In the first step, equation (3.8), the model ozone columns are adjusted (the basic OI equations). The equation for  $\vec{v}^{\text{incr}}$  is solved by Gauss-Jordan reduction with partial pivoting. Then a column-by-column redistribution of these analysis increments, equation (3.9), gives the full three-dimensional ozone analysis (step 2, equation (3.9)). The last step only depends on the vertical weight function  $F_m$ , and this is the only place where the vertical error covariance  $\beta_{mn}$  enters. The separation of the OI approach in a horizontal and a vertical step is very illuminating: it shows directly how the lack of information (i.e., how to distribute the mismatch between the measurement and the total ozone observation over the vertical layers of the model) influences the assimilation approach.

The assimilation method depends on a realistic estimate of the errors in the model, in the observations, and in the analysis system. The estimation of  $\mathbf{O}$ ,  $\sigma_i$ ,  $\rho(r)$ , and  $\beta_{mn}$  will be discussed in sections 3.5 to 3.7.

### 3.3 Transport Model Description

The tracer transport model (TM3) used in this study has been adapted from the global tracer transport model TM2 [Heimann, 1995]. The present model calculates the horizontal and vertical transport of tracer mass using meteorological fields from the European Centre for Medium-Range Weather Forecasts (ECMWF) model. The input meteorological fields are updated every 6 hours [Velthoven and Kelder, 1996]. The analyzed meteorological fields of wind, surface pressure, temperature, and humidity (with resolution  $2.5^\circ \times 2.5^\circ$ ) are interpolated to the TM3 model grid. In this study the TM3 model has 19 vertical sigma-pressure layers between the surface and 10 hPa and a horizontal resolution of  $3.75^\circ \times 5^\circ$ . The vertical resolution in the stratosphere is coarse with only three layers between 50 and 10 hPa. The top layer contains all air between 20 and 0 hPa.

The transport equation for ozone can be written as follows:

$$\frac{\partial \rho \chi}{\partial t} + \nabla \cdot \rho \vec{u} \chi = R, \quad (3.10)$$

where  $\chi$  is the ozone mass mixing ratio (kg/kg),  $\rho$  is the air density (kg/m<sup>3</sup>),  $\vec{u}$  is the three-dimensional wind vector and  $R$  represents the sources and sinks (e.g. chemistry and deposition). Three-dimensional tracer transport in the model is accounted for by advection for the resolved motions and by convection and vertical diffusion for the unresolved motions (the sub-grid scale). The advection of tracers in the model is calculated with the slopes scheme of Russell and Lerner [1981]. The subgrid scale convection fluxes are calculated using the scheme of Tiedtke [1989]. The vertical diffusion is calculated using the parameterization of Louis [1979].

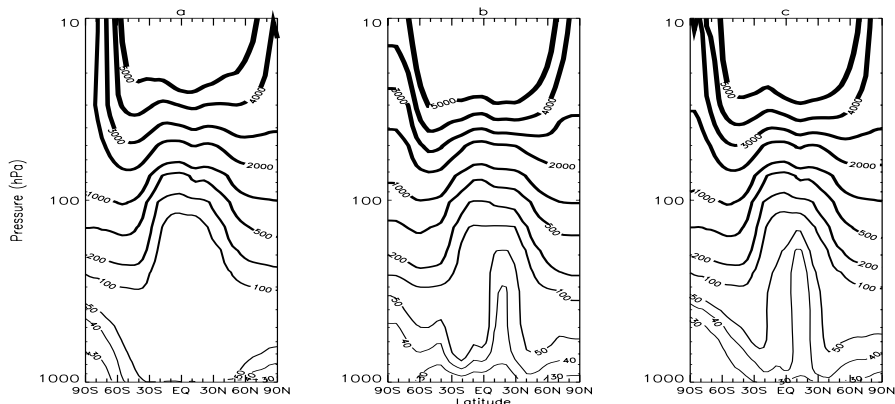


Figure 3.2: Monthly averaged zonal mean ozone mixing ratios (ppbv) for September 1992. (a) Model simulation calculated with Cariolle chemistry. (b) Climatology of Fortuin and Kelder [1998]. (c) Model simulation with modified Cariolle chemistry (equilibrium values replaced by climatology) and no chemistry in the troposphere.

### 3.4 Chemistry Parameterization

Ozone is mainly produced in the tropical stratosphere by the photolysis of oxygen [Chapman, 1930; Crutzen, 1970; Johnston, 1971]. By the poleward meridional circulation it is transported to higher latitudes, where it is transported downwards. As a result maximum ozone mixing ratios in the tropics are found around 10 hPa and around 50 hPa in the extra-tropics (see figure 3.2).

The classical view of the origin of tropospheric ozone is that it is transported from the stratosphere and destroyed at the surface [Regener, 1949]. In the 1970's it was recognized, however, that considerable amounts of ozone are produced in the troposphere [Crutzen, 1973]. The gross chemical production and loss terms can be six times as large as the influx from the stratosphere. However, averaged over large spatial and time scales, they are nearly in balance, and the net ozone production is small. Locally larger differences between ozone production and loss may exist.

To simplify our model set-up we decide not to include any tropospheric chemistry in our model but only apply dry deposition at the surface. We apply a simple scheme, using a constant deposition velocity that discriminates between land, ice, and sea surfaces [Wauben *et al.*, 1998].

To capture the ozone maximum correctly and to prevent the stratosphere from losing all ozone by stratosphere-troposphere exchange in the long run (typically a few months), some stratospheric chemistry describing the ozone production needs to be included in the model. A full stratospheric chemistry scheme would be very costly in computing time and needs a treatment to balance different chemical species in the assimilation procedure. This is a step in future research but is not within the scope of this thesis. We choose to use a chemistry parameterization developed by [Cariolle and Déqué, 1986]. Their approach consists of the linearization of the ozone photochemical sources and sinks around equilibrium values using a two-dimensional photochemical



model. In the parameterization the mixing ratio of ozone ( $\chi$ ) is calculated by

$$\begin{aligned} \frac{d\chi}{dt} = & \langle S \rangle + \left\langle \frac{\partial S}{\partial \chi} \right\rangle (\chi - \langle \chi \rangle) + \left\langle \frac{\partial S}{\partial T} \right\rangle (T - \langle T \rangle) \\ & + \left\langle \frac{\partial S}{\partial \Phi} \right\rangle (\Phi - \langle \Phi \rangle), \end{aligned} \quad (3.11)$$

where  $S = (P - L)$  is the photochemical production minus chemical loss of ozone,  $T$  is the temperature (K), and  $\Phi$  the ozone column content above the point of interest ( $\text{kg m}^{-2}$ ). The terms between  $\langle \rangle$  are two-dimensional climatological mean values calculated with their two-dimensional photochemical model. The other terms are variables in the current three-dimensional model. Local production and loss rates of ozone depend not only on the ozone mixing ratio (first and second term on right-hand side) but also on temperature (third term), because of the temperature dependence of the chemical reaction rates, and on the local UV flux (fourth term), which is a function only of the total number of ozone molecules above the local point. Heterogeneous chemistry is not included, so we will not be able to simulate the chemical processes contributing to the formation of the ozone hole.

We apply chemistry only in the stratosphere, using the climatology of *Fortuin and Kelder* [1998] as equilibrium values. This climatology is based upon ozone sondes and Solar backscattered ultraviolet (SBUV) measurements over the period 1979-1990. Figure 3.2a shows that the vertical ozone distribution after 1 month of simulation, with the original Cariolle parameterization used over the whole vertical model domain, does not correspond very well with the present climatology. The structure of the zonally averaged ozone field in the tropics is much better represented if, like we do, no chemistry is applied in the troposphere (see Figure 3.2c).

### 3.5 TOVS Observation Errors

For the TOVS ozone retrieval, errors of 5% or more are often mentioned [*Planet et al.*, 1984], [*Engelen*, 1996]. Several sources of errors in the retrieval are discussed by [*Lefèvre et al.*, 1991]. These authors estimate an error of 16-18 DU under clear-sky conditions and of 25 DU if clouds are present. Comparing the TOVS ozone pixels with gridded TOMS data (provided by NASA) gives similar results. The largest deviations occur at midlatitudes (Northern Hemisphere), while in equatorial regions the differences are considerably smaller. We will adopt a combined TOVS retrieval and representativeness error of 25 DU at mid and high latitudes and an error of 15 DU in the equatorial regions.

It is well known that the TOVS retrieval encounters problems due to the low emissivity of sand. To account for this, we additionally applied a desert mask to the model grid with an observation error of 40 DU. The globally averaged error with this procedure is 23 DU.

Typically, about five TOVS measurements occur in a single TM3 grid cell. Instead of assimilating the individual TOVS pixels, “super observations” are used. These consist of the set of TOVS observations inside a given model grid box. The individual departures between the TOVS observations and the model field are determined by interpolation of the model grid values to the positions of the individual TOVS pixels. These departures are then averaged over the grid cell. The error of the super

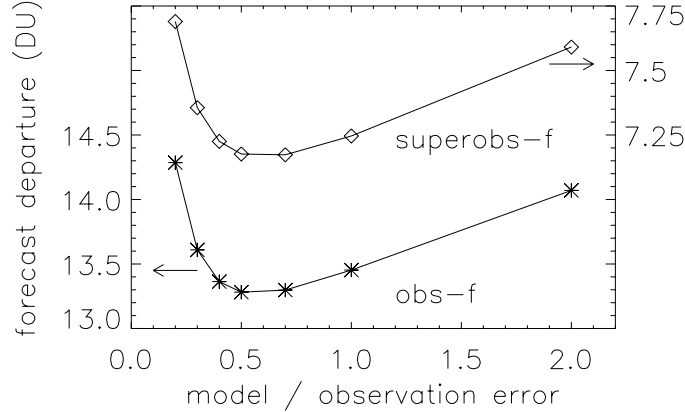


Figure 3.3: *RMS of the difference between the forecast and the TOVS observation as a function of the ratio between the model and observation error.*

observation is determined by the number of observations  $K_i$  in cell  $i$ , and the degree of correlation between the TOVS errors. If  $c$  is an average correlation factor for the measurements in grid cell  $i$ , then

$$\sigma_i^{\text{superobs}} = \sigma^{\text{obs}} \sqrt{\frac{1-c}{K_i} + c} \quad (3.12)$$

An estimated value  $c = 0.5$ , as determined in section 3.6, is used. The observation matrix  $\mathbf{O}$  is now taken to be diagonal.

### 3.6 Horizontal Error Covariance

In the case of the model error (the standard deviations  $\sigma_i$ ) it is natural to assume that larger errors will occur if the ozone variation with time is also large. To mimic this effect, we take  $\sigma_i$  to be latitude dependent according to the zonally averaged model ozone variation found per latitude. This amounts to relatively small values around the equator and larger values at midlatitudes, similar to the TOVS observation error discussed above.

The absolute value of the model ozone column error (the mean of  $\sigma_i$ ) may be fixed in the following way. A series of assimilation runs is performed with varying ratios between the model and observation error. For each of these runs we monitor the forecast skill. The results are shown in Figure 3.3. The forecast compared with the individual TOVS pixels shows a clear minimum of the departure at a model/measurement error ratio of about 0.55. Using the super observations defined above, a similar value for the optimal ratio is obtained.

Apart from the average model error estimate, a functional form is needed for the horizontal model correlation function  $\rho(r)$ . We estimated the forecast error covari-

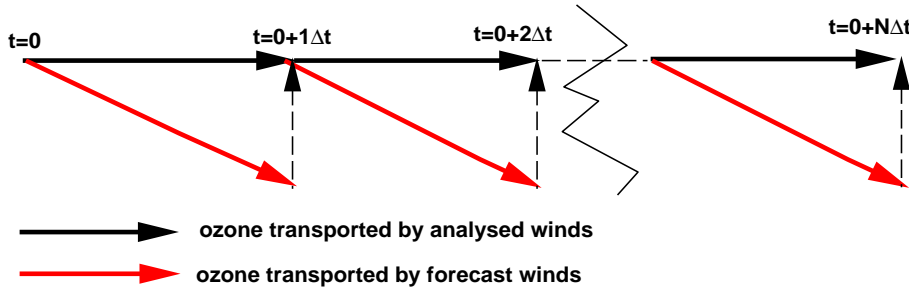


Figure 3.4: Schematic representation of the NMC estimate of the model error covariances.  $\Delta t$  is 24 hours, and  $N$  is 30 days.

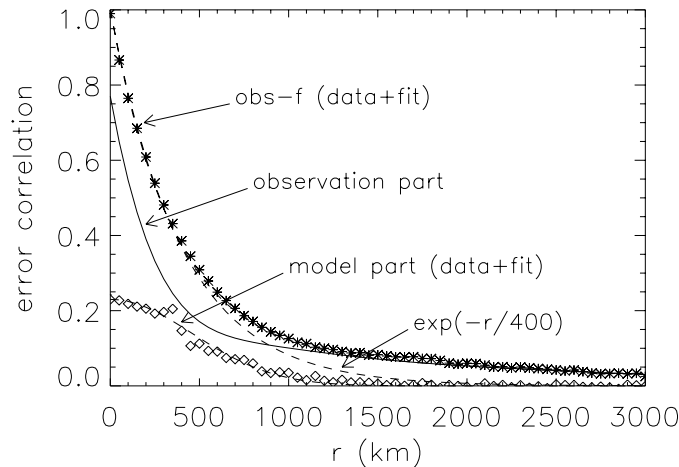


Figure 3.5: Horizontal ozone column error correlations as a function of the distance between the columns. Stars and dashed line: TOVS observation minus forecast correlations and a fit. Diamonds and dashed line: model error estimated with the NMC approach, plus a fit with a Gaussian function. Solid line: observation part of the total correlation.

ance matrix with an approach based on the so-called National Meteorological Center (NMC) method [Parrish and Derber, 1992], which is widely used in the numerical weather forecast community. In this method the difference between two model forecasts valid at the same time are used to estimate the error structure. We calculated two series of 24 hour forecasts, with 30 forecasts in each series. In one series the meteorological fields driving the TM3 model come from the ECMWF analyses, while in the other series the ECMWF 24 hour forecasts are the driving fields. The same ozone field is used to initialize both series, but due to the difference in meteorological input fields the ozone fields will diverge from each other in the 24 hour simulations and reveal the forecast error structures (see Figure 3.4 for illustration). In this way,

values for  $\rho(r)$  and  $\beta_{mn}$  (discussed in more detail in the next section) are found.

In Figure 3.5 the horizontal error statistics are shown. The observation minus forecast covariance is plotted as a function of the distance between the individual TOVS measurement positions. The values are divided by the corresponding variance, resulting in a dimensionless error correlation (stars in the figure).

When correlations between the model errors and observation errors can be neglected, the observation minus forecast covariance is the sum of the model and observation covariances

$$\langle (\vec{Q}^{\text{obs}} - \mathbf{H}\vec{q}^f) (\vec{Q}^{\text{obs}} - \mathbf{H}\vec{q}^f)^T \rangle = \mathbf{H}\mathbf{B}\mathbf{H}^T + \mathbf{O}. \quad (3.13)$$

Earlier (Figure 3.5) an optimal ratio between the model and observation error of 0.55 was found. This suggests that about 23% of the observation minus forecast variance is due to the model ( $\mathbf{B}$  term). Therefore we multiplied the model error correlation function (found using the NMC method) by this factor. The results are shown in Figure 3.5. A reasonable fit to these points is obtained using a Gaussian function with a  $1/e$  correlation length of 650 km.

Given the total RMS departure and the model contribution, it is tentative to assign the remaining covariance (solid line) to the TOVS observations. This observation part seems to consist of two parts. For distances less than 400 km the correlations are described well by an exponential decay. For longer distances a long featureless tail is found. In the assimilation the combined TOVS ozone values of the NOAA 11 and NOAA 12 satellites is used. Owing to, for instance, instrumental differences, biases of global and regional scales may exist. The globally and monthly averaged ozone value shows a difference of 12 DU between the two satellites (April 1992). The correlation data in figure 3.5 are already corrected for this global bias. If the data of only NOAA 11 are used, the ‘‘correlation tail’’ almost disappears. This is evidence that the long-range tail is caused by the differences between the two TOVS instruments/retrievals.

Using only the short-range observation correlations, modeled by an exponential distance dependence, an average correlation inside a TM3 grid box can be estimated. This factor  $c$  is found to be about 0.5, and this factor is used in equation (3.12).

It is interesting to observe that the correlation length is about 500 km. The model grid has a horizontal resolution of  $5^\circ$  by  $3.75^\circ$ . The advection scheme apparently has very little diffusion, and the model is able to preserve features with a size of about one grid cell.

### 3.7 Vertical Redistribution of the Ozone Analysis Increments

With the two-dimensional ozone column analysis given, the remaining task is to find good estimates for the weight function  $F_m$ , which distributes column errors over the vertical model layers. Note again that the weights are normalized. The absolute values are irrelevant. We use three different approaches for  $F_m$ :

1. With the NMC error covariance ( $F_m(x, y)$ ) approach the forecast error covariance matrix elements  $\beta_{mn}$  are estimated with the NMC method as described in the previous section. The vertical covariances obtained are divided by  $\sum_{mn} \beta_{mn}$  to obtain the normalized weight factors  $F$  as defined in equation (3.9).

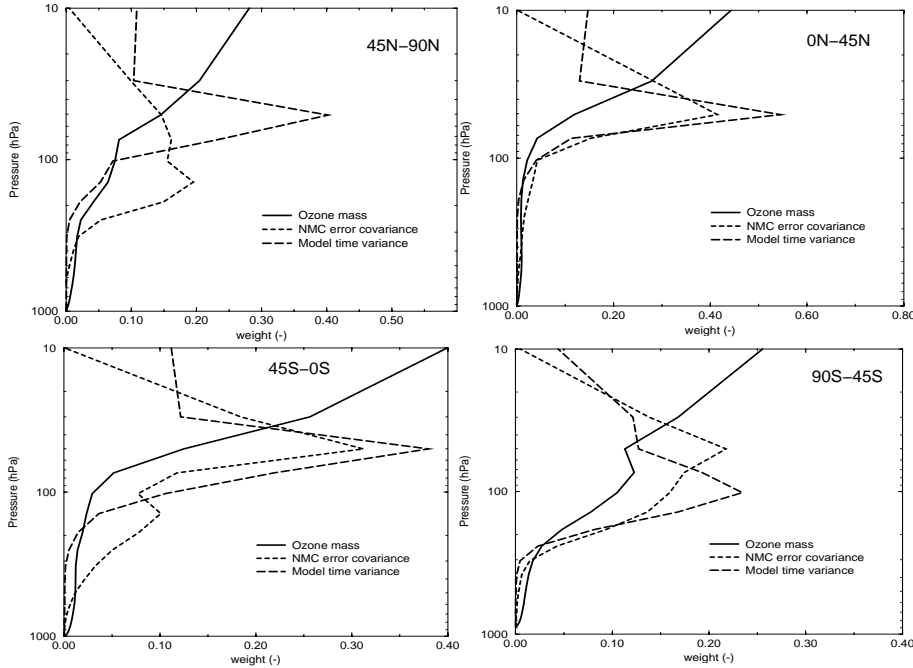


Figure 3.6: Normalized vertical weight functions  $F_m$  for 4 different geographical regions.

2. In the model time variance ( $F_m(x, y)$ ) approach it is assumed that the model forecast error is proportional to the model's variation in time, with the largest forecast error where the model transport is most variable. We use a model time variance calculated with the related chemistry-transport model CTM3 [Houweling *et al.*, 1998]. This variance field is three-dimensional and is calculated for each grid point over a series of 120 six-hourly output intervals.

3. In the ozone mass ( $F_m(x, y, t)$ ) approach we assume that the model forecast error is proportional to the actual ozone mass in a layer as given by the model. Then the model ozone profile gives the form of the model forecast error profile. After the analysis, the shape of the ozone profile remains unchanged.

In the derivation of equation 3.9 it is assumed that  $\beta_{mn}$  is homogeneous and does not depend on longitude and latitude. To satisfy homogeneity, global averages would have to be taken in the determination of the weight functions defined above. However the vertical ozone distribution and the height of the tropopause change considerably as a function of particularly the latitude. To take this into account, we use weight functions that do depend on the horizontal coordinate,  $\beta_{mn} = \beta_{mn}^{(i)(j)}$ . Here  $\beta_{mn}^{(i)(i)}$  is determined by one of the three recipes above, and we assume  $\beta_{mn}^{(i)(j)} = 0.5(\beta_{mn}^{(i)(i)} + \beta_{mn}^{(j)(j)})$ . Equation 3.9 is no longer mathematically correct, but the analyzed 3D ozone field can be determined conveniently using equation 3.7 directly. Note that the expression for the analyzed column (equation 3.8) is also valid for this generalized case. Equation 3.7 shows that only measurements that fall within a model-error correlation length (in our case about 500 km) from the analysis point have a substantial

influence. If the vertical covariance changes only slowly with position, as it does for the first two choices of  $\beta_{mn}$ , then the two-step approach is a good approximation (local homogeneity). However, even with the more rapidly changing scaling with the ozone mass, we find that equations 3.9 and 3.7 produce very similar ozone fields. The interpretation of equation 3.9 therefore remains valid: the local vertical covariances  $\beta_{mn}$  act as weight factors that determine how the ozone column analysis increment is distributed over the vertical layers.

Figure (3.6) shows the three vertical weight functions averaged over four geographical regions. The ozone mass weight function differs considerably from the others, with the maximum at the model top level, as expected. The time variance weight function and the NMC approach both have their maximum in the lower stratosphere. The NMC function, however, has a much broader and therefore less pronounced peak in the stratosphere. This is particularly visible for the region between 45°N and 90°N. Variations revealed by the NMC method are purely dynamical, since only the input wind field differs between the two parallel runs (see figure 3.4). The variance in time is calculated with a model with a different chemical scheme, and contains the combined variation of chemistry and transport in time.

## 3.8 Ozone Column Results

The power of data assimilation is illustrated in Figure 3.1. Irregularly distributed observations are mingled with the model forecast field, yielding a global picture of the ozone column field at any desired time. The model resolves synoptic features up to scales of 500 km supporting evidence, as was noted earlier, that the model's advection scheme has little diffusion. The full dynamical range of TOVS ozone values (with maxima over 500 DU) is well preserved by the assimilation. The comparison of the TOVS assimilated fields and a free model run with TOMS ozone data is shown in Figure 3.7. In the free model run, the assimilation is turned off at the third day of the month, and statistics are only accumulated over the last 20 days of the month. The assimilation, not surprisingly, improves the model result considerably compared to the simulation without assimilation. This improvement is mainly due to a reduction of the bias, especially in the equatorial region. The bias may indicate that the simplified chemistry, in combination with the limited vertical model resolution in the stratosphere, causes too low ozone values in the tropics (see also next section). Outside of the tropics, where the bias is smaller, the free run is quite close to the assimilation run. This indicates that even without assimilation the structures in the ozone column field are maintained correctly by the model, within this period of 1 month.

The model with assimilation is closer to TOMS than the TOVS observations themselves. This is especially the case in the storm track regions where dynamics play an important role. This indicates that the combination of TOVS and model is better than the original TOVS data alone. In the tropics where the dynamics play only a small role, the model basically adopts the TOVS ozone amount.

Although errors in TOMS are generally estimated to be smaller than errors in TOVS, we have to keep in mind that the picture shows a combination of TOVS and TOMS errors. For instance the bias, which is regularly increasing toward the pole in the Southern Hemisphere, may be (partly) due to the dependence of the TOMS

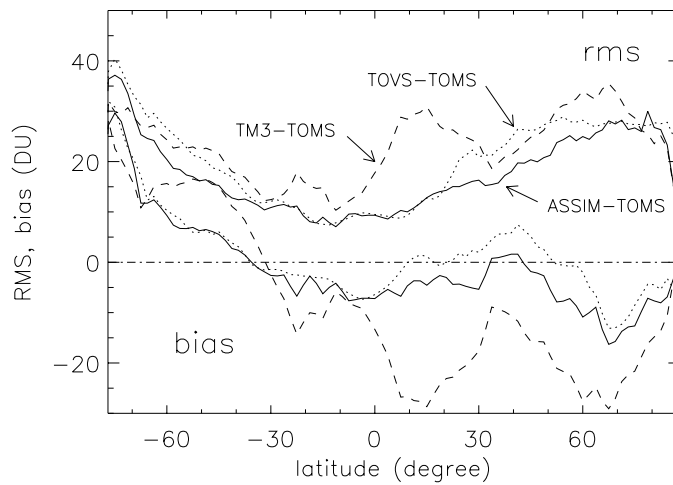


Figure 3.7: *The error statistics as a function of the latitude. Shown are the bias and the root-mean-square differences between the TOVS observations and TOMS, a free model run (TM3) and TOMS, and the assimilated field (assim) and TOMS. The Nimbus 7 TOMS gridded fields are supplied by NASA. Period: April 1992.*

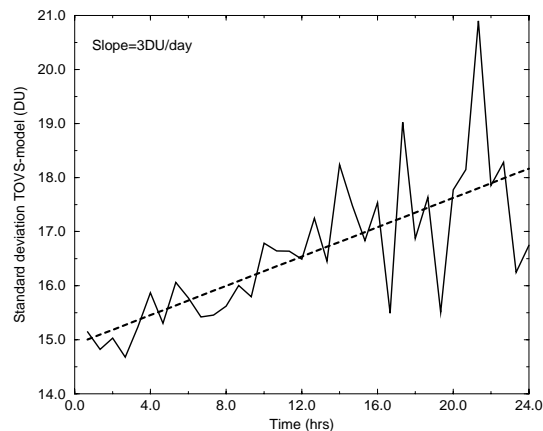


Figure 3.8: *Estimated linear error growth between  $60^\circ$  and  $90^\circ$  for April 1992.*

retrieval on the solar zenith angle.

In Figure 3.8 we monitor the growth of the difference between TOVS and model as a function of time. The calculated error growth rates from the linear regression are very small, ranging from about 0-1 DU in the tropics to 3-4 DU per day at higher latitudes. This is considerably smaller than the error growth in the two-dimensional

Assimilation Model KNMI (AMK) [Levelt *et al.*, 1996] which is typically 20 DU per day [Eskes *et al.*, 1999]. This means that a three-dimensional model is to be preferred to assimilate observations which are sparse in time and space.

### 3.9 Ozone Profile Results

To assess the quality of the model ozone profiles, the model results are compared with ozone sondes. In contrast to satellite limb profile measurements, sonde measurements cover the largest part of the vertical model domain with a good vertical resolution. We have taken the ozone sonde data from the World Ozone and Ultraviolet radiation Data Center (WOUDC). In total, almost 200 (April plus September) sondes are included in this comparison. A few characteristic cases for various geographical locations and for different meteorological situations are shown in Figure 3.9.

In general, the model and profile measurement results show good agreement, in particular, around the tropopause where most of the variation can be expected due to fast dynamical changes. The height and shape of the ozone-defined tropopause is captured very well by the model (e.g., Churchill, Sodankyla). For example, at Hohenpeissenberg for April 13 the observations as well as the model runs are outside the climatological bandwidth for the upper troposphere. For April 15, only 2 days later, the profile has changed considerably, and a clear secondary lower stratospheric ozone maximum, caused by filamentation of the polar vortex, can be distinguished. Also, this dynamical feature is reflected in the model results. However, model profiles are smoother than the observed ones, due to the limited model resolution.

As has already been shown for the column results, the model tends to underestimate the ozone column in the tropics. In the profile results this is reflected by the too low ozone concentrations above 50 hPa. This is illustrated by the profiles at Irene and Hilo. In the tropics the bulk of the ozone is located at this altitude. Our model has only three levels between 60 and 5 hPa. We suspect that the strong gradient in chemical ozone production in this region can not be simulated well with the limited resolution in the model, in this way causing a negative bias compared to the observations. Because of fast photochemistry, the forcing of the chemistry parameterization in the uppermost layer has such a short time scale that the assimilation has almost no effect here. This is reflected by the fact that all model simulations give almost exactly the same ozone concentrations in the uppermost layer.

For the South Pole two strikingly different profiles are shown. The April profile has a pronounced sharp shape. The model profile shows a similar but broader ozone distribution. The September profile clearly shows the ozone hole which starts developing in this month (note that a data point is missing at 10 hPa). Since the model does not contain ozone hole chemistry, large corrections by the assimilation are needed to force the model ozone to the observed low values. The results with assimilation are much better than without. However, since neither the vertical weight function nor the chemistry account for the ozone hole, the shape of the profile is not well simulated. Since it starts developing only in the second half of the month, the ozone hole is not fully reflected by the climatological mean for the whole month.

Only small differences between the results for the runs based on the three vertical weight functions can be distinguished. In most cases, column corrections are only small. As can be clearly seen for the ozone hole case, when the corrections become



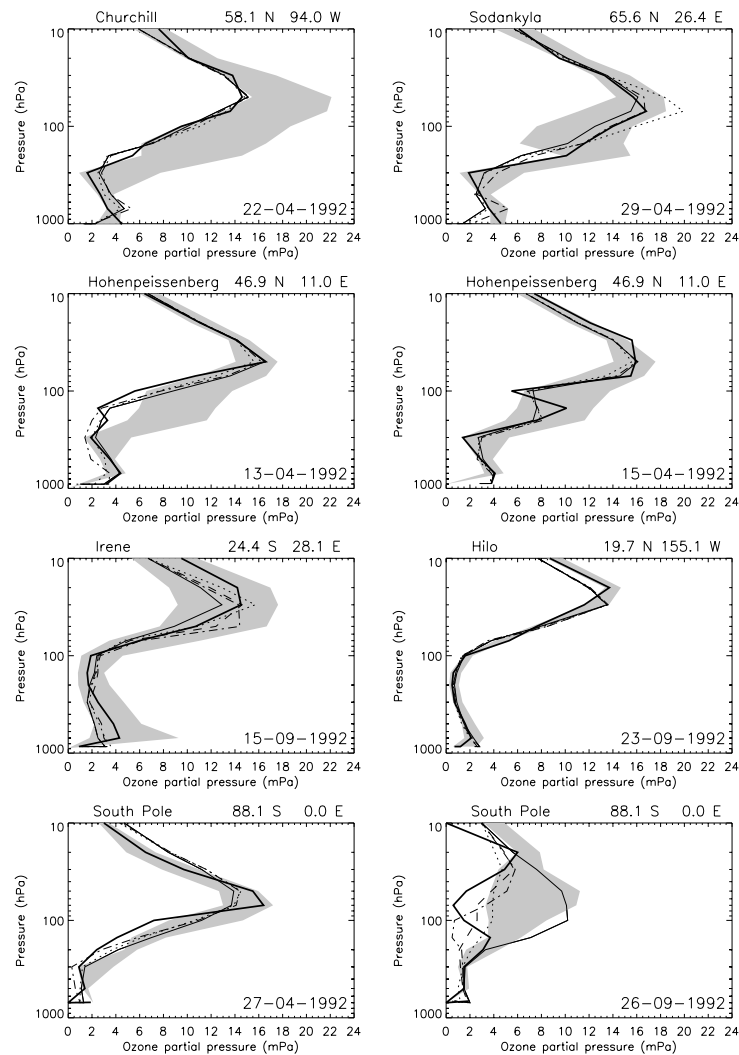


Figure 3.9: Model ozone profiles compared with selected ozone sonde measurements for April and September. The thick solid line is the sonde observation. The thin line is a model run without assimilation. The dashed, dotted, and dash-dotted lines are assimilation runs using the NMC error covariance, model ozone mass, and the model time variance vertical weighting coefficients  $F_m$ , respectively. The shaded area represents the climatological mean (over the period 1979-1990, given per month) for same ozone stations together with its standard deviation, taken from [Fortuin, 1996]. The model results are interpolated to the time, location, and standard pressure levels of the individual soundings.

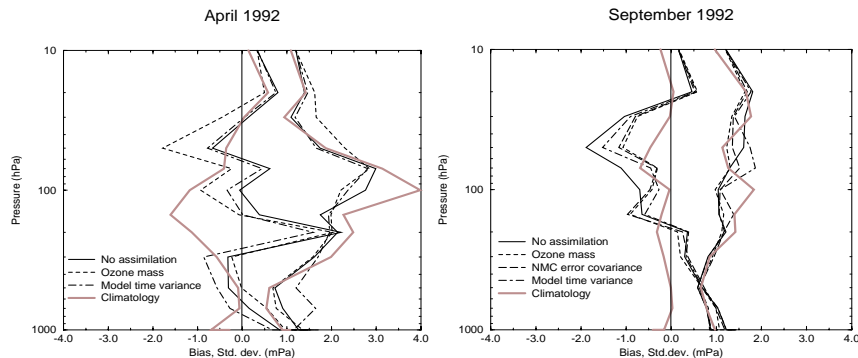


Figure 3.10: *Bias and standard deviation of the differences between modeled and actual ozone profiles and the difference between the climatological and actual profile for stations north of 30° N. Results are for (left) April and (right) September 1992. The number of sondes in the comparison is 34 and 41, respectively.*

larger, differences between different choices become more pronounced.

The model simulations without assimilation are not qualitatively different when considering the ozone profile. This supports the conclusion that the shape of the profile is hardly changed by the assimilation but is mainly determined by the model’s three-dimensional transport (from ECMWF-analyzed meteorology) and chemistry. Note that the “no assimilation” run has been initialized by applying assimilation in the first 3 days of the simulation. Since the ozone column error growth is only small, the integral of the ozone mass is preserved for a long time. It can therefore be expected that longer simulation periods than a month are needed to find more pronounced differences between profiles from simulations with and without assimilation.

Figure 3.10 gives a quantitative comparison between model and sonde profiles. It is known that individual sondes can sometimes give unrealistic ozone column amounts, inconsistent with both TOMS and TOVS. As a quality control, we have therefore made a selection of sonde measurements based upon how well they reproduce the observed column (should be within 7.5%). In addition, we only consider stations above 30°N. For other regions we do not have enough good sondes to calculate statistics. This leaves us with a sample size of 34 for April and 41 for September. The variance of the difference between sondes and the model is largest in April, when the storm track region is well developed in the Northern Hemisphere. For September in the stratosphere an improvement by data assimilation can be observed in the bias. Differences between the different weight functions are again small. Errors near the surface and in the troposphere are relatively large when compared to the absolute ozone amounts present. These errors are reasonable given the simplified parameterization of dry deposition and the lack of (polluted) boundary layer chemistry. For the part of the profile which is mainly determined by dynamical processes (tropopause, lower stratosphere), the model simulations agree better with the observations than the sonde climatology. For the lower troposphere and upper stratosphere the climatology compares similarly (standard deviation) or better (bias) with the actual sondes than the assimilation model, which is a disappointing result.

However, the interpretation of figure 3.10 is not straightforward. The sample size is small, and there may be a large representativeness error. Also, the vertical resolution is different between sonde and model. We have to keep in mind that the statistics shown are a sum of both errors in the model and measurements. A systematic bias in the measurements will also be present in the climatology of the measurements.

### 3.10 Discussion and Conclusions

In this chapter we have presented an approach for the assimilation of total ozone column measurements in a three-dimensional tracer transport model. The analysis can be seen as a two-step procedure. The equation for the columns does not depend on the choice of the vertical covariances. These vertical weights will influence the columns only indirectly via the 3-D transport in the model. However, these vertical covariances directly determine the weights with which the total ozone increments are distributed over the vertical layers.

Results for the total ozone analysis show that (compared to TOMS) the model ozone columns have improved by assimilating TOVS observations. Synoptic features are described well by the model. Structures of the size of one grid cell are resolved. In assimilation mode the full dynamical range of the high-resolution TOVS observations is reproduced well. The model in forecast mode maintains the correct synoptic structure, but in a few weeks time the dynamical range becomes smaller than TOVS. The good forecast skill is also confirmed by the slow model error growth and the small optimal ratio between model and observation error. The model analysis compares well with gridded TOMS data also for areas where no TOVS data were present. Especially, at higher latitudes where synoptic scale weather systems dominate, the model-assimilated field at the observation positions lies closer to independent TOMS measurements than the TOVS data itself.

The model, driven by ECMWF-analyzed meteorology, simulates good ozone profiles, compared to sonde measurements. Especially, dynamical features like the position of the tropopause and secondary ozone maxima can be reproduced. The good forecast skill of the model results in small analysis increments. The chemistry in the stratosphere and the mixing and deposition in the troposphere force the model profile towards an equilibrium. In combination with the small analysis increments this may explain that the three rather different weight functions give very similar results. In addition, the chemical forcing in the upper layer, which contains a substantial amount of ozone, is so strong that it completely dominates the forcing due to the assimilation. In the tropics this leads to rather low stratospheric concentrations. Whereas the comparison of individual sondes show that the model profiles are qualitatively similar to the observed profiles, the statistical results seem to indicate that there are also quantitative differences. In particular, in the lower troposphere and stratosphere, the model has some artifacts. It is likely that these artifacts are due to an oversimplification in the representation of stratospheric and tropospheric ozone chemistry and surface deposition, a limited vertical resolution in the stratosphere, and therefore poorly resolved stratospheric dynamics.

## 3.11 Outlook

In the near future, ECMWF meteorological analyses will become available with a better vertical resolution in the stratosphere upto 0.1 hPa. We expect improvements to our model if these new input data are used. Apart from an increased number of vertical layers, a future version of the model may contain a more realistic description of chemistry, an improved horizontal resolution and a better description of stratospheric dynamics.

The assimilation model described in this study is a useful tool to generate global three-dimensional ozone analyses using satellite ozone column measurements as input. Since the model error growth is slow, it is also suitable for sparser data such as for example, total ozone data from the GOME instrument on board the ERS2 satellite. This has been done recently by *Eskes and Jeuken* [1999]. Some additional improvements to the TM3 model were added. Because the chemistry, as described in section 3.4, is strongly height dependent and TM3 contains only a few levels in the stratosphere, the chemistry calculations are done on an extended number of levels in the stratosphere. Ozone columns measured by GOME are much more accurate than those measured by TOVS. Whereas for TOVS an optimal forecast to observation error ratio of 0.55 is found (see figure 3.3) for GOME this ratio is 1.5 [*Eskes and Jeuken*, 1999].

The use of retrieved profile information from satellite measurements may be expected to improve the ozone analysis further. Currently ozone profiles are available from GOME [*Van der A et al.*, 1998]. These profiles have a good resolution in the stratosphere but contain approximately only two levels in the troposphere. It is planned to assimilate these profiles in TM3 as soon as also the extended ECMWF meteorology is available.

In this chapter, isotropic spatial error correlations were assumed. Dynamical structures in ozone are however fundamentally anisotropic. Therefore, a more realistic description of error covariances might improve the ozone analysis. In the Kalman-filter approach for instance the temporal and spatial evolution of the model error covariance is calculated explicitly [*Kalman*, 1960]. This requires transport of enormous matrices and therefore not directly suitable for use in global atmospheric models. In 4D-var no covariance matrix is explicit stored but the dynamical aspects of the error covariance are accounted for through the model dynamics. This concept has been applied by e.g. *Eskes et al.* [1999] for assimilation of GOME total ozone columns in the two dimensional AMK-model.

Satellite instruments like GOME and in the future SCIAMACHY are in principle able to measure many more species than just ozone. For instance, NO<sub>2</sub> and BrO are species which are currently retrieved from GOME measurements [*Burrows et al.*, 1999]. The MOPITT instrument launched in 1999 and SCHIAMACHI instrument scheduled to be launched in 2003 and will be able to measure additional gases like for instance N<sub>2</sub>O, CH<sub>4</sub> and CO. The availability of these extra species opens new possibilities for data assimilation in chemical transport models. Special attention should be given to the combination of retrieval and assimilation in the same model environment. The model can provide the first guess profile information required by the retrieval algorithm.



## Chapter 4

# Evaluation of vertical mixing and scavenging in a global tracer transport model using measurements of $^{222}\text{Rn}$ and $^{210}\text{Pb}$

*The work in this chapter has been performed in close cooperation with Hans Cuijpers of KNMI*

### 4.1 Introduction

The TM3 off-line chemical tracer transport model has gradually evolved from the TM2 model as developed by Heimann [Heimann, 1995] at the end of the eighties. This model was originally used to simulate the Carbon Dioxide cycle [Heimann and Keeling, 1989]. The original model resolution was  $8^\circ$  latitude by  $10^\circ$  longitude, with 9 vertical layers extending from the surface to 10 hPa and was usually transporting a single tracer. Later, a background photochemical scheme, containing 13 species of which seven were transported, was added to the model, to simulate the background chemistry of methane, ozone and  $\text{NO}_y$  species [Hein *et al.*, 1997]. This chemical version of the TM2 model was extended with extra layers in the tropopause region to be better able to simulate the influence of aircraft emissions [Velders *et al.*, 1994; Wauben *et al.*, 1997]. By adding the chemistry of higher hydrocarbons it became possible to use the model for simulations of polluted boundary layer chemical processes [Houweling *et al.*, 1998]. In the meantime the model resolution had been changed to 19 vertical levels [Rehfeld and Heimann, 1995], similar to the vertical levels of the ECMWF and ECHAM model and the convective transport was improved by including entrainment and detrainment in downdrafts. A description of the transport in the model can be found in Chapter 3. A recent evaluation of the performance of the

transport in the model can be found in *Dentener et al.* [1999].

Throughout the years the model was applied to studies of long-term trends of long-lived species like  $\text{CO}_2$ ,  $\text{CH}_4$ , tropospheric ozone, and the chemistry and transport of shorter-lived species like  $\text{NO}_x$ , isoprene,  $\text{SO}_2$  and ammonia. Especially the latter short-lived species require a better model description of transport and source and sink processes, since the variability on time scales larger or equal to the chemical lifetime should be represented. To be able to validate the description of transport and chemistry of short lived tracers, comparison with measurements of such tracers is needed.

Processes in the boundary layer, like emissions, deposition and turbulent transport, are contributing for a large part to the observed variability of short lived species. From a study in which the tracer transport of TM3 was evaluated with the radionuclide tracer  $^{222}\text{Rn}$  it was concluded that future work will have to concentrate on the improvement of the vertical diffusion scheme [*Dentener et al.*, 1999]. It was found that there is insufficient vertical mixing in the boundary layer, especially during night- and wintertime stable conditions. In the first section of this chapter an improved boundary layer vertical diffusion scheme will be introduced. Results of this new scheme will be validated against measurements of  $^{222}\text{Rn}$  and compared to the old scheme of *Louis* [1979] used in previous studies. Since  $^{222}\text{Rn}$  has no sinks other than its well known radioactive decay and since its source is within the boundary layer, it is well suited to validate boundary layer transport.

An important cause of the variability of water soluble tracers is cloud processing and removal by precipitation. In the second part of this chapter the wet removal scheme of TM3 will be tested by comparing model results with  $^{210}\text{Pb}$  measurements, the water soluble decay product of  $^{222}\text{Rn}$ .

$^{222}\text{Rn}$  and  $^{210}\text{Pb}$  are nowadays commonly used to test sub grid transport and scavenging [*Guelle et al.*, 1997a; *Wang et al.*, 1999; *D. J. Jacob et al.*, 1997].

## 4.2 Parameterization of sub-grid scale vertical turbulent transport

In most global tracer transport models sub-grid scale vertical transport by turbulent eddies is parameterized by vertical diffusion. Different approaches exist to model this vertical diffusion. The most widely used approach, is local gradient mixing (also called *K*-theory). In this approach the vertical flux of a conserved quantity, e.g. a (passive) tracer, is described as the product of a so called “turbulent eddy diffusivity” *K* and the local gradient of the transported quantity. *K* is parameterized as the square of a typical eddy length scale *l* times the local wind gradient and a functional dependence on the gradient Richardson number, a dimensionless quantity indicative of local atmospheric stability.

For unstable and convective conditions the size of turbulent eddies exceeds the typical layer height of model levels in the boundary layer. Under these circumstances turbulent transport is not well described by local quantities. In another often applied method [*Holtslag and Moeng*, 1991] a fixed shape of the *K*-profile is assumed, depending on non-local quantities as the boundary layer height and a typical turbulent velocity scale. An extra term is added to the local transport term [*Deardorff*,

1966], to account for counter-gradient transport observed under dry-convective conditions. The determination of the boundary layer height is critical in this approach. An advantage is that the  $K$  profile only depends on 2-dimensional (latitude-longitude) meteorological fields.

In most existing off-line models vertical diffusion of tracers is modeled in a similar way as vertical diffusion of moisture in numerical weather prediction (NWP) models. In, weather forecast models, however, there is a feedback of the turbulent transfer of heat, momentum and moisture on all other model processes. A wrong description of vertical diffusion will immediately leads to biases in the temperature and moisture, especially near the surface [Beljaars and Viterbo, 1998]. The combination of model and data in the data-assimilation of the NWP model enables a good validation of the parameterizations of vertical diffusion in these models.

It is more difficult to test the performance of boundary layer diffusion schemes in off-line tracer transport models. First of all sufficient measurements to validate tracer distributions are lacking. Furthermore, transport of tracers in the model is not accounted for by vertical diffusion alone, so it is difficult to separate, diffusion from other vertical transport processes. The diffusive tracer mass flux would be the appropriate quantity but it can hardly be validated. In addition, the dependence of the flux on  $K$  is nonlinear since it also depends on the local gradient of the tracer, which will be reduced by large diffusivities.

Wang *et al.* [1999] use measurements of the boundary layer height, Radon and methane to test their implementation of the Holtslag and Boville scheme in the Cambridge University off-line tracer transport model TOMCAT. They achieve a clear improvement in both the vertical distribution of Radon and the surface concentrations of Radon and methane compared to an older model version, which included the Louis [1979] local diffusion parameterization. Lee and Larsen [1997] used measured Radon profiles to study vertical mixing processes in the boundary layer.

In this section we investigate how the vertical mixing in TM3 can be improved. To do this we first will evaluate all steps in the calculation of vertical mixing by diffusion and summarize the main problems that are encountered in each step. Then we indicate improvements and discuss the resulting changes.

### 4.2.1 Limitations of the available meteorological data

Vertical diffusion coefficients are not directly available from the ECMWF archive of model analyses and forecasts, from which input data for TM3 usually are obtained. Therefore they are calculated in a preprocessing procedure at  $2.5^\circ$  by  $2.5^\circ$  resolution and 31 vertical levels and a time resolution of 6 hours, using the formulations by Louis [1979]. The input meteorological fields, profiles of wind and virtual temperature and surface fluxes of sensible and latent heat, are available from the ECMWF archive. There are fundamental difficulties associated with the use of NWP data for off-line models. The ECMWF model profiles of wind and temperature are partly a result of vertical mixing processes parameterized in the ECMWF model itself. It is therefore advisable to use consistent formulations in the TM3-preprocessing. This used to be the case when the TM3 model was developed. However, the ECMWF model parameterizations are constantly being updated. In addition, the ECMWF parameterizations are not developed to simulate the transport of tracers but rather the transport of heat, momentum and moisture. Although the focus is different, it is



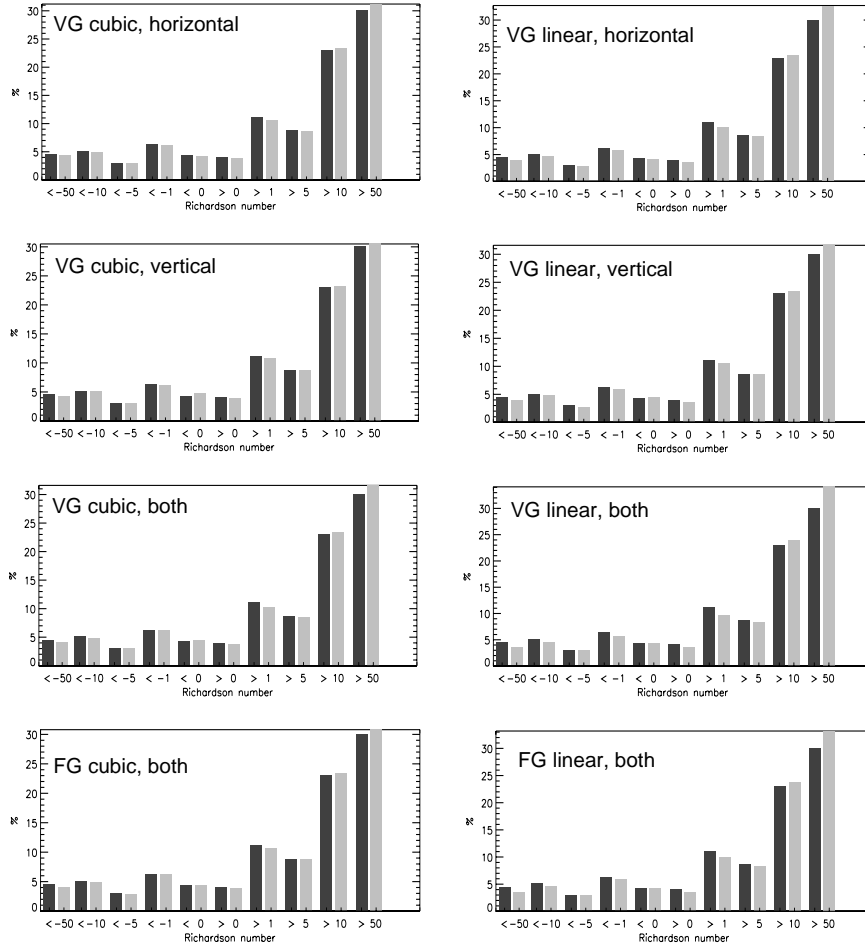


Figure 4.1: Comparison between ECMWF archived data (dark shading) and TM3 preprocessed data (light shading) for two resolutions ( $FG=5^\circ$  by  $3.75^\circ$  and  $VG=2.5^\circ$  by  $2.5^\circ$ ) and using different interpolation methods (linear and Hermite cubic interpolation). Vertically the wind and temperature profiles are interpolated from 31 to 19 hybrid levels. The percentage of grid cells per stability (indicated with the Richardson number) interval is compared. The comparison is done for 6 hourly global fields at a resolution of  $2.5^\circ$  by  $2.5^\circ$  below 2000 meter and cover 1 full day in January 1993.

assumed that this latter quantity is transported similarly as other gaseous tracers.

The obvious first step is to change the somewhat outdated Louis scheme in TM3 to the formulation currently employed in the ECMWF model. This formulation consists of two parts: for stable conditions a revised Louis approach is used, and for unstable conditions the scheme is adopted from [Holtslag and Boville, 1993]. The implementation of the new formulation is described in the next section.

As is often the case with parameterizations in global models, the calculation of the

diffusion coefficients is dependent on the resolution of the input data. To illustrate this we use the gradient Richardson number  $Ri$ , a quantity which is used in the calculations of the diffusion coefficients and which is sensitive both to temperature and wind gradients.  $Ri$  is defined as:

$$Ri = \frac{g}{\theta_v} \frac{\partial \theta_v / \partial z}{\partial U^2 / \partial z^2} \quad (4.1)$$

with  $\theta_v$  the virtual potential temperature and  $U$  the wind velocity. We have calculated  $Ri$  from data directly retrieved from the ECMWF archive and from interpolated data on various TM3 resolutions. Figure 4.1 shows that in general due to the horizontal and vertical interpolation of wind and temperature relatively more grid cells end up at the stable end of the range of Richardson numbers. This is not desirable, since it implies that on average there will be less mixing under stable conditions. In principle it would be advantageous to calculate  $K$ -values not in the preprocessing but on-line since it would reduce the IO by one 3-D field. However, to avoid this particular dependence on resolution we decided to calculate the  $K$ -values in the preprocessing step at the input resolution of the ECMWF fields. We realize that also this resolution is well below the original ECMWF model resolution, which currently is about  $0.5^\circ$  by  $0.5^\circ$ . Non-local schemes will be much less resolution dependent, since they are less influenced by local gradients. The dependence on resolution is a well known and difficult to solve problem for the parameterization of sub-grid scale fluxes [Beljaars, 1991; Mahowald *et al.*, 1995].

Another shortcoming of off-line models is the limited temporal resolution of the input data. In TM3 every 6 hours new meteorological fields are read and used for six hours. No interpolation in time is applied. Since there is a pronounced daily cycle in the diffusion coefficients, systematic errors are made by sampling only at 6 hour intervals. Since new values are read at universal time, this systematic error is different for different locations. Figure 4.2 illustrates the time resolution problem for the calculation of the boundary layer height, which is a crucial parameter in the Holtslag and Boville scheme. As can be seen, for instance at locations where the sensible heat flux is maximum at 12 UTC, the boundary layer height and therefore also mixing is underestimated for the major part of the day. At another hypothetical location the opposite can happen.

In order to resolve better the daily cycle of the boundary layer height and turbulent diffusion, we decided to increase our time resolution for the calculation of diffusion coefficients to 3 hours. For this purpose we use the 3 and 6 hour forecast values of ECMWF surface fluxes together with 6 hourly temperature and wind fields linearly interpolated to 3 hourly intervals. Although, we still can not preclude discretization errors, considerable improvement is achieved compared to the old situation.

To summarize, the following requirements are posed to the new scheme:

- Mixing under stable conditions should be better represented, which means that it should increase relative to the old scheme.
- Under unstable conditions the mixing should be described more realistically, by using non-local quantities to describe the  $K$ -profile instead of local gradients.
- The new formulations should be less sensitive to the chosen resolution in space and time.

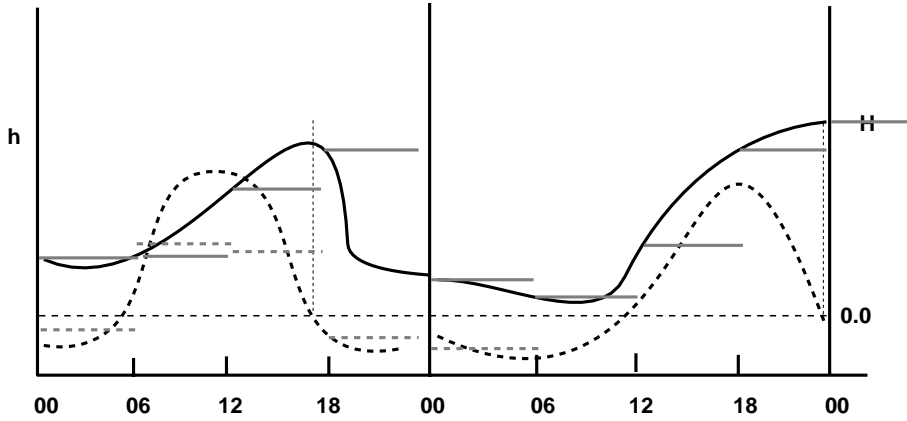


Figure 4.2: Schematic representation of the daily cycle of the surface heat flux  $\mathbf{H}$  (dashed line) and boundary layer height  $\mathbf{h}$  (bold line) and the TM3 model representation with a 6 hour time step (grey lines). Two fictitious cases are shown.

#### 4.2.2 Vertical diffusion formulation

The vertical flux of a tracer due to vertical diffusion can be described as [Holtslag and Boville, 1993]:

$$\overline{w'C'} = -K_c \left( \frac{\partial C}{\partial z} - \gamma_c \right) \quad (4.2)$$

, in which  $K_c$  is the eddy diffusivity for the tracer and  $\gamma_c$  represents the counter gradient transport due to dry convection. This term is unimportant under stable or neutral conditions.  $\gamma_c$  contains a dependence on the surface flux of the scalar quantity  $C$ . For moisture or heat this flux is easily prescribed, however for a chemical tracer it is more complex. The flux at the surface depends on complex local emission and deposition processes, which are different for each species and often not known with enough detail. For example for  $\text{SO}_2$  most emissions are from point sources while the dry deposition flux is relatively constant over the grid box surface area. Simply taking the average of these two fluxes leads to errors of similar or larger magnitude as would the omission of the local term lead to. In addition comparisons with large eddy simulations (Hans Cuijpers, pers. communication) show that the influence of the counter gradient term is only small. Therefore we decided to set:  $\gamma_c = 0$ .

In the free troposphere we use for  $K_c$  the traditional formulation [Louis et al., 1982]:

$$K_c = l_c^2 \frac{\partial U}{\partial z} F_c(Ri) \quad (4.3)$$

, where  $F_c$  denotes the functional dependence of  $K_c$  on the gradient Richardson number (see equation 4.1).  $l_c$  is the turbulent length scale, which can be diagnostically

determined from:

$$l_c = \frac{1}{\frac{1}{kz} + \frac{1}{\lambda_c}} \quad (4.4)$$

Here  $k = 0.41$  is the Von Karman's constant,  $\lambda_c$  is the asymptotic length scale, giving a maximum value for the size of the turbulent eddies. The determination of  $\lambda$  is not straightforward and depends on the local stratification. For heat it was assigned a typical value of 450 meters by [Louis, 1979]. This value might be appropriate for the boundary layer, but in the free troposphere it is much too large. Therefore Holtslag and Boville defined  $\lambda_c = 30 + 270 \exp(1 - z/1000)$ , which gives a value of 300 meters at 1000m and 30 m at the top of the atmosphere.

For  $F_c$  we take for stable conditions:

$$F_c = \frac{1}{1 + 10Ri(1 + 8Ri)} \quad (4.5)$$

and for unstable conditions:

$$F_c = 1 + 18Ri \quad (4.6)$$

Within the PBL we use for  $K_c$  [Holtslag and Boville, 1993]:

$$K_c = kw_tz(1 - \frac{z}{h})^2 \quad (4.7)$$

with  $w_t$  a characteristic turbulent velocity scale which is independent of height, and  $h$  is the boundary layer height. We use the method of *Vogelezang* [1996] to determine the boundary layer height  $h$  in an iterative procedure with the criterion that  $h$  is found when the Richardson number for the gradient between level  $h$  and the surface layer  $z_1$  is larger than a critical Richardson number  $Ri_{crit} = 0.3$ :

$$h - z_1 = \frac{Ri_{crit}[(u_h - u_1)^2 + (v_h - v_1)^2 + bu_*^2]}{g/\theta_{v1}(\theta_{vh} - \theta_{vs})} \quad (4.8)$$

Subscript 1 indicates the first model layer, subscript h indicates the model layer at the top of the boundary layer. With each iteration h is increased.  $u_*$  is the friction velocity.  $\theta_{vs}$  is an offset temperature near the surface. The influence of the choice of  $\theta_{vs}$  on the boundary layer height is discussed in *Vogelezang* [1996]. We use for  $\theta_{vs}$  the virtual potential temperature at the lowest model level ( $\pm 30$ m). For unstable conditions within the surface layer ( $=0.1h$ ) we use:

$$w_t = \frac{u_*}{\phi_H} \quad (4.9)$$

with  $\phi_H$  the stability correction function for heat [Holtslag and Boville, 1993]. For unstable conditions outside the surface layer we use:

$$w_t = \frac{w_m}{Pr}, \quad w_m = \frac{u_*}{\phi_m} \quad (4.10)$$

with  $\phi_m$  the stability correction function for heat and  $Pr$  the Prandtl number. Since we have omitted the counter-gradient term, a formulation different from the original

one for  $Pr$  is needed which is consistent with equation 4.2. We therefore use the formulation for  $Pr$  given by Holtslag and Boville for  $z/h = 0.1$  throughout the whole boundary layer.

Similar to the procedure in the ECMWF operational weather forecast model, in TM3 the non-local formulation is applied for unstable conditions only. For stable conditions a local formulation given by equation 4.3 is used. The stability function  $F_c$  has been adjusted, since the old formulation [Louis *et al.*, 1982] appeared to give too little mixing for heat, resulting in a surface temperature bias. The new formulation is [Beljaars and Viterbo, 1998]:

$$F_c(Ri) = \frac{1}{(1 + 10Ri\sqrt{1 + Ri})} \quad (4.11)$$

### 4.2.3 Results

In order to test the new vertical diffusion scheme, we compare model output from a simulation using this new scheme (**W3**) both with observations and with output from a simulation using the old Louis parameterization (**W1**). Figure 4.3 shows the daily cycle and variation of the boundary layer height at various locations around the globe. In all cases the development of the boundary layer height looks realistic for the time of the year and the location. At continental locations with high surface heat fluxes (e.g. Alice Springs) there is a pronounced daily cycle in the boundary layer height reaching maximum values in the late afternoon. A typical cold winter situation is encountered at Yellowknife, where the boundary layer does not exceed its prescribed minimum value of 100 meters. Over the ocean (e.g. The Azores) the height of the boundary layer does not vary strongly from day to night. Advection of cold or warm air is the main determining factor here. Figure 4.3 also shows that with a 6 hour time resolution the development of the boundary layer is not well described and that in some cases the height can be severely underestimated (e.g. Khartoum). Comparison (Figure 4.4) of model calculated boundary layer heights with observed heights from an aerosol lidar and radiosonde temperature profiles for a site in the Netherlands shows that in general the model estimated boundary layer height is too low. However, also the radiosonde and lidar estimated height differ considerably, the lidar measurements being in best agreement with the model calculations. The most prominent differences in the  $K$ -values itself are found in the free troposphere where there is too much diffusion in the old scheme. This is clearly shown in figure 4.5 where the differences between TM3 Radon concentrations from simulations with the old scheme and the new scheme have been plotted. With the old diffusion scheme we find much higher concentrations in the upper troposphere, especially near the subtropical jet, and stratosphere. This is a result of upward mixing of Radon, which was probably too strong due to the overestimation of the mixing length ( $\lambda_c$  in Equation 4.4) in the Louis parameterization.

In general the new diffusion scheme produces larger diffusion coefficients close to the surface and somewhat smaller values higher up in the boundary layer. For almost the whole globe the Radon surface layer concentrations over the continents are substantially smaller when the new vertical diffusion scheme is used. The difference with the old scheme can amount to more than 50 %.

In order to evaluate the new scheme further we compare with measurements. Fig-

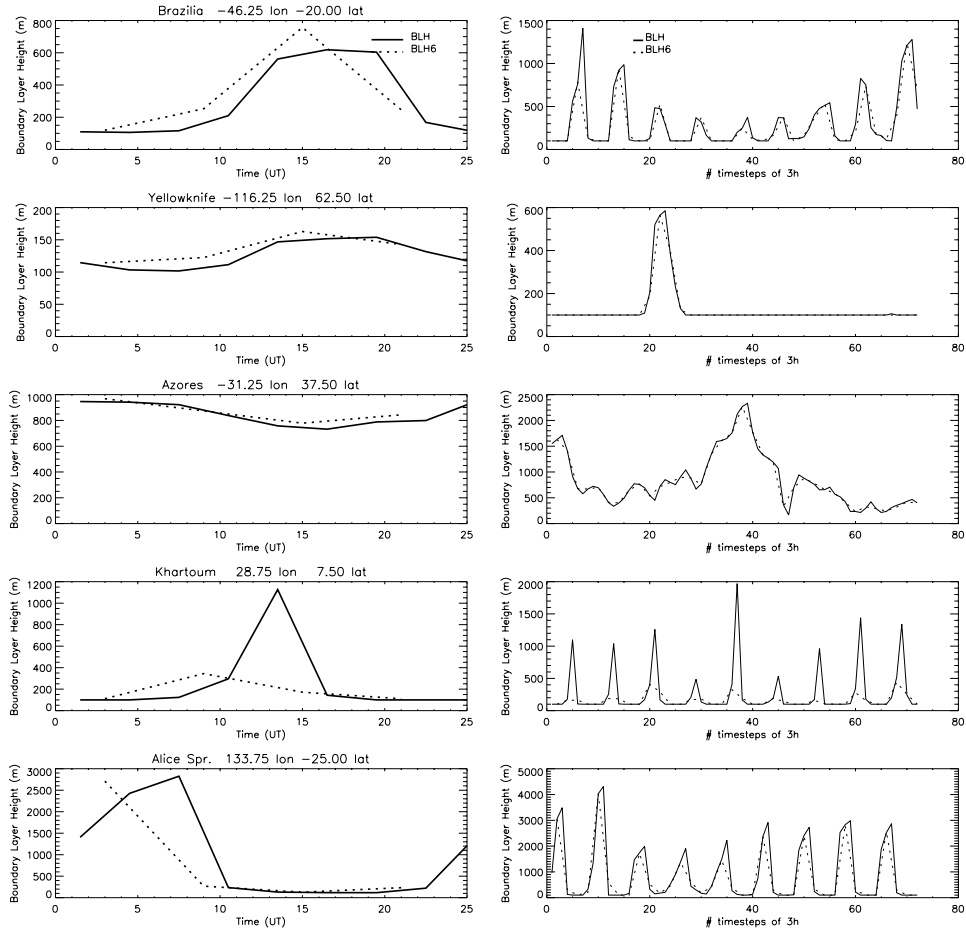


Figure 4.3: Time serie of the boundary layer height (right) and ten day average diurnal cycle (left) at various locations as calculated from the TM3 preprocessing for January 1997. Results for preprocessing with 3 (BLH) and 6 (BLH6) hour intervals are shown.

ure 4.6 shows the monthly averaged differences of  $^{222}\text{Rn}$  concentration measurements at 4 sites with two model simulations: One with the old Louis 6-hourly diffusion coefficients (**W1**) and one simulation done with the new 3-hourly calculated coefficients (**W3**). The model simulations are done at a resolution of  $3.75^\circ$  by  $5^\circ$  and 19 vertical levels. The measurements are a representative subset of the data used by *Dentener et al.* [1999]. Except for Freiburg and Schauinsland, most sites are at remote locations, at islands, well away from the continents where Radon is emitted. For remote stations the difference between the results of both model simulations is small. For the two continental sites Freiburg and Schauinsland the differences are more pronounced. Two reasons for this apparently weak impact of the new boundary layer scheme at remote sites can be identified. First of all, since there are no emissions close to the remote sites, the concentrations are mainly determined by long range transport and not by boundary layer mixing. Secondly, over the oceans, the atmospheric stability

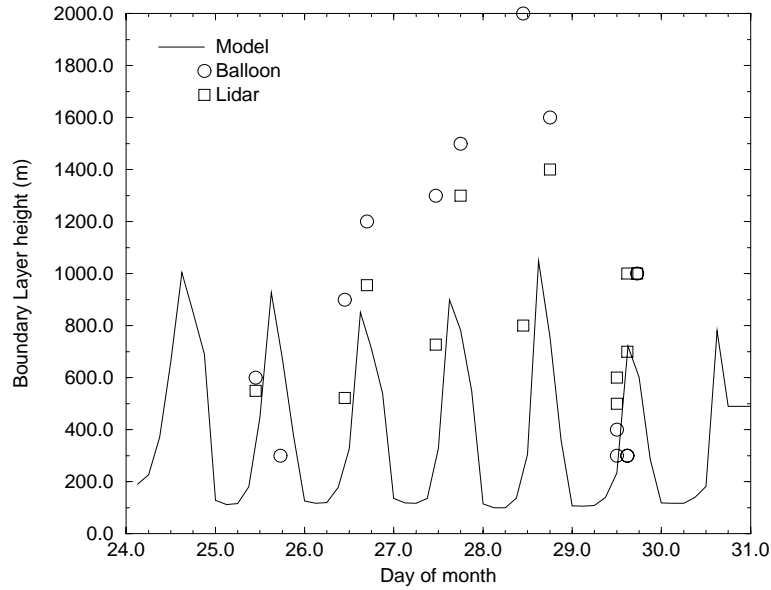


Figure 4.4: Time serie of the boundary layer height at Bilthoven for June 1995

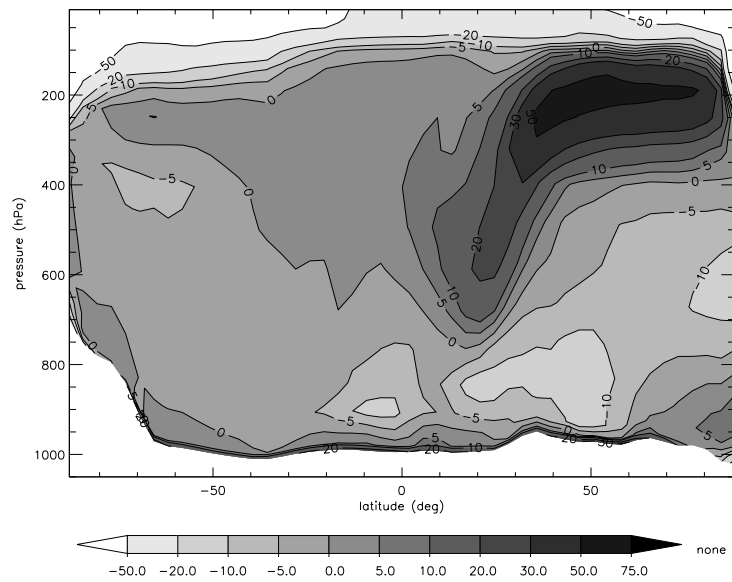


Figure 4.5: Relative difference (%) in zonally averaged  $^{222}\text{Rn}$  concentrations, Old (W1) - New (W3) vertical diffusion scheme for December 1993

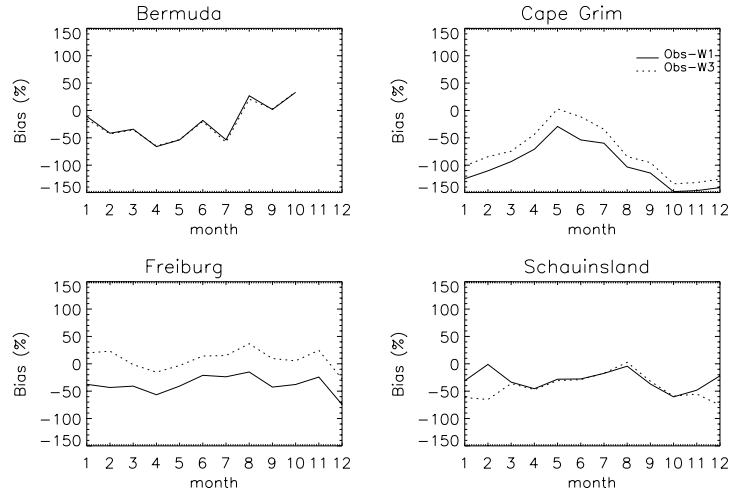


Figure 4.6: *Seasonal cycle for the difference model-measurement (W1 solid and W3 dotted line) for 1993*

is near neutral. Differences between the old and new scheme would occur under more stable and more unstable conditions. This is the case over land, where the emissions occur at the surface and where there is a strong diurnal and seasonal cycle in stability.

At Freiburg the Radon concentrations are overestimated with the old boundary layer scheme, resulting in too high Radon concentrations. By using the new scheme, the relative overestimation of observed concentrations at Freiburg is reduced from 50 % to about 0 % for the whole year. At Schauinsland, which is in same grid cell but at a different model level, the agreement with observations is worse in winter. This could indicate that the mixing directly at the surface has improved, but that it is too small higher up in the boundary layer. This is in agreement with the results presented in Figure 4.5 which shows a decrease of mixing towards higher altitudes. It should be noted however that the exact choice of the correct altitude presents some difficulties since Schauinsland is located on top of a hill. Therefore it may to some extent sample air originating from down-slope regions. One may not expect the simple boundary layer parameterization we use to capture the complicated interaction between boundary layer height and local flows around hills. In any case, model Radon values over land are quite uncertain because of the unknown local variability of emissions. We note that there is a significant improvement at Cape Grim, Tasmania, which is relatively close to the Australian continent. However, Bermuda, another station which is close to a continent, does not show such improvement (Figure 4.6).

Since there is a strong day-night variability in the development of the boundary layer we also compared our model results to observed day-night differences in Radon concentrations (see figure 4.7). It is clear that at nearly all sites the daily cycle in Radon surface concentrations has improved considerably. Most of this improvement can be attributed to the better time resolution in the new boundary layer scheme. As can be seen in figure 4.7 in the old scheme in the morning the surface concentrations show a peak value that is too large and too late. Even for Schauinsland, where gen-



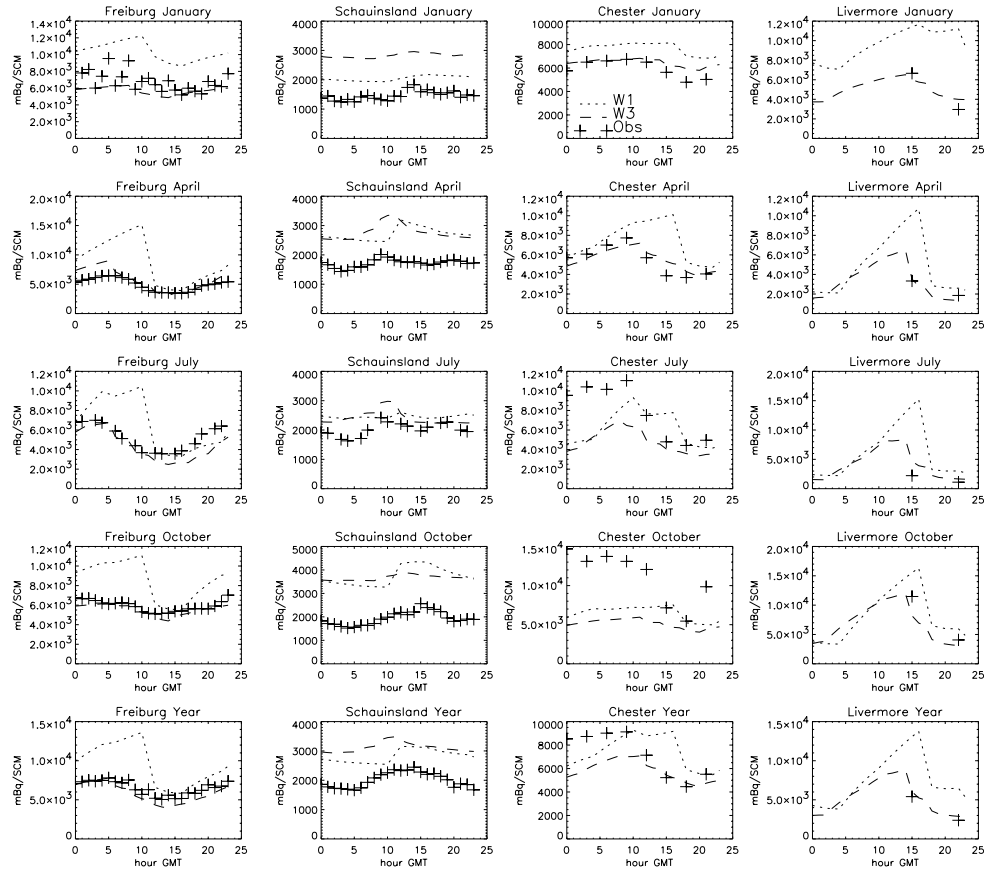


Figure 4.7:  $^{222}\text{Rn}$  monthly and annual averaged daily cycle for a few continental sites. Values for Chester and Livermore are taken from Gesell [1983]

erally model concentrations are too high, the maximum and minimum concentrations are better timed in the new model version.

To further evaluate the mixing characteristics the model results were compared with aircraft measurements at two locations at the edge of the North American continent, in California [Kritz *et al.*, 1997], and Nova Scotia [Zaucker *et al.*, 1996]. Results are shown in figures 4.8 and 4.9. These measurements are one of the few profile measurements, which are available for Radon over the last 10 years. The model results have been interpolated to the specific time and location of the measurements. Both model runs simulate the vertical profiles and the day-to-day variability herein reasonably well. Results for Moffett Field are substantially better than for the NARE campaign. No clear difference between the two model simulations can be observed from the comparison of individual profiles, especially in the free troposphere. However, the correlation between model and measurements calculated for all flights is substantially better for the model simulation with the new vertical diffusion scheme.

The profiles also show that the Radon concentrations in boundary layer are over-

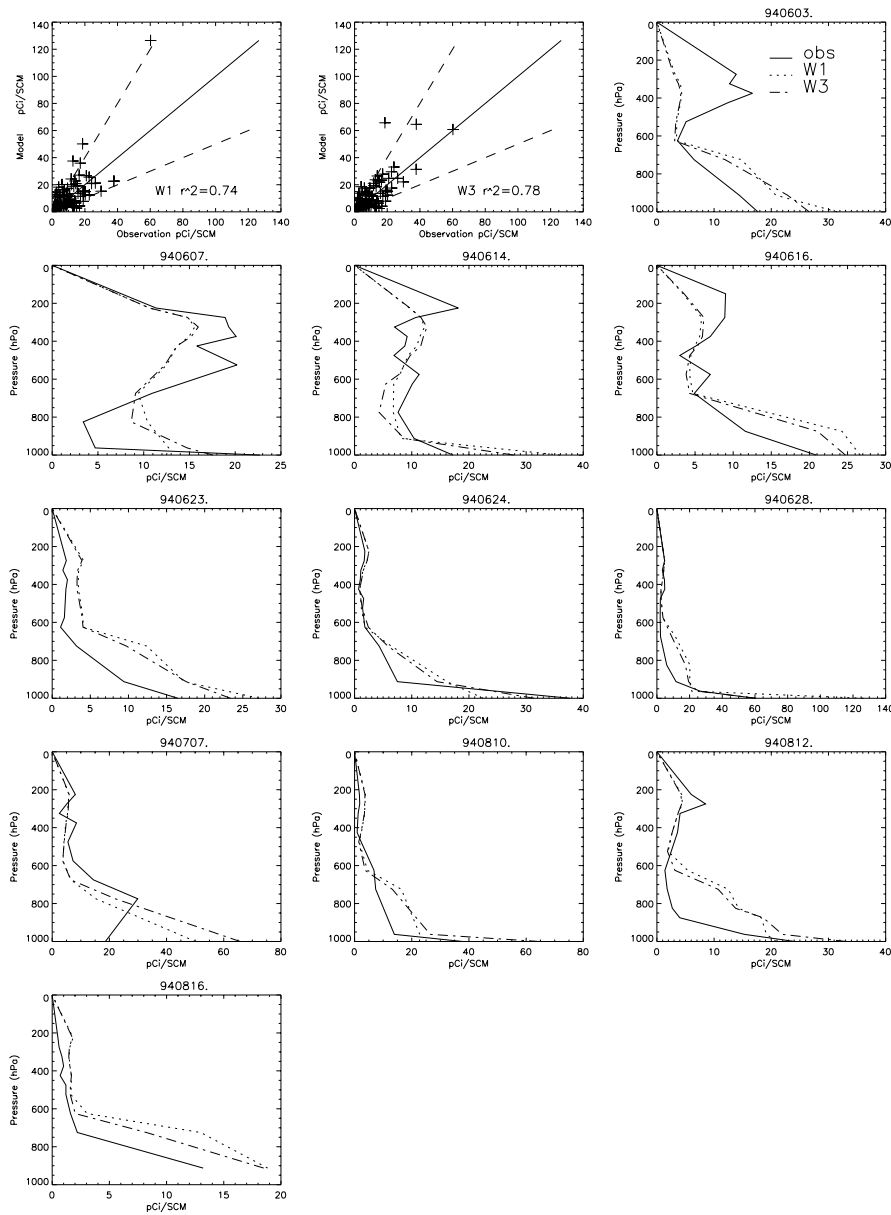


Figure 4.8:  $^{222}\text{Rn}$  profiles at Moffett Field ( $37.4^\circ\text{N}$ ,  $122.0^\circ\text{W}$ ) for different flights in June and July 1994.

estimated by both model simulations. The reason for this might be that the grid box average diffusion coefficients are too low or that the grid box average emission is too high. “Grid box average” is stressed here since for both locations there is a land-sea transition within the model grid box. It is always difficult for a model to represent the average for a grid box with such extremely different surface characteristics correctly.

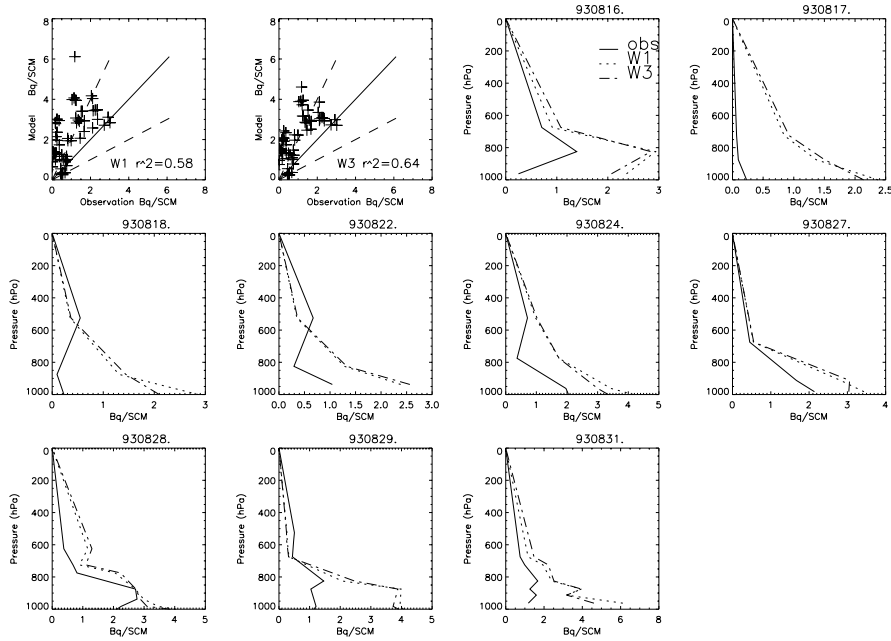


Figure 4.9:  $^{222}\text{Rn}$  profiles during the NARE campaign ( $44^\circ\text{N}$ ,  $66^\circ\text{W}$ ) for different flights in August 1993.

It could be that in reality the atmosphere over land is stable, while it is unstable over sea, resulting in total different mixing over land and sea. In the model, however, only one value is used for the vertical mixing, depending on the average surface virtual heat flux. Therefore more profile measurements of Radon over homogeneous, preferably land, surfaces are needed. In addition it should be stressed that while in the model Radon emission rates are assumed to be constant with  $1\text{ atom cm}^{-2}\text{ s}^{-1}$ , they are in reality dependent on soil type and soil wetness ranging from  $0.1$  to  $2.5\text{ atoms cm}^{-2}\text{ s}^{-1}$  [Turekian *et al.*, 1977].

### 4.3 Scavenging

For accumulation range ( $0.1\text{-}2\mu\text{m}$ ) aerosol particles, wet scavenging by precipitation is the main removal mechanism. In contrast with coarse particles, the settling velocity is so low that gravitational settling does not play a role. Measurements show that important aerosol species such as sulfate are mainly present in this accumulation range aerosol [Wang and John, 1988]. Also for important soluble gases as  $\text{HNO}_3$  and  $\text{H}_2\text{O}_2$  wet scavenging is a main removal mechanism. The global distribution of water soluble gases and aerosol is highly dependent on the global distribution of precipitating clouds. On average merely one tenth of all clouds is in a precipitating state. Moreover, the global average precipitation efficiency is about 50 % which means that half of the amount of water entering a precipitating system reaches the surface.

Also for the calculation of scavenging rates we need ECMWF input fields for TM3.

The ECMWF model distinguishes between two types of precipitation: convective and large scale. Only the precipitation at the earth's surface is stored. The vertical distribution of the precipitation therefore has to be estimated in an other way.

In many models no distinction is made between convective and large scale scavenging. In these models scavenging is parameterized as a first order removal process. However, such an approach fails to capture the rapid processing of air in a convective updraft during a model time step, which increases the total mass of soluble tracer exposed to precipitation [Xing and Chameides, 1990]. Therefore, scavenging by convective precipitation is calculated in TM3 as part of the mass flux entrained in convective clouds. We apply a scavenging efficiency  $\eta$  to the updraft massflux of the convective cloud ensemble. We adopt the values of Balkanski *et al.* [1993] and Guelle *et al.* [1997b] for  $\eta$  which is 50% for shallow convection and 100% for deep convection. In practice this means that a well soluble tracer in a deep wet convective event is removed completely from the updraft mass flux. The combination of convective mass transport and rainout prevents a soluble tracer to be pumped in a convective updraft and disperse at the top without experiencing sufficient scavenging [Balkanski *et al.*, 1993].

The scavenging of tracers by large scale precipitation can be written as a first order removal process:

$$\frac{dC}{dt} = -\beta_{lsp}C \quad (4.12)$$

, with  $\beta_{lsp}$  the scavenging rate expressed in  $s^{-1}$  and  $C$  the tracer concentration. We separate the scavenging by large scale precipitation into two different processes: in-cloud and below-cloud scavenging. For large scale in-cloud scavenging the rate is mainly dependent on the local precipitation formation rate. Following Roelofs and Lelieveld [1995] The scavenging coefficient  $\beta$  ( $s^{-1}$ ) for a completely soluble gas ( $HNO_3$ ) is calculated as follows:

$$\beta_1 = \frac{3D_g L_c}{r_c} \quad (4.13)$$

$$\beta_2 = P_f L_c \quad (4.14)$$

$$\beta_{inc} = \frac{1}{\beta_1^{-1} + \beta_2^{-1}} \quad (4.15)$$

with  $P_f$  the precipitation formation rate ( $kg\ m^{-3}\ s^{-1}$ ),  $L_c$  the grid box averaged liquid water content ( $kg\ m^{-3}$ ),  $D_g$  the gas phase diffusion coefficient ( $m^2\ s^{-1}$ ),  $r_c$  the average cloud drop size in a rain-cloud (estimated as  $r=20\ \mu m$ ). The final in-cloud scavenging rate  $\beta_{inc}$  is determined by the slowest of the two processes with rates  $\beta_1$  and  $\beta_2$ . Uptake of gases by cloud droplets, ( $\beta_1$ ) is the limiting factor only at low liquid water concentrations and high precipitation formation rates. The rate conversion of cloud water to precipitation ( $\beta_2$ ) is in almost all situations the rate determining step. Since it is assumed that all aerosol particles act as cloud condensation nuclei,  $\beta_1$  does not apply to aerosol.

Below-cloud scavenging of gases by falling raindrops is parameterized as a function of raindrop radius, the velocity of falling drops and molecular diffusion. The equation

for the scavenging coefficient  $\beta_{bc}$  is very similar to that of the mass transfer part of the in-cloud scavenging. The difference is that for rain drops the mass transfer from the gas phase to the falling droplet is rate determining and strongly depends on the above mentioned factors.

$$\beta_{bc} = \frac{3k_c L_{rain}}{r_d} \quad (4.16)$$

with  $k_c$  ( $\text{m s}^{-1}$ ) the mass transfer coefficient,  $L_{rain}$  the dimensionless rain liquid water content and  $r_d$  the rain droplet radius (m).

The flux of a gaseous species to a raindrop can be expressed as the product of the mass transfer coefficient and the concentration difference between the gas phase and the rain droplet's surface. For a well soluble gas the assumption that the concentration at the droplet's surface equals zero is quite valid [Seinfeld, 1986]. The mass transfer coefficient for a sphere is given by an empirical relationship depending on the Schmidt and Reynolds numbers:

$$k_c = \frac{D_g}{2r_d} (2 + 0.6Re^{1/2}Sc^{1/3}), \quad Re = 2r_d V_t / D_a, \quad Sc = D_a / D_g \quad (4.17)$$

with  $D_a = 0.133$  ( $\text{cm}^2 \text{s}^{-1}$ ) the diffusion coefficient of air at standard pressure and temperature and  $V_t$  the terminal velocity of falling raindrops, which can be calculated using an empirical relationship depending on the droplet radius  $r_d$  [Seinfeld, 1986]. The two major unknown variables  $r_d$  and  $L_{rain}$  are parameterized as a function of the rainflux, using the empirical formulae proposed by Mason [1971].

The below-cloud scavenging of aerosols strongly depends on the size of the particles. Sulfate aerosol is mostly present in the accumulation mode particle range for which below-cloud scavenging is not very efficient. We adopt a scavenging efficiency of  $0.05 \text{ mm}^{-1}$ , taken from Dana and Hales [1991], for a lognormal background aerosol distribution with  $r = 0.13 \mu\text{m}$ ,  $\sigma = 1.9$  [Jaenicke, 1988] and a frontal rain spectrum with a geometric mean radius  $R_g$  of  $0.02 \text{ cm}$  with  $\sigma = 1.86$ . It should be noted that the scavenging coefficient is strongly dependent on the actual choice of  $r$  and  $\sigma$ .

As mentioned the ECMWF archive does not have any information about the vertical distribution of precipitation. We define the precipitation at the bottom of level  $k$ ,  $R^k$  ( $\text{kg m}^{-2} \text{s}^{-1}$ ), as:

$$R^k = R^{k+1} + P_f^k h^k \quad (4.18)$$

with  $P_f^k$  the precipitation formation rate ( $\text{kg m}^{-3} \text{s}^{-1}$ ) in layer  $k$  and  $h^k$  the layer height (m). From the top to the bottom of a precipitating cloud  $R^k$  is accumulated assuming that no evaporation of precipitation occurs.

We calculate the precipitation formation rate from the 3-dimensional fields of cloud ice and liquid water content, using similar parameterizations as used in weather prediction models [Tiedtke, 1993]. Precipitation by liquid and ice water clouds is formed via two fundamentally different processes. For liquid clouds the precipitation formation rate increases with increasing liquid water content  $q_{cl}$  ( $\text{kg/kg}$ ) according to:

$$P_{cl} = q_{cl} c_0 [1 - e^{-(q_{cl}/q_{cr})^2}] \quad (4.19)$$

with  $c_0$  ( $\text{s}^{-1}$ ) the rate of conversion of cloud drops to rain drops, and  $q_{cr}$  a typical cloud liquid water content at which rain is starting to be efficiently produced [Sundquist

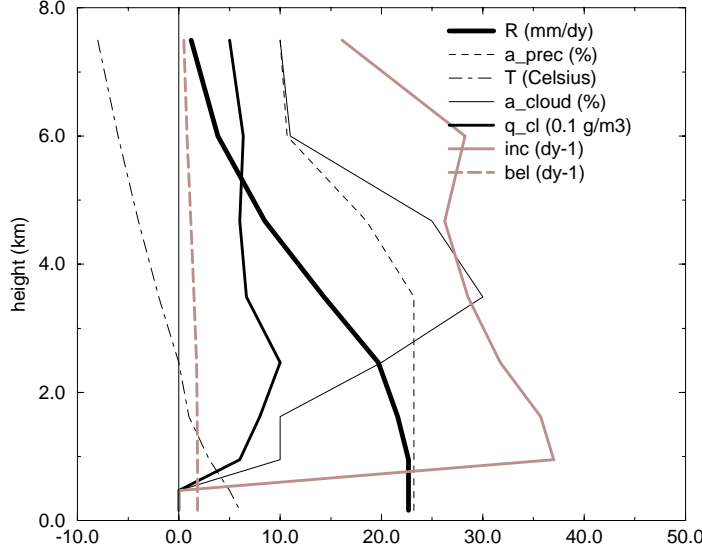


Figure 4.10: Vertical profile of precipitation ( $R$ ), rain cover ( $a_{prec}$ ), in-cloud ( $inc$ ) and below-cloud ( $bel$ ) scavenging, for a given distribution of temperature ( $T$ ), cloud cover ( $a_{cloud}$ ) and cloud liquid water content ( $q_{cl}$ ) for a typical frontal rain-cloud.

*et al.*, 1989]. The formulation of  $c_0$  takes into account the effect of collection of cloud droplets by raindrops falling through the cloud ( $F_1$ ) and the Bergeron-Findeisen mechanism ( $F_2$ ):

$$c_0 = c_0^* F_1 F_2, \quad (4.20)$$

$$F_1 = 1 + b_1 \sqrt{R_{loc}} \quad (4.21)$$

$$F_2 = 1 + b_2 \sqrt{T_{Berg} - T}, \quad T_{ice} < T < T_{Berg} \quad (4.22)$$

$R_{loc} = R^{k+1} / a_{prec}$  is the local precipitation rate and  $T_{berg} = 268$  K is the temperature at which the Bergeron-Findeisen mechanism starts to enhance the precipitation. The constants  $b_1, b_2$  and  $c_0^*$  are taken from *Sundquist et al.* [1989]. The grid box fraction  $a_{prec}$  over which precipitation occurs is parameterized such that it at least equals the precipitation fraction of the above grid cell and that it increases with the relative increase of local precipitation, taking into account the local cloud cover.

For ice clouds the precipitation formation  $P_{ci}$  is calculated from the divergence of the ice flux density :

$$P_{ci} = g \frac{\partial}{\partial p} (V_{ti} \rho_a q_{ci}) \quad (4.23)$$

with  $V_{ti} = \alpha(\rho_a q_{ci})^\beta$  is the terminal velocity of ice crystals,  $q_{ci}$  the ice water content,  $p$  pressure and  $\rho_a$  the air density. The constants  $\alpha$  and  $\beta$  are obtained from a fit through observations [Heymsfield and Donner, 1990]. The total precipitation formation rate is  $P_f = P_{cl} + P_{ci}$ .

Figure 4.10 shows the vertical profile of scavenging of a completely soluble gas and precipitation for a hypothetical rain cloud, consisting of liquid water only. The profiles are calculated with equations 1.13 - 1.22 for prescribed profiles of temperature, cloud liquid water and cloud cover.

Starting at the top of the cloud, the in-cloud scavenging rate first increases rapidly from 8 to 6 km to a value of  $30 \text{ day}^{-1}$  due to the enhancement of precipitation formation by  $F_2$  the Bergeron-Findeisen mechanism (Eq. 1.22). Below 3 kilometer, the cloud liquid water content decreases while the in-cloud scavenging rate increases. This is due to the influence of the local precipitation falling through the cloud (term  $F_1$  in Eq. 1.21). The below-cloud scavenging is much smaller than the in-cloud scavenging and increases with increasing precipitation flux.

### 4.3.1 $^{210}\text{Pb}$ simulations

The radionuclide  $^{210}\text{Pb}$  is a decay daughter of  $^{222}\text{Rn}$ . Because of its low vapor pressure it attaches indiscriminately to aerosol surfaces; its size distribution is concentrated in the 0.1 to 1 micron range. Because of this behaviour it is a good tracer to test the model performance with respect to non-chemical removal of aerosols in the above mentioned size range (e.g. sulfate) [Balkanski et al., 1993; Guelle et al., 1997a]. Moreover many deposition flux and concentration measurements exist for locations over the whole globe [Larsen et al., 1995; Preiss et al., 1996].

We perform  $^{210}\text{Pb}$  simulations with the TM3 model by allowing  $^{222}\text{Rn}$  emissions to radioactively decay to  $^{210}\text{Pb}$ . Wet and dry removal of  $^{210}\text{Pb}$  is treated exactly the same way as if it were sulfate aerosol. No distinction is made between the in-cloud scavenging by ice or liquid clouds and between the below-cloud scavenging by rain or snow.

We have performed two simulations at a resolution of  $5^\circ$  longitude by  $3.75^\circ$  latitude. One, which included the detailed scavenging scheme, described in the previous section (**W3**) and one using the old and much simpler scavenging scheme (**W2**) [Langner and Rodhe, 1991] which was used in an older version of the model. In this scheme:

$$\beta_{tot} = P^k / L^k, \quad P^k = R^{surf} g^k \quad (4.24)$$

in which  $\beta_{tot}$  is the total scavenging rate for the sum of convective and large scale precipitation,  $P^k$  is the precipitation formation rate at level  $k$ .  $P^k$  is a function of the surface precipitation  $R^{surf}$  and a seasonal and a normalized zonal averaged climatology  $g^k$  of the vertical distribution of the precipitation formation rate.  $g^k$  is taken from climate model output [Newell et al., 1974]. The new vertical diffusion scheme as described in previous section has been used in both model simulations.

Hence the main differences between the old and new formulation are the treatment of the convective removal and the vertical and zonal distribution of scavenging rates. In the new scheme there is a direct coupling between precipitation and the occurrence of clouds and convection. In the old scheme the cloud fields are not involved in

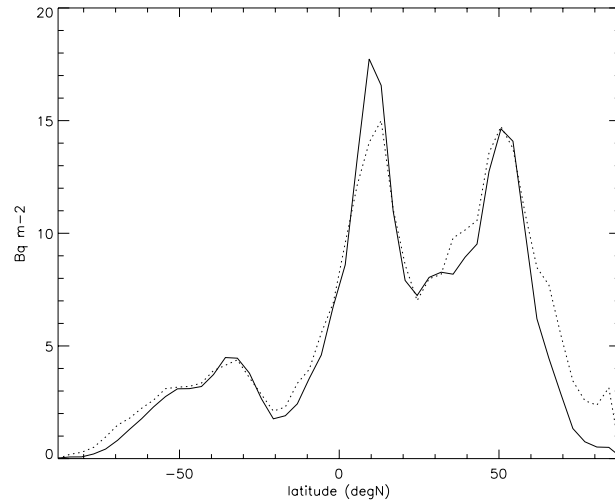


Figure 4.11: Comparison of zonally averaged deposition of  $^{210}\text{Pb}$  for model simulation **W2** (bold line) and **W3** (dashed line) for July 1993.

the calculation of the vertical scavenging distribution. In addition, the below-cloud scavenging is not considered in the old scheme.

If we compare the zonal averaged distributions of  $^{210}\text{Pb}$  wet deposition of both model simulations we hardly find any differences (Figure 4.11). Compared to the old scheme the new scheme results into somewhat higher deposition in the polar regions and slightly less deposition in the tropics. We have also compared the simulated total deposition for the year 1993 with annual bulk deposition measurements at various sites [Preiss *et al.*, 1996]. Dry deposition is accounting for about 14% of the total deposition [Balkanski *et al.*, 1993]. Figure 4.12 shows scatter plots of model results versus measurement for both simulations **W2** and **W3**. Model values have been interpolated to the measurement location. As we would expect from the results in Figure 4.11 results for the different schemes are not very different. The linear regression statistics show that both model simulations slightly overestimate the measured deposition flux. The small difference between results of the two model simulations indicates that the deposition is mainly sensitive to the location of the precipitation and much less to the vertical distribution of scavenging rates.

Figure 4.13 shows that although there are small differences between simulation **W2** and **W3** in the accumulated deposition amounts, concentration differences are much larger. Over almost the entire troposphere the concentrations are 1.5 times lower with the new scavenging scheme. Only in the tropics between 700 and 400 hPa the opposite is true. We have compared monthly averaged model  $^{210}\text{Pb}$  concentrations for 1993 with a climatology based on a large amount of surface measurements, which have been done over many years at various sites around the world. These data are available from the Laboratoire de Glaciologie et Geophysique de l'Environnement [Preiss *et al.*, 1996]. We have calculated the correlation and the average difference between measurements and model output separately for stations in the tropics, north



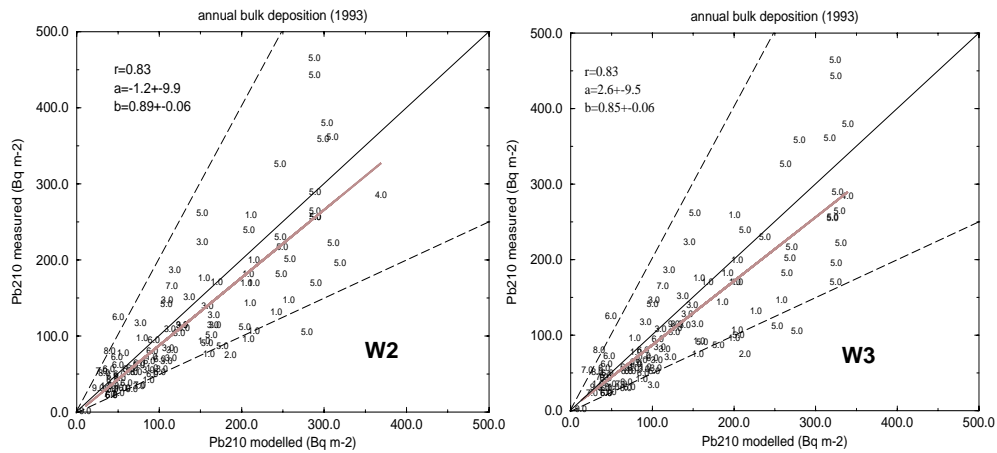


Figure 4.12: Comparison of annual bulk deposition of  $^{210}\text{Pb}$  between model results for the old scavenging scheme (left) and new scheme (right) and measurements for various sites: 1=North America, 2=South America, 3=Europe, 4=Africa 5=Indian subcontinent, 6=Oceania, 7=North Pacific, 8=South Pacific 9=Atlantic, 10=Arctic, 11=Antarctica. Also shown are linear regression statistics,  $r$ ,  $a$  and  $b$ , the correlation coefficient the  $y$ -offset and slope of the linear regression, respectively

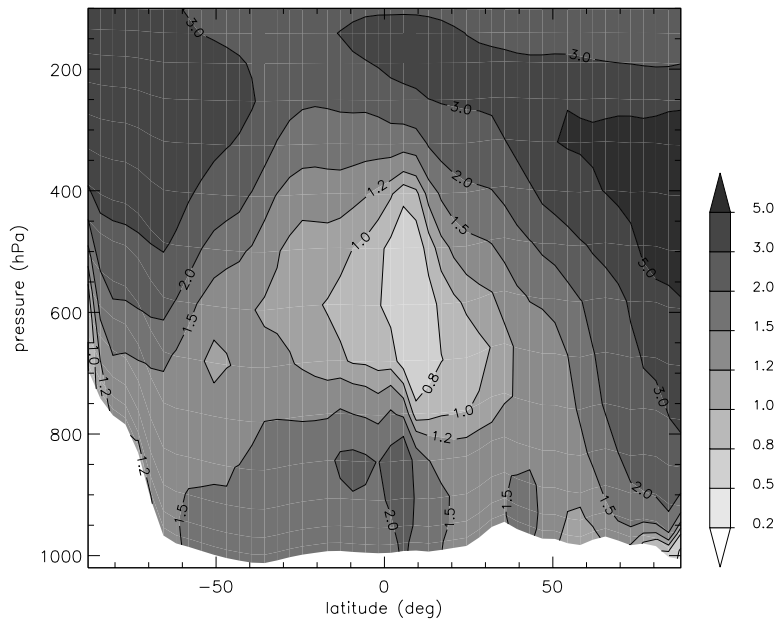


Figure 4.13: Zonally averaged  $^{210}\text{Pb}$  concentration ratio  $W2/W3$  for July 1993.

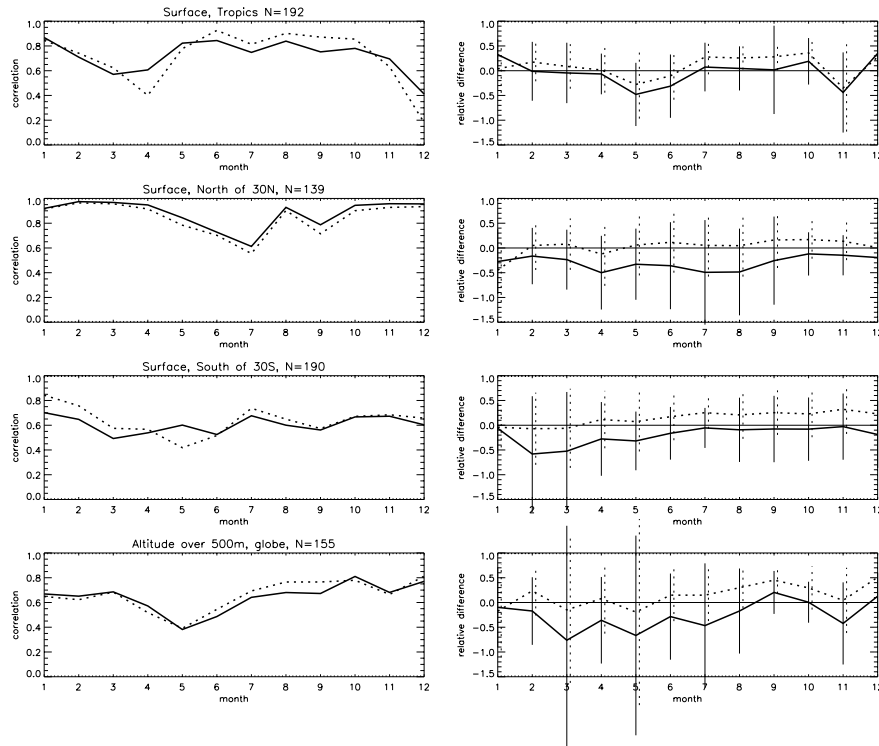


Figure 4.14: Correlation and average relative difference  $((obs-mod)/obs)$  between a climatology of monthly mean  $^{210}Pb$  measurements [Preiss et al., 1996] and monthly mean simulated surface layer concentrations for 1993. The simulation with the old scheme (**W2**) is represented by the solid and the simulation with the new scheme (**W3**) by the dotted line. Correlations and differences have been calculated for different domains, the standard deviation of the average difference and the yearly sample size are also showed.

of  $30^{\circ}N$ , south of  $30^{\circ}S$  and stations at altitudes over 500 meter. High correlations between model and measurements are obtained for both model simulations, especially for the northern hemisphere extra-tropics. The average difference is well within 50% for most months and domains. Except in the tropics, the simulation with the new scavenging scheme agrees clearly better with the observations with an average difference close to zero. In addition, the standard deviation of the differences is much smaller for model simulation **W3** than for **W2**, which indicates that in less cases large discrepancies between model and measurements occur.

The comparison of monthly mean modeled and measured surface concentrations for the specific year 1993 (figure 4.15) also shows an improvement compared to the old scheme. The model simulation with the new scavenging scheme in general tends to underestimate the observed  $^{210}Pb$  concentrations, especially in winter at higher latitudes. This could indicate that aerosol scavenging by ice or snow is too efficient. One should, however, realize that these results reflect the net effect of transport and removal. A different vertical diffusion scheme would result in a different vertical distribution of  $^{210}Pb$  and thus influence the scavenging. As we saw in section 4.2

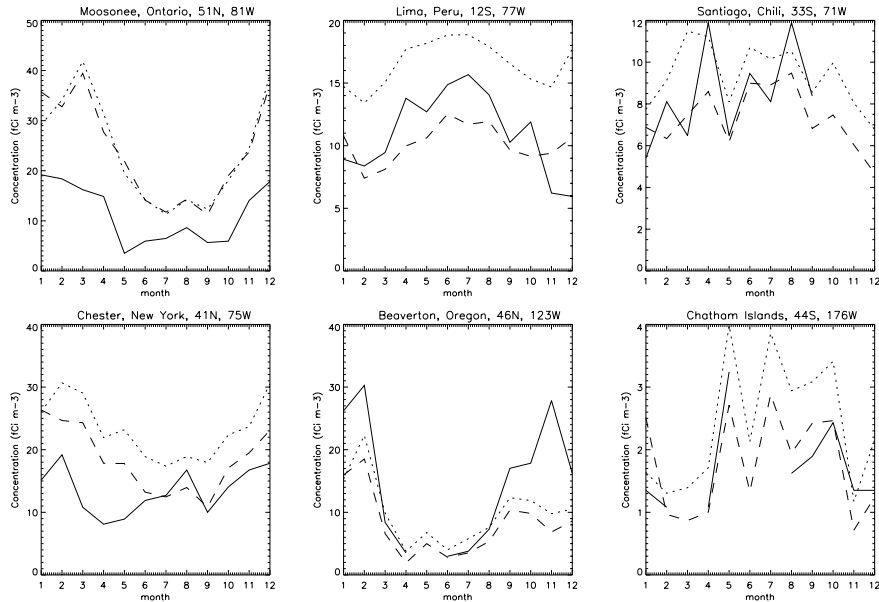


Figure 4.15: Monthly mean measured  $^{210}\text{Pb}$  surface concentrations (solid line) compared with model results for 1993. The dotted line is the simulation with the old and the dashed line the simulation with the new scavenging scheme.

the vertical diffusion in the model seems to be underestimated in winter. Increasing the vertical diffusion would further decrease  $^{210}\text{Pb}$  boundary layer concentrations and make discrepancies in winter even worse. Surface concentrations in particular are influenced by dry deposition. It is also possible that we overestimate the dry deposition of  $^{210}\text{Pb}$  in winter.

Based on Figure 4.13 the most pronounced effect of the new scavenging scheme is expected on the vertical distribution of  $^{210}\text{Pb}$ . For validation of model profiles we used some of the rare available profile measurements of  $^{210}\text{Pb}$ , which were carried out during the NASA Pacific Exploratory Missions PEM-West A [Dibb *et al.*, 1996] and PEM-West B [Dibb *et al.*, 1997] in September/October 1991 and February/March 1994 respectively. Model calculated  $^{210}\text{Pb}$  concentrations were interpolated to the time and location of the aircraft measurements. We have averaged both model and observational data over three larger areas: the western Pacific north of  $25^\circ\text{N}$ , the western Pacific south of  $25^\circ\text{N}$  and the central Pacific area around Hawaii. Most flights took place over the western Pacific. Figures 4.16 and 4.17 show that both model simulations capture the shape of the observed profiles quite well, especially for region NW during the PEM-West A campaign. For both campaigns the average difference between model and measurements is smallest for simulation **W3**. The correlation with measurements for **W3** is highest during the PEM-West A campaign while for the PEM-West B campaign **W2** has a higher correlation. In the lower troposphere simulation **W3** seems to underestimate the observed concentrations. Simulation **W2** strongly overestimates the upper tropospheric concentrations. The small sample size, the specific location of the measurements and the restricted time period, make it

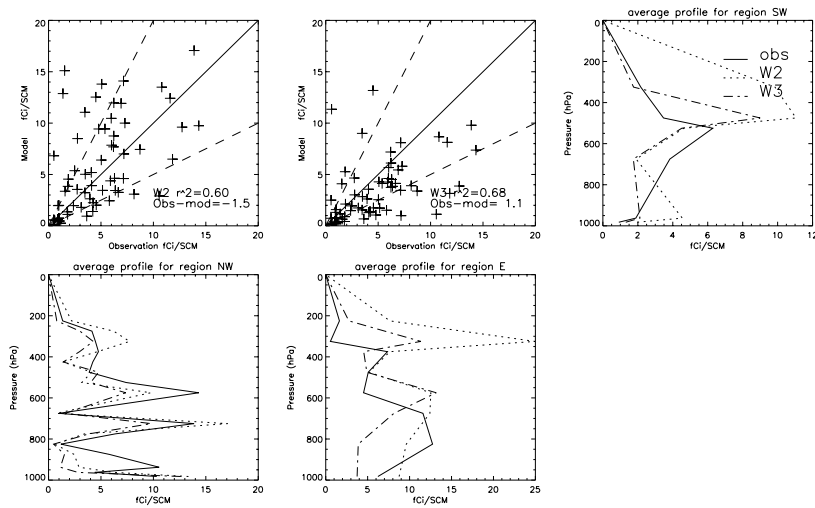


Figure 4.16: Measured  $^{210}\text{Pb}$  concentrations along the flight track (solid line) compared with model results for the PEM-West A campaign. **W2** is the simulation with the old and **W3** the simulation with the new scavenging scheme. Area SW ( $N=10$ ) represents all measurements between,  $10^\circ\text{S}$ - $25^\circ\text{N}$  and  $110^\circ\text{E}$ - $160^\circ\text{E}$ , NW ( $N=41$ ) between  $25^\circ\text{N}$ - $45^\circ\text{N}$  and  $120^\circ\text{E}$ - $160^\circ\text{E}$  and E ( $N=11$ ) between  $0^\circ\text{N}$ - $45^\circ\text{N}$  and  $180^\circ\text{W}$ - $140^\circ\text{W}$ .

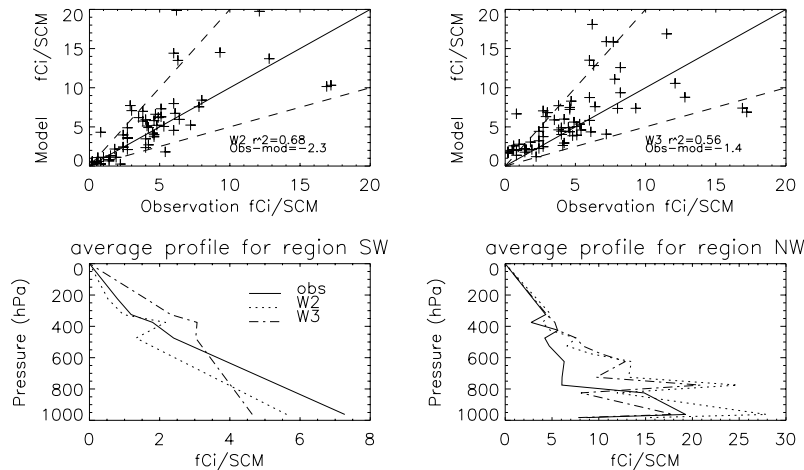


Figure 4.17: Same as Figure 4.16 but for the PEM-West B campaign. The number of aircraft samples  $N$  is 19 for region SW and 49 for region NW.

difficult to draw general conclusions.

## 4.4 Conclusions and Outlook

We have included an improved boundary layer diffusion scheme in the TM3 model. Its main features are: a more realistic description of the mixing under unstable conditions, increased mixing under stable conditions due to the use of revised stability functions, decreased mixing in the free troposphere due to the use of a smaller turbulent length scale and a better time resolution of 3 hour intervals instead of 6 hours. The most important improvement appears to be the increased time resolution, which resulting in a better resolved daily cycle. Also the magnitude of the vertical diffusion seems to have improved. For continental sites the surface concentrations have decreased, which improves the agreement with observations. In the upper troposphere there is a strong reduction of the concentrations due to the use of a smaller turbulent length scale. Statistically a small improvement is achieved with the new diffusion parameterisation in comparison with a few measured vertical profiles of Radon.

However, in almost all model-measurement comparisons, surface concentrations are overestimated, indicating that we still underestimate the vertical mixing. Several reasons can be identified. It might be that the limited resolution of the ECMWF input for the preprocessing, which has been interpolated from the original model resolution, results in too stable temperature profiles as was shown in Figure 4.1. This would again lead to smaller diffusion coefficients and the calculation of a too low boundary layer height. In the near future experiments will be done with  $1^\circ$  by  $1^\circ$  input data, which we expect will lead to an increased intensity of mixing. From these results resolution dependent stability correction functions might be derived.

Also the original ECMWF profiles of wind and temperature might already have lead to too high stability under some circumstances. E.g. there are indications from field campaigns in boreal forests that the energy balance over snow covered forests is incorrectly modeled leading to too stable boundary layers [Van der Hurk *et al.*, 1999].

Not only vertical diffusion determines the vertical transport of tracers in the model. In some cases the convection in the model can be too weak. In addition in some places too high Radon emissions could also lead to an overestimation of boundary layer concentrations.

In contrast to previous model versions, formation of large-scale precipitation is now calculated on-line in TM3 from ECMWF cloud fields. The in-cloud scavenging of tracers, which is the most efficient wet removal mechanism, is directly coupled to these precipitation formation rates. Scavenging in convective clouds is treated separately [Balkanski *et al.*, 1993] and allows for efficient wet removal of tracers over multiple layers in a single timestep in the updraft only. The annual and monthly bulk amounts of  $^{210}\text{Pb}$  removed by deposition appear to be rather insensitive to the vertical distribution of precipitation. Apparently the location and total amount of precipitation are of greater importance. Good improvement in simulated  $^{210}\text{Pb}$  concentrations is achieved compared to a simulation with an old scheme. In wintertime the observed surface concentrations seem to be underestimated at higher latitudes. This could indicate that the scavenging is too efficient in these areas and that a generalisation for cloud water and ice scavenging, rain and snow can not be fully justified. The  $^{210}\text{Pb}$  profiles measured from aircrafts are well simulated by the model. These profiles were,

---

however, measured for a specific season and area over the Pacific ocean. To draw more general conclusions, profile measurements for other seasons and for continental locations would be needed. Unfortunately, to our knowledge such measurements do not exist.  $^{210}\text{Pb}$  is relatively well mixed. For less well mixed components the vertical distribution of precipitation might become more important. For tracers that react in the cloud phase it is desirable that clouds and scavenging are modeled consistently. This probably provides the best argument to use the new proposed scavenging scheme in TM3.



## Chapter 5

# Modeling the global sulfur cycle with a global chemistry transport model and comparison with measurements

*The work presented in this chapter has been done in close cooperation with Frank Dentener, Swen Metzger, who developed the aerosol equilibrium module, and Pepijn Veefkind, who developed and validated the ATSR-2 and GOME AOD retrieval algorithms. AOD satellite data of ATSR-2 for August 1997 were kindly provided by Cristina Robles-Gonzales and Gerrit de Leeuw (TNO-FEL). Surface measurements of aerosol composition at Petten were kindly provided by Harry ten Brink (ECN) and data of the Dutch national air pollution monitoring network by Hans Bergwerff (RIVM). All work has been done within the framework of the MEMORA project of the Dutch national research program for air pollution (NRP).*

### 5.1 Introduction

An increasing number of global CTMs and GCMs are nowadays able to simulate sources and sinks of aerosol <sup>1</sup>. Langner and Rodhe [1991] were among the first to perform a global simulation of sulfate aerosols. Many more modelers followed [e.g. Pham et al., 1995; Feichter et al., 1996; Chin et al., 1996; Roelofs et al., 1998]. Also for other aerosol species like organic aerosols [Lioussse et al., 1996], black carbon [Cooke and Wilson, 1996], dust aerosols [Tegen and Fung, 1994], sea salt aerosol [Gong et al., 1997] and nitrate aerosols [Metzger et al., 1999b; Adams et al., 1999], three-dimensional model studies have become available. For sulfate aerosols, the confidence in model results is largest. Model results for other aerosol components

---

<sup>1</sup>“aerosol” is system of aerosol particles, often abbreviated to aerosols



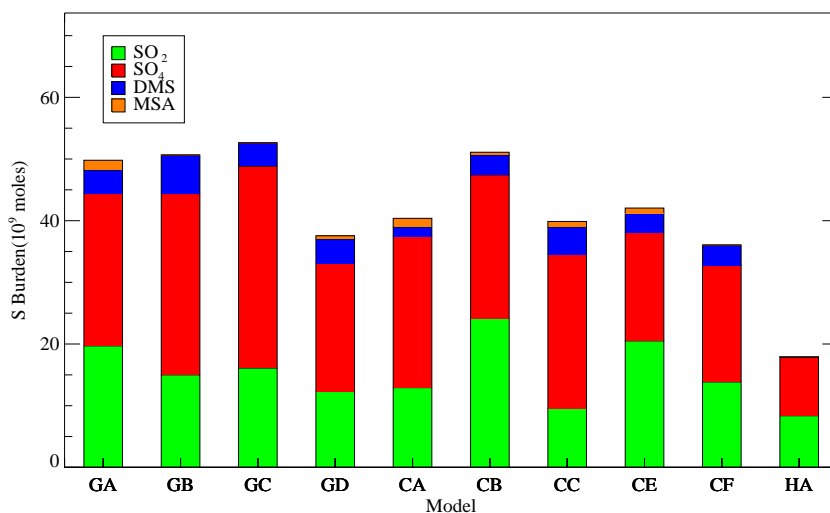


Figure 5.1: Annual averaged column sulfur burden for the models participating in COSAM. CB corresponds to a previous version of the model used in this study. (DMS=dimethyl sulfide; MSA=methanesulfonic acid;  $10^9$  moles corresponds to  $32 \times 10^{-3}$  Tg S)

indicate large uncertainties, a large part of which can be attributed to the lack of measurements available for validation. However, also the modeling of the sulfur cycle has its uncertainties.

Sulfate aerosols vary strongly both spatially and temporarily. The main reasons for this variation are the irregularly spaced sources of the sulfate precursor SO<sub>2</sub> and the strong dependence of SO<sub>2</sub> oxidation and aerosol scavenging on cloud and precipitation processes. The concentration distribution of SO<sub>2</sub>, in addition, strongly depends on dry deposition at the surface, since the deposition velocities vary considerably depending on surface characteristics and local meteorology. As a result the lifetime of SO<sub>2</sub> and sulfate is short ( $\pm 1-10$  days). The large variability of the sulfur species poses high requirements on the model. Due to a limited resolution and due to rather crude parameterizations of the before mentioned processes current models have difficulties to simulate the observed variability of sulfate correctly.

From the COSAM (COmparison of large scale atmospheric Sulfate Aerosol Models) workshop [Barrie *et al.*, 2000; Lohmann *et al.*, 1999; Roelofs *et al.*, 2000], in which about 10 global models participated, it was concluded that the variety in results for sulfur components among the different models is large. Most of the differences originated from the treatment of cloud and precipitation processes. Model results for sulfate were on average within 20% of the observed concentrations at remote sites while SO<sub>2</sub> was overestimated as much as a factor 2. Figure 5.1 shows the global and annual average column burden of sulfur containing species of the different models participating in COSAM. When we do not consider the hemispheric model HA, the simulated SO<sub>2</sub> burden ranges from 10 to  $25 \times 10^9$  moles and simulated sulfate burden

from 18 to  $32 \times 10^9$  moles.

A systematic error that appears in most models is the overestimation of  $\text{SO}_2$  surface concentrations in winter times. The TM3 model without any adaptation to the vertical diffusion showed this behaviour extremely. It was suggested [Kasibhatla *et al.*, 1997] that an additional heterogeneous oxidation mechanism, not yet included in models, might reduce  $\text{SO}_2$  concentrations. Furthermore, the dry deposition in wintertime could be underestimated.

In addition Roelofs *et al.* [1998] note that free tropospheric model concentrations differ considerably between models. This was confirmed by the results of the COSAM intercomparison workshop [Lohmann *et al.*, 1999]. However, the real vertical distribution is not well known due to a lack of profile measurements, which are only retrieved during dedicated airborne measurement campaigns.

Reported results from model-measurement intercomparison for sulfur species thus indicate that the processes controlling the sulfate aerosol cycle are not fully understood or at least not sufficiently accurately modeled yet. In this chapter the TM3 model as originally described by Houweling *et al.* [1998] is extended with the chemical cycles of sulfur and reduced nitrogen species.

Recent measurements [Ten Brink *et al.*, 1996a] indicate that nitrate may constitute an important mass fraction of the aerosol, and that therefore simulations of the sulfur cycle alone may not always be sufficient to obtain the aerosol optical properties such as the radiative forcing. However, the aerosol optical properties also strongly depend on the hygroscopicity (=aerosol associated water), which in turn depends of the composition of the aerosol. The latter is difficult to model in a global model, since species such as nitrate, are volatile and easily partition between gas and aerosol phase. Furthermore, the gas-aerosol partitioning strongly depends on the ambient relative humidity and temperature in addition to the aerosol precursor gases ( $\text{HNO}_3$ ,  $\text{NH}_3$ ) and pre-existing aerosol particles. Therefore, we have accounted for the gas-aerosol partitioning of the ammonia-sulfate-nitrate system, by adding a simplified thermodynamical equilibrium model [Metzger, 2000].

The changes to the model as described in Chapter 4 are also included in this aerosol version of TM3. The better description of the boundary layer turbulent diffusion should also improve the transport of  $\text{SO}_2$  surface emissions to the free troposphere. The improved wet scavenging scheme will have a strong impact on simulated aerosol concentrations. It is investigated to what extent the TM3 model with its additional improvements is able to reproduce the large observed variability.

To test the model, we compare its results with various measurements in section 5.3. First we will focus on the global scale and compare the TM3 model results with monthly averaged measurements at the background sites used in the COSAM model intercomparison [Barrie *et al.*, 2000]. To assess the model's ability to represent free tropospheric sulfate, we will consider profiles measured during a few aircraft measurement campaigns. Finally we look more specifically at model results for Europe. Day to day variations and daily cycles are compared to ground based measurements. In addition in section 5.4 model results for Europe will be looked upon from quite a different perspective by comparing model calculated aerosol optical depths derived from aerosol sulfate, nitrate and water with satellite retrieved optical depths from ATSR-2 and GOME.

	Reaction	Rate Coefficients ( $\text{cm}^3 \text{ molecules}^{-1} \text{ s}^{-1}$ )
1	$DMS + OH \rightarrow SO_2 + \dots$	$9.6 \times 10^{-12} \exp(-234/T)$
2	$DMS + OH \rightarrow 0.75SO_2 + 0.25MSA$	$k_1 M / (1. + k_2 M)$ $k_1 = 1.7 \times 10^{-42} \exp(7810./T)$ $k_2 = 5.5 \times 10^{-31} \exp(7460./T)$ $M : O_2 \text{ (molecules/cm}^3\text{)}$
3	$DMS + NO_3 \rightarrow SO_2 + \dots$	$1.9 \times 10^{-13} \exp(500/T)$
4	$SO_2 + OH \rightarrow \dots \rightarrow H_2SO_4$	$k_3 / (1. + k_3/k_4) 0.6^B$ $B = (1. / (1. + {}^{10} \log(k_3/k_4)^2))$ $k_3 = 3.0 \times 10^{-31} \times (T/300.)^{-3.3} \times M$ $k_4 = 1.5 \times 10^{-12} \times (T/300.)$ $M : \text{air density (molecules/cm}^3\text{)}$
5	$NH_3 + OH \rightarrow NH_2 + H_2O$	$1.7 \times 10^{-12} \exp(-710/T)$

Table 5.1: Gasphase reactions and rate coefficients as used in TM3

## 5.2 Model description

### 5.2.1 Chemistry

The sulfur cycle is coupled to the chemistry version of TM3 as described by [Houweling *et al.*, 1998]. This chemistry model describes the background tropospheric  $\text{CH}_4$ - $\text{CO}$ - $\text{O}_3$ - $\text{HO}_x$ - $\text{NO}_x$  chemistry and the chemistry of Non Methane Hydro Carbons (NMHC's) lumped in groups, using a modified version of the widely used Carbon Bond mechanism [Gery *et al.*, 1989]. In the current TM3 version we use the photolysis scheme adapted from Krol and van Weele [1997] consistently with local cloud cover and ozone columns.

We have added the gas and cloud phase reactions of  $\text{SO}_2$ , DMS,  $\text{NH}_3$ ,  $\text{SO}_4^-$  and  $\text{NH}_4^+$ . Table 5.2.1 summarizes the gas phase reactions of  $\text{SO}_2$ , DMS and  $\text{NH}_3$  [Denstener and Crutzen, 1994]. For a complete list of all other gas phase reactions we refer to Houweling *et al.* [1998].

$\text{SO}_2$  is oxidized in the gas phase by the OH radical, ultimately producing sulfate. The reaction of DMS with OH has several pathways, which are not completely understood yet. Besides  $\text{SO}_2$ , Methyl Sulphonic Acid (MSA) is a major product of this reaction. As indicated in Table 5.2.1 two major steps can be identified, one leading to  $\text{SO}_2$  only and one leading to 75 %  $\text{SO}_2$  and 25 % MSA.

Table 5.2 summarizes the aqueous phase reaction of the sulfur species in TM3.  $\text{SO}_2$  and its oxidants  $\text{H}_2\text{O}_2$  and  $\text{O}_3$  are dissolved into the cloud droplet according to their respective Henry's Law equilibrium. For  $\text{SO}_2$  an effective Henry's law constant is used, taking into account dissociation into  $\text{HSO}_3^-$  and  $\text{SO}_3^{2-}$ , effectively allowing more  $\text{SO}_2$  to dissolve. Dissolved  $\text{SO}_2$  and its dissociation products can be denoted as  $S(IV)$  i.e. total sulfur in oxidation state 4 and consists of  $[\text{SO}_2 \cdot \text{H}_2\text{O}]$ ,  $[\text{HSO}_3^-]$  and  $[\text{SO}_3^{2-}]$  [Seinfeld, 1986]. Both the dissociation equilibrium and rate coefficients are pH dependent. Ignoring the contribution of weak acids and bases the pH ( $-\log[\text{H}^+]$ ) is calculated from the strong acids and bases as:

$$[\text{H}^+] = 2[\text{SO}_4]_a + [\text{MSA}]_a - [\text{NH}_4]_a + [\text{HNO}_3]_g + [\text{NO}_3]_a \quad (5.1)$$

, where subscripts a and g stand for dissolved aerosol and gaseous species respectively.

	Reaction	Rate Coefficients (cm <sup>3</sup> molecules <sup>-1</sup> s <sup>-1</sup> )
1	$SO_2 + H_2O_2 \rightarrow H_2SO_4$	$(8.10^4 \exp(-3560(1/T - 1/298)))/(0.1 + H^+)$
2	$S(IV) + O_3 \rightarrow H_2SO_4$	a) $4.39.10^{11} \exp(-4131/T) + 2.56.10^3 \exp(-966/T)$ b) $2.56 \exp(-966/T)/H^+$
3	$NH_3 + H_2SO_4 \rightarrow (NH_4)_2SO_4$	only limited by $NH_3$ availability

Table 5.2: Aqueous phase reactions and rate coefficients as used in TM3

For  $pH > 4.3$  also the dissociation of the weak acids  $SO_2$  and  $CO_2$  as well as the base  $NH_3$  is taken into account. With the concentration  $H^+$  known, the effective Henry's law coefficient (mol l<sup>-1</sup> atm<sup>-1</sup>) for  $S(IV)$  can be calculated from:

$$H_{S(IV)}^{eff} = H_{SO_2} \left( 1 + \frac{K_{s1}}{[H^+]} + \frac{K_{s1}K_{s2}}{[H^+]^2} \right) \quad (5.2)$$

, with the dissociation equilibrium constant  $K_{s1}$  for  $[SO_2 \cdot H_2O] \rightleftharpoons [HSO_3^-]$  and  $K_{s2}$  for  $[HSO_3^-] \rightleftharpoons [SO_3^{2-}]$ . The reaction of  $S(IV)$  with ozone can be written as 2 independent (a and b in Table 5.2) reactions of which the rate of one (b) increases strongly with increasing pH. This pH dependency of the  $O_3$  reaction is stronger than that of the  $H_2O_2$  reaction. This means that with increasing pH the  $O_3$  reaction will become more important.

In many models the sulfur cycle is coupled with off-line calculated fields of OH,  $H_2O_2$  and  $O_3$  [Feichter et al., 1996; Langner and Rodhe, 1991]. In some models the  $H_2O_2$  concentration is allowed to gradually recover after reaction with  $SO_2$ . However, in reality the recovery of  $H_2O_2$  depends on the local chemistry regime. Lohmann et al. [1999] conclude that models that calculate the chemistry of the oxidants on-line are better able to simulate measured instantaneous profiles of  $SO_2$  and sulfate. Roelofs et al. [1998] also concludes that coupling between sulfur chemistry and photochemistry gives a somewhat better agreement with observations. However, the average overestimation of  $SO_2$  levels is less in models with prescribed oxidant fields [Koch et al., 1999].

Following Dentener and Crutzen [1993] we calculate heterogeneous reaction rates of  $N_2O_5$  on preexisting aerosol surface, resulting in the formation of  $HNO_3$  (g). Since the aerosol in our model is MSA and ammonium-sulfate/nitrate only, we might underestimate the rate of this reaction. Most other sulfur-cycle models do not model ammonia, but assume that a fixed fraction of sulfate is neutralized by ammonium. Ammonium, however, can have a strong and spatially variable feedback on sulfur cycle via the calculation of the pH and is therefore included in our model.

### 5.2.2 Aerosol equilibrium model

Aerosol properties like the aerosol composition and the aerosol associated water are difficult to measure in the atmosphere but are of importance for the calculation of the aerosol radiative forcing. Therefore, several thermodynamic gas-aerosol equilibrium models (EQMs) have been developed (for an overview see Metzger et al. [1999a]).

An EQM describes the equilibrium partitioning between aerosol precursor gases ( $NH_3$ ,  $H_2SO_4$ ,  $HNO_3$ , and  $HCl$ ) and liquid and solid aerosol phases for major inorganic aerosols compounds (ammonium, sulfate, nitrate, sea salt, mineral dust). Some

simplifications have to be made in general. For instance, it is usually assumed that aerosols are internally mixed, and that they obey thermodynamic gas-aerosol equilibria; both assumptions are safely made under prevailing atmospheric conditions, since most compounds form highly hygroscopic salts, and hence, take up so much water that they are deliquescent and internally mixed.

Nevertheless, the calculation of the gas-aerosol partitioning is rather complex. This has led to the development of complex EQMs, which are not suited for global modeling since they rely on iterative methods to calculate the activity coefficients of the aerosol components. Consequently, the aerosol composition and the water uptake have been rarely investigated on a global scale.

Several approaches have been proposed as an alternative to the iterative calculation of activity coefficients. These range from neural networks [*Potukuchi and Weiler, 1997*] to obtain the gas partial pressure of the equilibrium composition, to the use of pre-calculated sets of activity coefficients [*Nenes et al., 1998*] and polynomial fits to an activity coefficient - RH relationship [*Metzger et al., 1999a*].

Recent work [*Metzger, 2000*] has shown that it is in principle not necessary to use iterative schemes for the calculation of activity coefficients and equilibrium composition of binary or multi-component systems. Based on fundamental physical properties, a new method has been introduced which allows to calculate the gas-aerosol partitioning for global modeling rapidly and accurately.

The method is based on the fact that, for atmospheric aerosols in thermodynamical equilibrium with the ambient air, the solute activity, and hence the activity coefficient calculation, is governed by the aerosol associated water. The latter depends only on the relative humidity and the type and number of moles of dissolved matter. Central in the method is the use of concentration domains, which are based on the mole ratio of the solute concentrations. For instance the aerosol can be in the “sulfate rich” domain (i.e.  $2\text{NH}_4^+ < \text{SO}_4^{2-}$  or in the sulfate poor case (i.e.  $\text{NH}_4^+ > \text{SO}_4^{2-}$ ). Based on the domain and the relative humidity the aerosol associated water amount can be calculated and from this it is possible to directly derive the activity coefficients using a generalization of Raoult’s law.

The activity coefficients calculated non-iteratively with the new method, compare well with those obtained with common iterative methods of various EQMs, when applied to cases (concentration domains) where the aerosol droplet is non-acidic, e.g. that sulfate is completely neutralized (“sulfate-poor”, “sulfate-neutral” or “cation-rich”). For the remaining cases, which are mostly “sulfate-rich” or “very-rich” cases, however, discrepancies can occur, which increase as the relative humidity decreases. It has, however, been shown that practically this has no influence on the composition of atmospheric aerosols, including the aerosol associated water, since acidic particles are generally assumed to be non-volatile. Therefore, the gas-aerosol partitioning, can be calculated sufficiently accurately for all conditions relevant to large-scale atmospheric/chemistry modeling [*Metzger, 2000*]. Since the new method is an inexpensive and straightforward alternative to the explicit and more expensive thermodynamic calculations, it is suited for global aerosol chemistry transport models.

We have implemented the above-described method in TM3 to calculate the gas-aerosol partitioning of  $\text{NH}_3$ ,  $\text{NH}_4^+$ ,  $\text{HNO}_3$ ,  $\text{NO}_3^-$  and  $\text{SO}_4^{2-}$ . For this purpose nitrate ( $\text{NO}_3^-$ ), which was not included in previous model versions, has been added as a tracer to the model. Removal of ammonium nitrate by wet scavenging and by dry deposition is treated the same as for sulfate aerosol, thus implicitly assuming similar physical

properties as for sulfate.

### 5.2.3 Emissions

Anthropogenic emissions of  $\text{NO}_x$ ,  $\text{NH}_3$ ,  $\text{SO}_2$  have been taken from the historical Emission Database for Global Atmospheric Research (EDGAR) [Olivier, 1996] calculated on a grid of  $1^\circ$  by  $1^\circ$ . Van Aardenne *et al.* [1999] have estimated trends in these emissions, based upon demographical, economical, agricultural and technological developments during the past century. For example, the abatement strategies have caused the  $\text{SO}_2$  emissions to strongly decrease in western Europe and the United States, while economic growth has caused an increase in emissions of CO and  $\text{NO}_x$  and  $\text{SO}_2$  in other parts of the world. The time resolution of the database is 10 years until 1970 and 5 years hereafter up to 1990. After 1990 we have extrapolated the 1990 emission data, based on the increase of energy consumption. To obtain estimates for the specific years used in the model simulations in this Chapter, we linearly interpolate between the base years.

The seasonal variation in  $\text{NO}_x$  and  $\text{SO}_2$  is based upon the Global Emission Inventory Activity (GEIA) data base valid for 1985 [Benkovitz *et al.*, 1996]. In addition, the GEIA database distributes the emissions between two layers, below and above 100m height. We have converted the GEIA emissions into normalized weight factors. These seasonal and vertical weight factors have been applied to the EDGAR annual totals. Volcanic sulfur emissions are estimated by Andres and Kasgnoc [1998]. Distinction is being made between continuously and sporadically erupting volcanoes. DMS emissions are obtained by combining the oceanic surface concentrations compiled by Kettle *et al.* [1999] with turbulent air-sea exchange coefficient calculated using the parameterization by Liss and Merlivat [1986]. For DMS land-emissions and  $\text{SO}_2$  natural emissions we use the estimates of Spiro *et al.* [1992]. All other emissions are described in Houweling *et al.* [1998].

Within the framework of EMEP and the European project CORINAIR=(CORE INventory AIR), participating countries have committed themselves to regularly report their national emissions of several species on a grid of  $50 \times 50$  kilometer [EMEP, 1998]. In contrast with the global EDGAR data after 1990, reported CORINAIR emissions take into account the changes in emission factors, e.g. changes in the conversion factors from fossil fuel use by electric power generation to  $\text{SO}_2$  emissions. These conversion factors depend on several technical factors like which filter systems have been used or the composition of the fuel. Especially for  $\text{SO}_2$  these factors have changed considerably over the last 10 years. This is supported by the figures obtained from both data bases for 1997. While the total of  $\text{SO}_2$  emissions for Europe in the EDGAR database is 22 Tg S, it is only 12 Tg S in the CORINAIR data base. This remarkable difference leads to differences in model results depending on which emission data are taken. This will be discussed in section 5.3.3.

### 5.2.4 Dry deposition

Dry deposition is the major sink for soluble or reactive trace gases like  $\text{SO}_2$  and  $\text{NH}_3$ . Especially in wintertime when low  $\text{H}_2\text{O}_2$  concentrations limit  $\text{SO}_2$  oxidation it will be the dominant sink for  $\text{SO}_2$ . Therefore we use the “resistance in series” dry deposition scheme as described by Ganzeveld *et al.* [1998], which contains a fairly

detailed description of surface characteristics. The deposition velocity  $V_d$  can be written as the inverse of serial resistances:

$$V_d = \frac{1}{R_a + R_b + R_{surf}} \quad (5.3)$$

in which  $R_a$  is the aerodynamic resistance,  $R_b$  the quasi-laminar boundary layer resistance and  $R_{surf}$  the surface resistance. In the parameterization the surface resistance of  $\text{SO}_2$  strongly depends on snow cover and surface wetness. The sulfate aerosol deposition velocity is dependent on two parameterized size distribution, one for land and one for oceans, and further depends on the wind velocity which may increase the contact surface area over ocean when the sea becomes rough. Meteorological surface fields are obtained from the ECMWF archive. Vegetation descriptions are derived from a global ecosystem database [Olson *et al.*, 1983]. Variables like snow cover and surface wetness are prescribed by ECHAM4 climatological data [Claussen *et al.*, 1994]. According to Van der Hurk *et al.* [1999], in wooded areas the snow covered fraction is substantially smaller than one. We correct the ECHAM snow cover for this effect by allowing a maximum snow cover of 70% over vegetated surfaces.

The strong dependence of  $\text{SO}_2$  surface concentrations on dry deposition, makes it difficult to compare model results with surface measurements. Due to the variation in surface characteristics, also the surface concentrations will vary considerably within a grid cell. Under specific atmospheric conditions the vertical gradient of  $\text{SO}_2$  can be strong when there is stable stratification and a strong deposition at the surface. The concentrations at measurement height are therefore not necessarily representative for an average 60 meter layer concentration in the model. Therefore during winter and at night one might expect the model to overestimate the surface measurements.

### 5.2.5 Wet scavenging

In Chapter 4 the equations for precipitation scavenging of aerosols and completely soluble gases were presented. In TM3 we use  $\text{HNO}_3$  as the reference for a completely soluble gas. The scavenging rate  $\beta_x$  for any other gaseous species  $x$  is scaled to the scavenging rate of  $\text{HNO}_3$  according to its Henry equilibrium constant  $\mathcal{H}_x$  [Dentener and Crutzen, 1993]:

$$\beta_x = \beta_{\text{HNO}_3} \frac{R_g T L \mathcal{H}_x}{1 + R_g T L \mathcal{H}_x} \quad (5.4)$$

, where  $R_g$  is the universal gas constant,  $T$  the temperature and  $L$  the liquid water content ( $\text{m}^3 \text{m}^{-3}$ ). This scaling is applied to both in- and below-cloud scavenging.

The Henry coefficient of  $\text{SO}_2$  is with  $1.24 \text{ M atm}^{-1}$  at 298 K about  $2 \cdot 10^5$  times lower than for  $\text{HNO}_3$ . This means that most  $\text{SO}_2$  would reside in the gas phase and that it would hardly be scavenged by rain. We have seen (Equation 5.2) that due to dissociation of  $\text{SO}_2$  in the water droplet the effective Henry coefficient is much higher. This effective Henry coefficient is used in the cloud chemistry to describe the dissolution and reaction of  $\text{SO}_2$ . So the in-cloud scavenging of  $\text{SO}_2$  is already accounted for via the cloud chemistry. For below-cloud scavenging we assume that when the pH is below 5 the amount of  $\text{SO}_2$  scavenged is only limited by the amount of  $\text{H}_2\text{O}_2$  in the falling rain, assuming fast reaction of  $\text{H}_2\text{O}_2$  and  $S(IV)$ . Above pH=5

the below-cloud scavenging rate of  $\text{SO}_2$  is equal to the rate of  $\text{HNO}_3$ , assuming that oxidation by (the excess)  $\text{O}_3$  effectively removes  $S(IV)$ . By keeping track of the amount of  $\text{H}_2\text{O}_2$  and  $\text{H}^+$  scavenged in the grid cells above, the below cloud scavenging rate of  $\text{SO}_2$  is calculated. This simplified method probably presents an upper limit for the below cloud scavenging of  $\text{SO}_2$  since it assumes that the reactions and dissociation processes are fast compared to the time scales of existence of rain droplets.

### 5.2.6 Meteorological data

The calculation of the gas- and cloud phase chemistry in the model requires meteorological input fields. Most gas phase reaction rates are depending on temperature and pressure. Like the windfields, these are available every 6 hours from ECMWF analysis.

Since wet processes are of major importance for the chemistry of sulfate and nitrate aerosols, accurate cloud fields are crucial. The global mean cloud cover is close to 60%. The global average volume fraction of clouds in the troposphere is 7-8% and about 10% of the tropospheric air mass is contained in cloud systems. Together with the fact that chemical reactions in clouds are often much faster than in the gas phase, these numbers illustrate the importance of clouds for tropospheric chemistry [Lelieveld and Crutzen, 1991]. The distribution of clouds influences the chemistry in the model in three ways:

- First of all clouds provide an efficient reaction volume for aqueous phase reactions. The concentrations of dissolved species in the water droplets is dependent on the liquid water content. In this way also the acidity of the droplet is influenced.
- If cloud droplets grow beyond a certain size they will fall out as rain, returning particulate matter and dissolved gases to the earth's surface.
- Clouds also have a strong interaction with radiation, reflecting large parts of the shortwave radiation back to space, increasing the radiation intensity above the cloud and decreasing it below the cloud. Photo-dissociation of chemical species in this way strongly depends on the cloud distribution. We implemented the photolysis parameterization of [Krol and van Weele, 1997], which takes into account the effects of clouds.

We use 6 hourly three-dimensional fields of cloud cover and the cloud liquid and ice water content, available from the ECMWF re-analysis project (ERA). In the ECMWF model the cloud liquid water content and the cloud cover fraction are prognostic variables [Tiedtke, 1993] which have been calculated on a resolution of  $1.125^\circ$  by  $1.125^\circ$ . Not many off-line models contain this accurate cloud information. Often a climatological cloud distribution is prescribed [Pham *et al.*, 1995], [Langner and Rodhe, 1991] and sometimes part of the hydrological cycle is calculated on-line [Rasch *et al.*, 1997] or strongly parameterized [Benkovitz *et al.*, 1994; Kasibhatla *et al.*, 1997]. Climate models predict a climatological cloud distribution, but have the advantage of a better time resolution of the cloud fields. A higher resolution in time than 6 hours in our model can be important for the often very efficient chemical reactions in clouds. Since TM3 uses off-line calculated cloud fields, there is no feedback of calculated aerosol mass on cloud formation.



	Vertical diff.	Below-cloud scav.	Emissions	Resolution
<b>A1</b>	old	reduced	EDGAR	5° by 3.75° by 19
<b>A2</b>	new	reduced	EDGAR	5° by 3.75° by 19
<b>A3</b>	new	full	EDGAR	5° by 3.75° by 19
<b>A4</b>	new	full	EDGAR	2.5° by 2.5° by 31
<b>A5</b>	new	full	CORINAIR	2.5° by 2.5° by 31

Table 5.3: *Outline of the experiments performed with TM3. The “old” diffusion scheme is the scheme of Louis [Louis, 1979], previously used in TM3. The “new” scheme is the scheme as presented in Chapter 4. In two experiments the below-cloud scavenging, as described in 5.2.5 is reduced by 50%. In experiment A5 the EDGAR emission data for Europe are replaced by the CORINAIR emissions.*

## 5.3 Results

In this section results for  $\text{SO}_2$  and  $\text{SO}_4^{2-}$  and to a lesser extend  $\text{NH}_x (= \text{NH}_3 + \text{NH}_4^+)$  and nitrate are discussed. The TM3 model including both the updated scavenging and vertical diffusion scheme (see Chapter 4) is compared with surface, aircraft and satellite observations.

First we present global budgets of  $\text{SO}_2$  and sulfate and a comparison between model results and monthly averaged measurements to assess and demonstrate the sensitivity to specific parameterizations. Next profile measurements from aircraft campaigns are used to evaluate the vertical distribution of species in the model. Finally the model is evaluated for its ability to simulate the day-to-day variability and daily cycle of  $\text{SO}_4^{2-}$ ,  $\text{NO}_3$  and  $\text{SO}_2$ . For this purpose we focus on Europe for August 1997, and also use a better model resolution. Table 5.3 lists the 5 model simulations which we have done to investigate the influence of different resolutions, emissions and parameterizations of vertical diffusion and below-cloud scavenging in TM3. Results are discussed in the following sections.

### 5.3.1 Budgets and monthly averages

With model experiments **A1** to **A3** the influence of the new vertical diffusion scheme on the sulfur cycle is evaluated. In addition, the sensitivity of  $\text{SO}_2$  to below-cloud scavenging is tested by reducing it with a (arbitrary) factor two, since the parameterization of below-cloud scavenging (section 5.2.5) presents an upper limit of the possible amount of  $\text{SO}_2$  that can be scavenged below the cloud. No results of simulations with the old wet scavenging scheme are presented here, as it is obvious from  $^{210}\text{Pb}$  simulations (Chapter 4) that the new scheme has clear advantages, especially for simulations of aqueous phase chemistry. Table 5.4 shows the global budgets of model simulations **A1** to **A3**. The turnover times of  $\text{SO}_2$  and  $\text{SO}_4^{2-}$  are both relatively short, compared to other global sulfur models. In the COSAM intercomparison the turnover time was in the range 1.3-3.1 days for  $\text{SO}_2$  and 3.6-7.5 days for  $\text{SO}_4^{2-}$ . So, especially for sulfate TM3 is in the low end of the range (of 10 models). This short turnover time of sulfate is likely due to the effective wet scavenging, which as we noticed for  $^{210}\text{Pb}$  in Chapter 4 might somewhat overestimate the removal of accumulation mode aerosol. The low turnover time of  $\text{SO}_2$  can be explained by the effective below cloud scavenging, which

	<i>Global</i>		<i>N. Hemisphere</i>		<i>NH-PBL</i>	
	SO <sub>2</sub>	SO <sub>4</sub> <sup>2-</sup>	SO <sub>2</sub>	SO <sub>4</sub> <sup>2-</sup>	SO <sub>2</sub>	SO <sub>4</sub> <sup>2-</sup>
Emission	2660	61	2340	52	2217	52
Dry deposition (A1)	1250	125	1139	94	1139	94
(A2)	1200	121	1069	91	1069	91
(A3)	1150	112	1061	86	1061	86
Wet deposition (A1)	789	1120	559	846	413	478
(A2)	789	1170	558	893	417	521
(A3)	955	1040	665	810	506	477
SO <sub>2</sub> +OH (A1)	224	-	193	-	142	-
(A2)	231	-	199	-	150	-
(A3)	228	-	199	-	154	-
SO <sub>2</sub> +O <sub>3</sub> /H <sub>2</sub> O <sub>2</sub> (A1)	934	-	672	-	362	-
(A2)	979	-	709	-	400	-
(A3)	863	-	634	-	358	-
burden (A1)	15.4	12.3	14.0	9.2	7.7	4.0
(A2)	15.6	12.6	14.2	9.5	8.1	4.3
(A3)	15.1	11.6	13.9	8.9	8.0	4.2
turnover time (A1)	1.76	3.61	1.99	3.51	1.37	2.55
(A2)	1.78	3.56	2.04	3.52	1.45	2.56
(A3)	1.72	3.68	1.98	3.62	1.40	2.72

Table 5.4: Annual budget in  $10^9$  moles year<sup>-1</sup> for three different model simulations for the year 1993. The oxidation of DMS by OH and NO<sub>3</sub> serves as an additional source for SO<sub>2</sub> of about  $540 \times 10^9$  mole year<sup>-1</sup>.

is not implemented in a lot of models. Furthermore it should be noted that a large part of the sulfate and SO<sub>2</sub> burden is in the free troposphere.

The new vertical diffusion scheme results in an increase of upward mixing to the clouds where more SO<sub>2</sub> is converted to sulfate. Consequently the sulfate burden and wet deposition increase and the dry deposition of SO<sub>2</sub> decreases. Remarkably, the magnitude of all processes varies within 5-10% only. The in-cloud conversion to sulfate and the wet scavenging of sulfate are reduced by 10% when in addition the below-cloud scavenging of SO<sub>2</sub> is increased. Note that these are annual global and hemispheric budgets. Regionally and locally the differences can be much larger.

For COSAM surface based observations of sulfur species were compiled by the WMO/GAW (World Meteorological Organization/Global Atmosphere Watch) aerosol data center. In order to utilize consistent measurements, with similar collection and analysis techniques, data from the large-scale networks were preferred. The sites are chosen based upon their location on the periphery of source regions and in more remote areas downwind of source regions [Barrie *et al.*, 2000].

Figure 5.2 and 5.3 show monthly averages of SO<sub>2</sub> and sulfate measurements for a few selected sites from the COSAM selection, together with results of model simulations **A1** and **A3** for the year 1993. Most of these sites are at higher latitudes. For sulfate, winter concentrations are clearly underestimated by TM3 and SO<sub>2</sub> concentrations are highly overestimated. Including the new vertical diffusion parameterization yields a small improvement, except for Hawaii. Figures 5.4 and 5.5 confirm this.

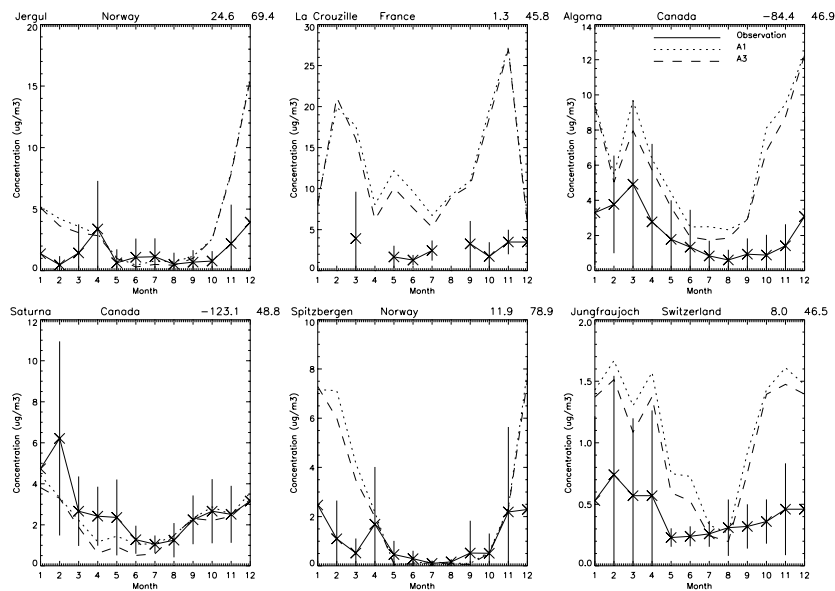


Figure 5.2: Monthly averaged concentrations for  $SO_2$  at selected stations with standard deviation of daily measurements (vertical bars) for 1993.

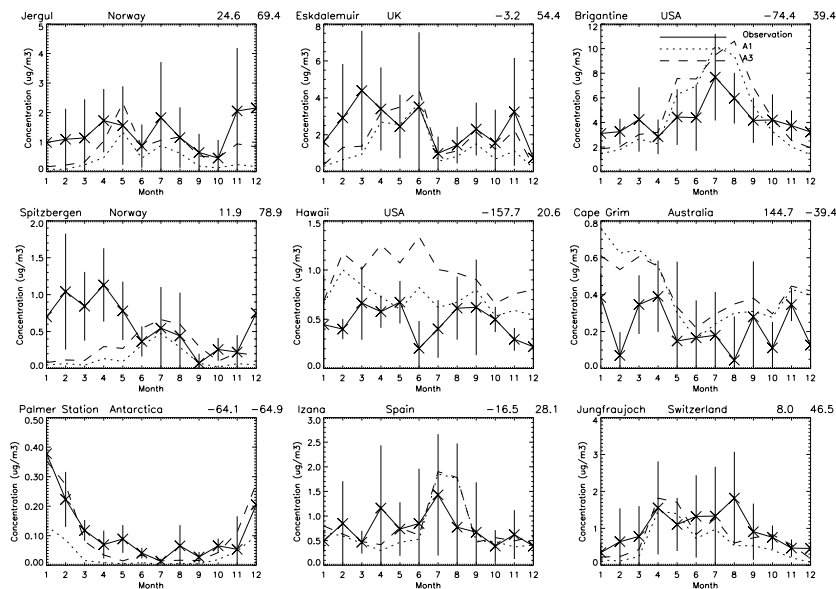


Figure 5.3: Monthly averaged concentrations for  $SO_4^{2-}$  at selected stations with standard deviation of daily measurements (vertical bars) for 1993.

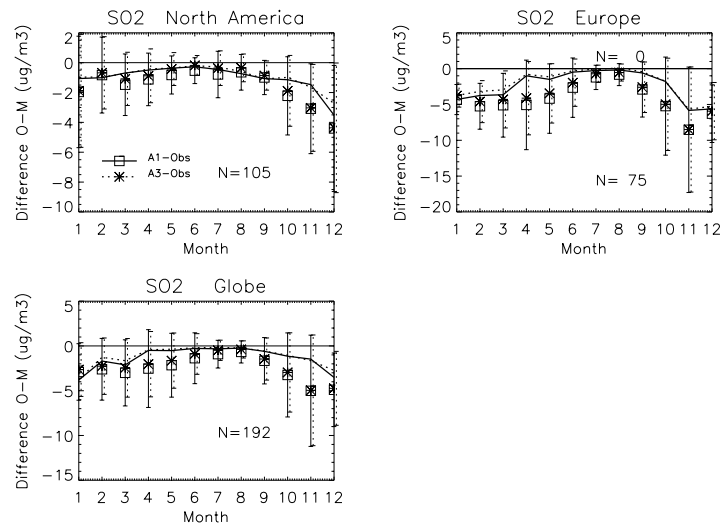


Figure 5.4: Mean (symbols), median (lines) and standard deviation (vertical lines) for the difference between observed and modeled  $\text{SO}_2$ . Definition of regions: North America ( $140\text{W}-35\text{W}, 25\text{N}-90\text{N}$ ), Europe ( $35\text{W}-80\text{E}, 30\text{N}-90\text{N}$ ), Oceania ( $80\text{E}-180\text{E}, 60\text{S}-0\text{S}$ ).

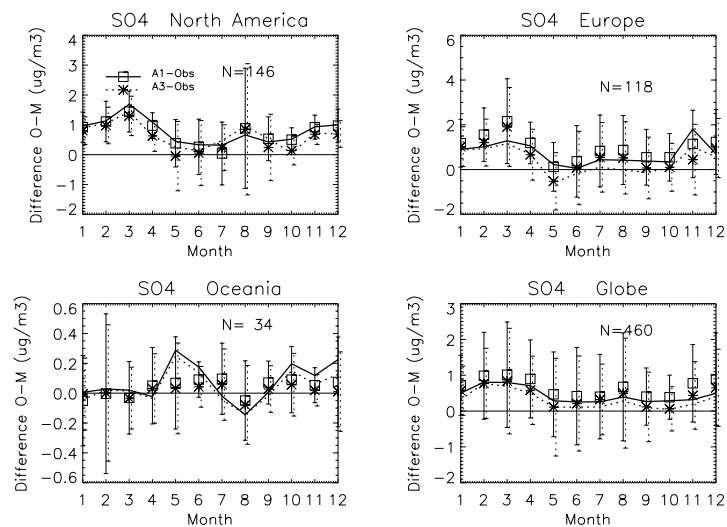


Figure 5.5: Mean (symbols), median (lines) and standard deviation (vertical lines) for the difference between observed and modeled sulfate. Definition of regions: North America ( $140\text{W}-35\text{W}, 25\text{N}-90\text{N}$ ), Europe ( $35\text{W}-80\text{E}, 30\text{N}-90\text{N}$ ), Oceania ( $80\text{E}-180\text{E}, 60\text{S}-0\text{S}$ ).

In these figures the average difference model - observation for all COSAM sites is presented. In addition sites have been subdivided per area. Especially for SO<sub>2</sub> the TM3 model strongly overestimates the measurements. As was also reported by other researchers, the bias is larger for Europe than for North America, e.g. [Koch *et al.*, 1999]. The substantial differences between the mean and median values in Figure 5.4 and 5.5, especially for SO<sub>2</sub> in winter, indicate that mean and standard deviation can for a large part be determined by a few extreme values. The underestimation of sulfate concentrations is similar for Europe and North America. Remarkably, the underestimation of sulfate concentration is relatively smaller than the overestimation of SO<sub>2</sub>. In section 5.5 we will discuss possible reasons for the observed discrepancies.

### 5.3.2 Profiles

In this section model simulations are compared with aircraft measurements. The simulations have been done for the same periods as the measurements were made. During two aircraft campaigns over Canada profiles of SO<sub>2</sub>, SO<sub>4</sub><sup>2-</sup>, aerosol particle number concentrations and H<sub>2</sub>O<sub>2</sub> were measured. The North Atlantic Regional Experiment (NARE) took place from August 9 to September 8, 1993. Profiles were measured over the peninsula of Nova Scotia around 44°N and 66°W [Leitch *et al.*, 1996; Fehsenfeld *et al.*, 1996]. SO<sub>4</sub><sup>2-</sup> was analyzed from the aerosol sampled on Teflon filters. The good correlation between aerosol particle number concentrations measured with a fast particle measuring system (PMS) and the integrated sulfate mass was used to derive high frequency sulfate values. SO<sub>2</sub> and H<sub>2</sub>O<sub>2</sub> were measured at 1 second intervals with an uncertainty of 30 and 5% respectively [Banic *et al.*, 1996]. The NARE area is far (±1000 km) removed from major SO<sub>2</sub> source areas. From the south-west polluted air masses can be advected originating from the urbanized east coast of the USA. About 80% of the sulfate and 55% of the SO<sub>2</sub> measured during NARE was transported above the boundary layer [Banic *et al.*, 1996].

The second Eulerian Model Evaluation Field Study (EMEFSII) was conducted from March 20 to April 29, 1990 near Egbert, Ontario (44°N, 80°W). Like for NARE, high frequency sulfate profiles were derived using the filter samples in combination with PMS data. SO<sub>2</sub> and H<sub>2</sub>O<sub>2</sub> measurements have an estimated uncertainty of 30 and 20% respectively [Lohmann *et al.*, 1999]. The EMEFSII area is located just north of the Toronto urban area. Only with southern winds polluted air is advected into the area. At the time of the EMEFSII measurements an Alaskan volcano had recently erupted causing elevated sulfur loadings in the upper troposphere.

The measurements of the NARE campaign (Figure 5.6) exhibit a lot of fine scale structure, with shallow layers of elevated concentrations at different heights and in general low surface concentrations. These shallow layers are probably plumes originating from long range transport from the USA and are not always captured by the model, resulting in a net underestimation of free tropospheric sulfate concentrations. Feichter and Lohmann [1999] obtained similar results with simulations with the ECHAM4 model.

Simulated H<sub>2</sub>O<sub>2</sub> concentrations are in the same range as those of the measurements. The spread in the model results from grid cell to grid cell is well illustrated by the SO<sub>2</sub> profile at August 20 and 24, where a shift of one grid cell makes a difference of 0.8 ppb in the concentration and the difference between good agreement and no agreement with the observations. For almost all profiles shown, the model values

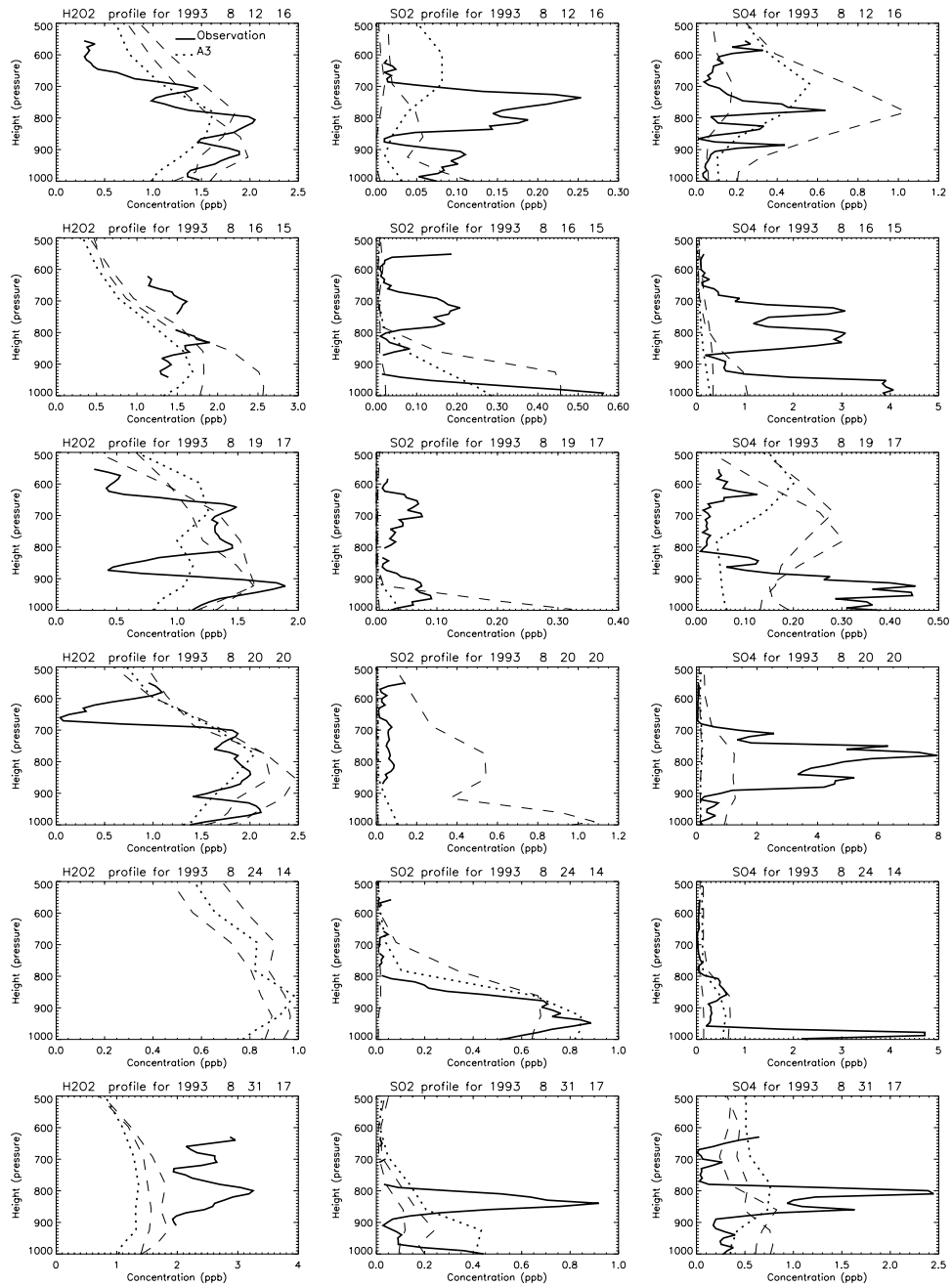


Figure 5.6: Selection of  $H_2O_2$ ,  $SO_2$  and  $SO_4$  profiles taken during the NARE intensive campaign [Leaitch et al., 1996]. The dotted line is the model value in the grid cell of the measurements and the dashed lines the model values of the two closest other grid cells.

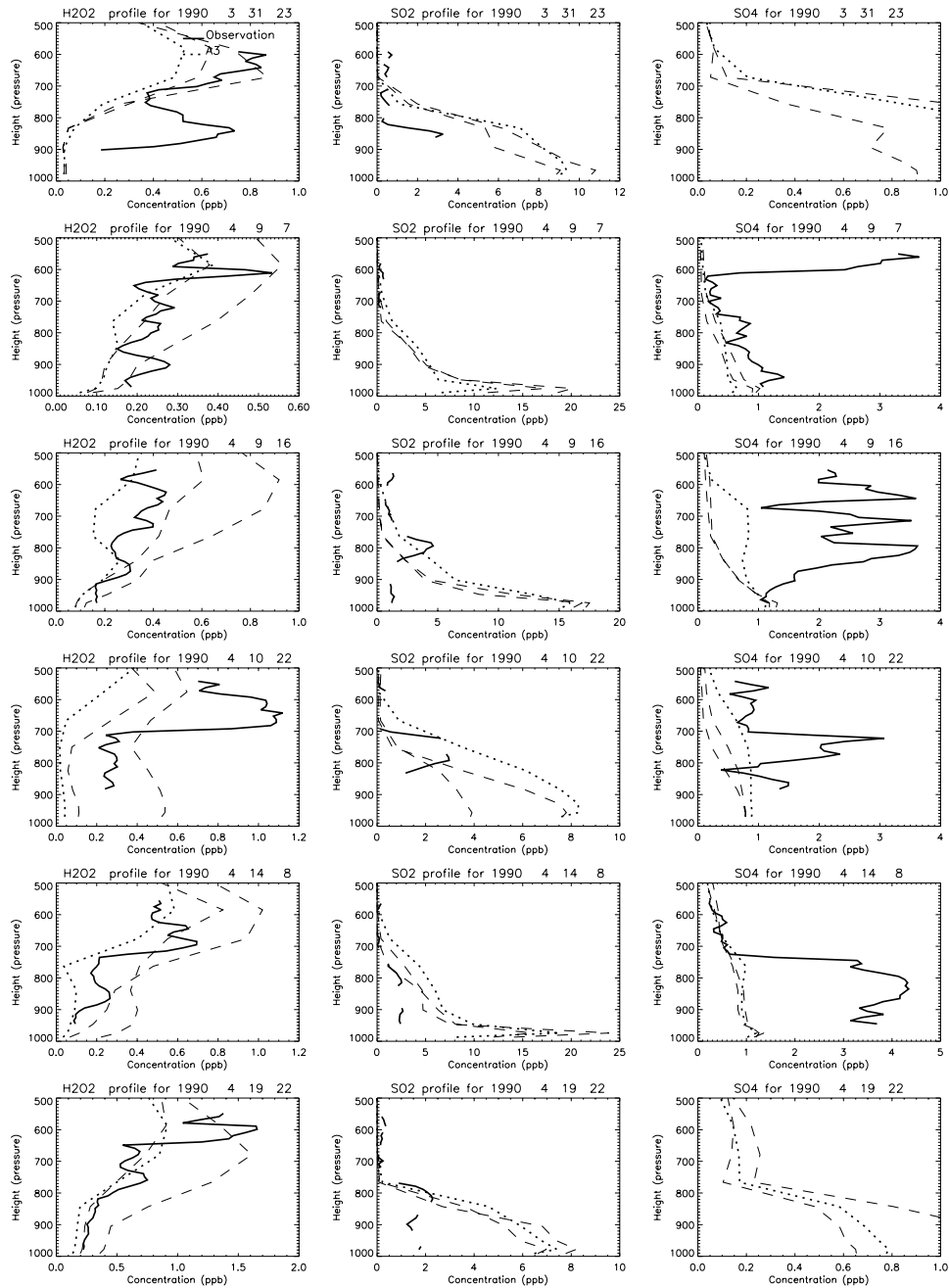


Figure 5.7: Selection of  $H_2O_2$ ,  $SO_2$  and  $SO_4$  profiles taken during the EMEFSII campaign [Issac, 1998] and TM3 profiles. The dotted line is the model value in the grid cell of the measurements and the dashed lines the model values of the two closest other grid cells.

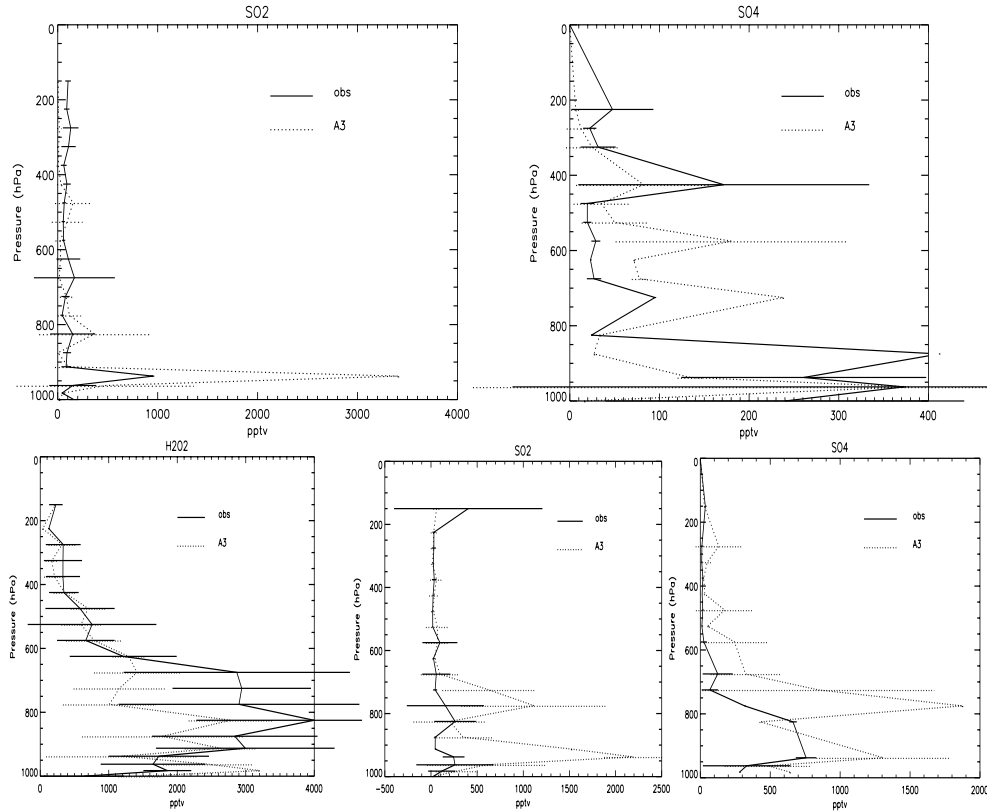


Figure 5.8: Average  $\text{SO}_2$  and  $\text{SO}_4$   $\text{H}_2\text{O}_2$  profiles for PEMW-A October 1991 (upper panels) and PEMW-B February 1994 (lower panels) +  $1\sigma$ . Observations are represented by the solid line and the model values by the dashed line. No error bar indicates that there is only one measurement at that level available.

of the closest grid cell, agree best with observations. For EMEFSII only few  $\text{SO}_4^{2-}$  profiles are available. As is the case for NARE, elevated sulfate plumes are not well captured by the model. If these plumes indeed originate from a volcanic eruption in Alaska, it is logical that the model does not represent them, since this eruption was not specifically accounted for in our model.  $\text{SO}_2$  concentrations in the boundary layer are generally overestimated by TM3, while there is a good agreement in the free troposphere. Also the  $\text{H}_2\text{O}_2$  concentrations are fairly well simulated and seem to be anti-correlated with  $\text{SO}_2$ . Near the surface, almost all  $\text{H}_2\text{O}_2$  in both model simulation and measurements is depleted, indicating that the oxidation of  $\text{SO}_2$  might be limited by the  $\text{H}_2\text{O}_2$  availability, assuming that sufficient clouds are present.

The Pacific Exploratory missions PEM West A and B took place over the northern and central West Pacific Ocean, in September/October 1991 and February/March 1994 respectively [Dibb *et al.*, 1996]. Aircraft measurements of aerosol composition and various trace gases were made to estimate the impact of anthropogenic emissions from China and Japan in this pristine oceanic region. Reported accuracies for the measurements are 10% for sulfate,  $\text{SO}_2$  and  $\text{H}_2\text{O}_2$  [Hoell *et al.*, 1997]. For PEM-



West A little outflow of polluted air from Asia was measured while for PEM-West B considerable amounts of pollution were transported over the ocean in a well-mixed boundary layer below 4 kilometer.

As sulfate is not continuously measured, we have averaged all available aircraft measurements over 20 vertical levels between the surface and 10 hPa. Model simulated values were interpolated to the time and location of the aircraft measurements and averaged in the same way. Figure 5.8 shows that for all components the agreement between model and measurements is good. The observed peak concentrations of sulfate are overestimated by the model, especially for the PEM-west B campaign. It should be noted, however, that at some levels there is only one observation available.  $\text{H}_2\text{O}_2$  seems to be underestimated by the model in the free troposphere. Due to the fact that measurements have been taken at various locations with different pollution characteristics, the scatter in the data is large. This variability in the measured profiles is also represented by the model.

It should be realized that these aircraft campaigns merely present a detailed snapshot for a certain period and area. Model simulated profiles have been compared to profiles from three distinctively different regions. For the coastal location of NARE the model seems to have difficulties to simulate the long-range transport of pollution plumes. For the continental location of EMEFSII boundary layer concentrations of  $\text{SO}_2$  are overestimated which, in this case, could be an indication of oxidant limitation. For both locations sulfate is underestimated. For the remote area of PEM-West A and B both sulfate and  $\text{SO}_2$  are overestimated by the model below 600 hPa. For the moment it is not clear what are the causes of these discrepancies as there are many model uncertainties (see section 5.5).

### 5.3.3 Simulation of aerosol components and $\text{SO}_2$ for Europe

In this section we will focus on the day-to-day variability and daily cycle of  $\text{SO}_2$  and the aerosol components represented by the model for Europe. For this purpose we use measurements from the EMEP network for August 1997 and measurements performed at the Dutch Energy Research Center at Petten ( $53^\circ\text{N}$ ,  $5^\circ\text{E}$ ) and at a few other measurement sites in the Netherlands. To be able to represent variability on time scales of a day or less, model simulations have been done at the, currently, highest possible resolution of TM3, which is  $2.5^\circ$  by  $2.5^\circ$  and 31 layers in the vertical. Model concentrations of  $\text{SO}_4^{2-}$ ,  $\text{NO}_3^-$ ,  $\text{NH}_4^+$ ,  $\text{NH}_3$ ,  $\text{SO}_2$  and  $\text{HNO}_3$  are sampled every two hours at the locations of the measurement sites. This includes 6 sites for the Netherlands and an additional 200 sites from the EMEP network. It must be noted that not all sites measured all species over the whole time period. Especially for  $\text{NH}_3$  and  $\text{NO}_3^-$  only a few measurements are available.

We also investigate the influence of emission reductions of  $\text{SO}_2$ . Therefore, in model experiment **A5**(Table 5.3) the EDGAR historical emission data for  $\text{SO}_2$  are replaced by the CORINAIR emission inventory for Europe. As we know from section 5.2.3, the CORINAIR emissions are on average almost a factor 2 lower than the EDGAR emissions since they are obtained by using more realistic emission factors. Figure 5.9 and 5.10 show the effect of the different emission data on the  $\text{SO}_2$  and sulfate surface concentrations. For  $\text{SO}_2$  the effect clearly is largest with the maximum differences between 100-200% over Germany and Eastern Europe. Differences for sulfate show a very similar pattern. Over most of Europe surface concentrations

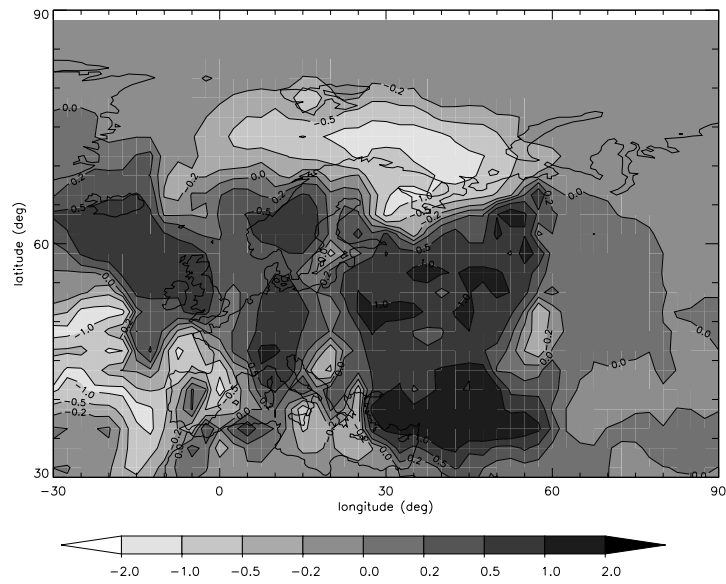


Figure 5.9: *Monthly average relative difference in surface  $SO_2$  concentrations for model simulation A4 - A5 over Europe for August 1997.*

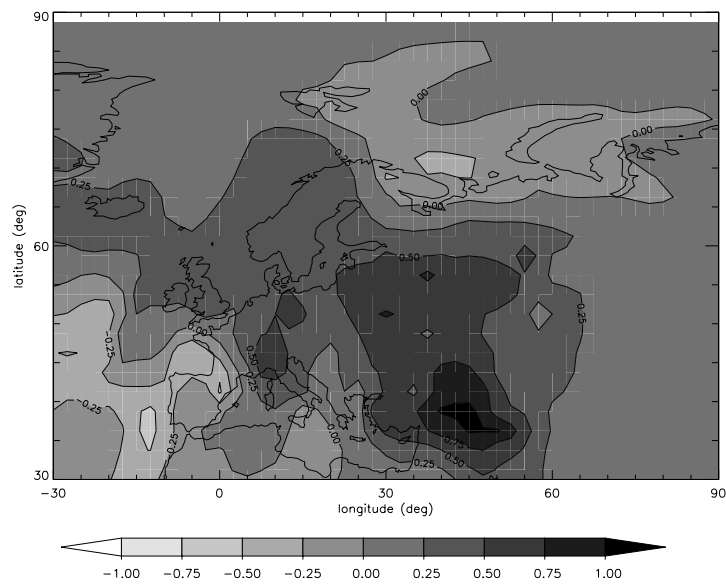


Figure 5.10: *Monthly average relative difference in surface sulfate concentrations for model simulation A4 - A5 over Europe for August 1997.*

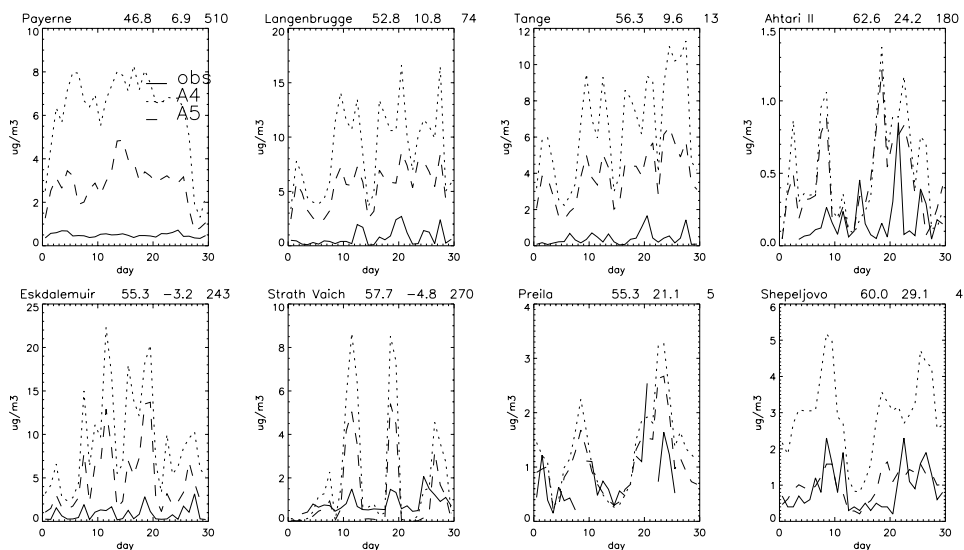


Figure 5.11: Comparison of daily averaged model values and measurements of  $\text{SO}_2$  for selected EMEP sites (August 1997). Numbers on top of the plots indicate latitude, longitude and height (m) respectively.

decrease when using the CORINAIR data. Only over the Spanish north and east coast, the Balkan and north Scandinavia we find an increase. This indicates that locally CORINAIR emissions might exceed the EDGAR ones.

Figure 5.11 shows a sample of 8 EMEP stations where  $\text{SO}_2$  has been measured. Sites were chosen such that they are representative for different European regions. In general, episodic peak values are reasonably well captured by both model simulations. However, the absolute values are in most cases much too high. At the eastern end of the European domain at Preila, Latvia and Shepeljovo, Russia we obtain good agreement between model simulation A5 and the measurements. Over the British islands at Strath Vaich Dam and Eskdalemuir the model strongly overestimates the observations but there is a good correlation between model and measurements. At Payerne, Langenbrugge and Tange, the observed concentrations are almost constantly very low, whereas the model simulations show rather high values. For station Ahtari II model and observations are in the same range but the agreement is not very good. In general, model concentrations agree better with observations for the model simulation with the CORINAIR emissions. We also get the impression (not only from these 8, but from all stations) that concentrations are most severely overestimated over the western European countries and that there is better agreement for eastern and northern European sites.

The average difference observation - model and the correlation between model and observation for all available EMEP measurements is shown in Table 5.5. Also these numbers clearly indicate that the agreement with observations becomes better when the CORINAIR emissions are used. On average simulation A5 overestimates the measurements with  $2.7$  and A4 with  $4.0 \mu\text{g m}^{-3}$  with a large variability between stations. Also the correlation between model and measurements improves considerably when

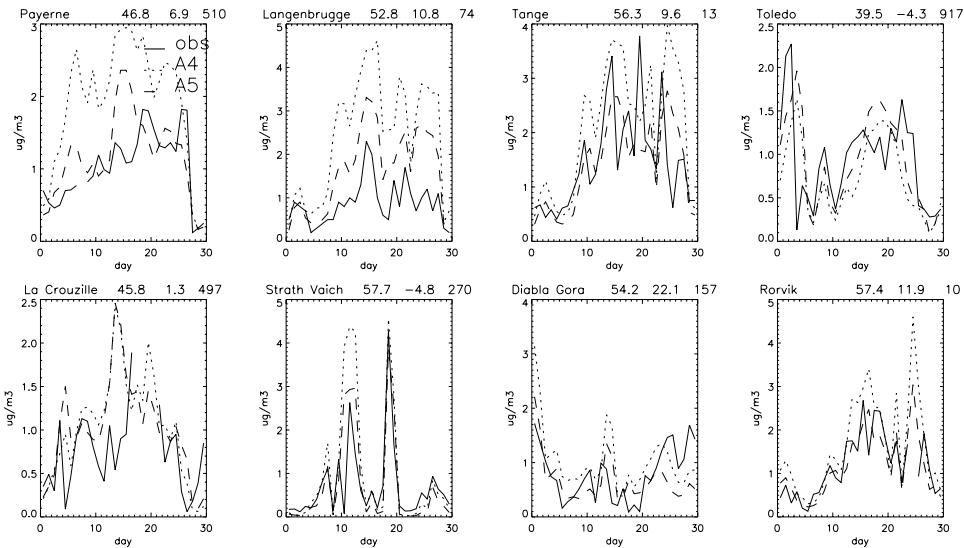


Figure 5.12: Comparison of daily averaged model values and measurements of  $SO_4^{2-}$  for selected EMEP sites (August 1997).

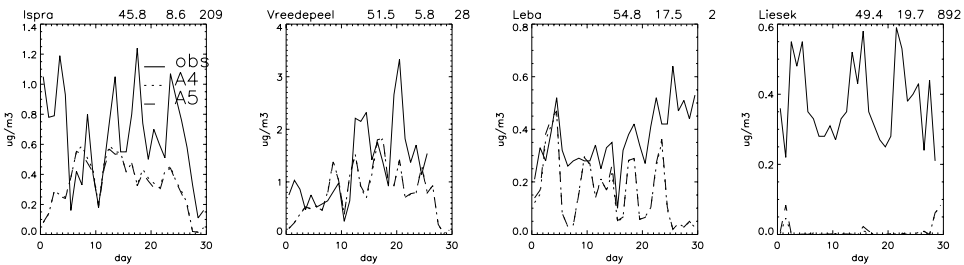


Figure 5.13: Comparison of daily averaged model values and measurements of  $NO_3^-$  for selected EMEP sites (August 1997).

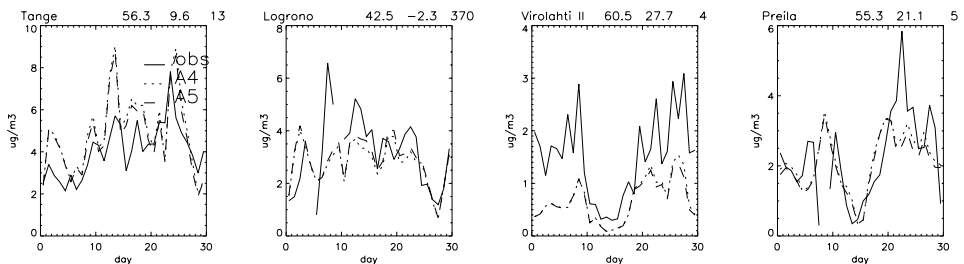


Figure 5.14: Comparison of daily averaged model values and measurements of  $NH_4^+ + NH_3$  for selected EMEP sites (August 1997).

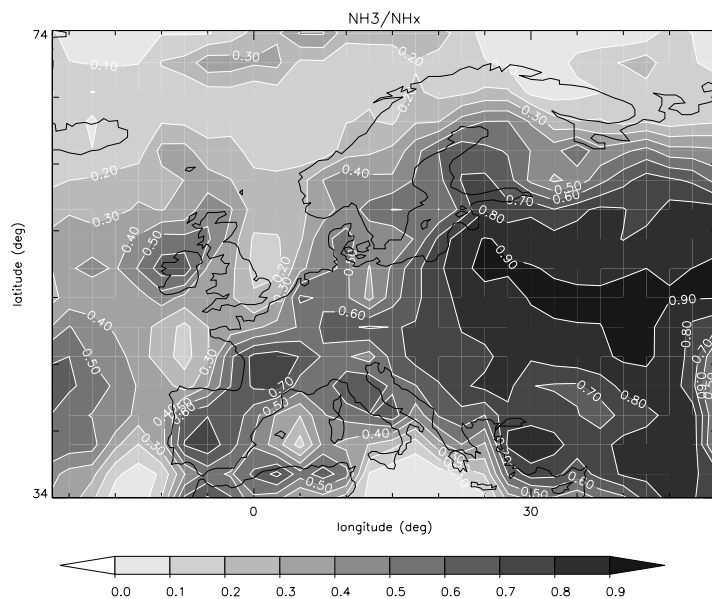


Figure 5.15: Monthly average mole fraction  $\text{NH}_3$  to  $\text{NH}_x$  at ground level for Europe, August 1997, model run A5.

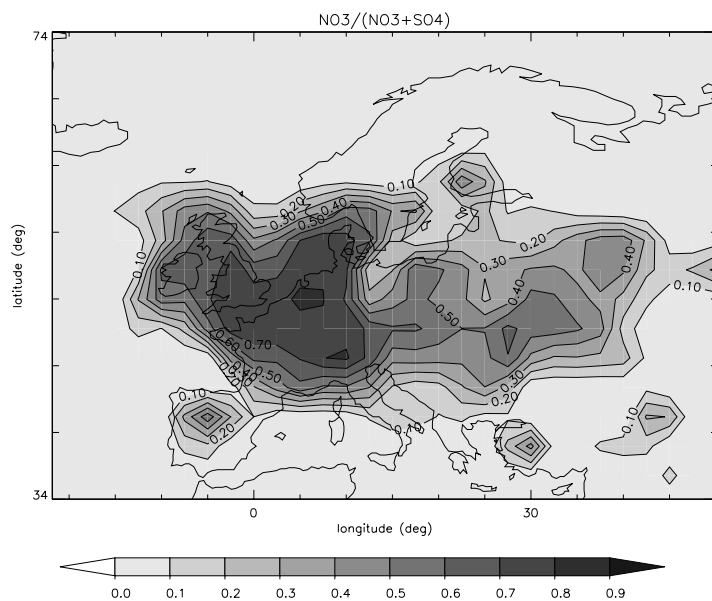


Figure 5.16: Monthly average mole fraction of  $\text{NO}_3^-$  aerosol relative to the sum of  $\text{SO}_4^{2-} + \text{NO}_3^-$  at ground level for Europe, August 1997, model run A5.

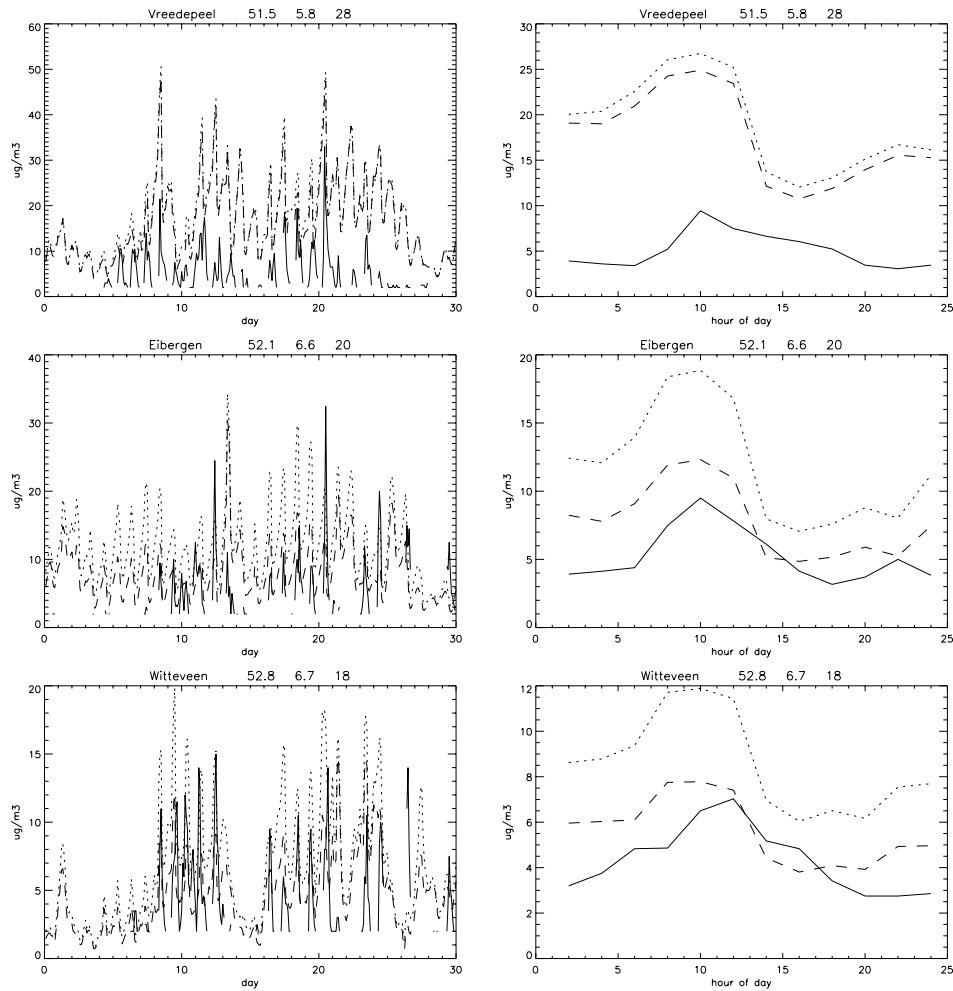


Figure 5.17: Comparison of instantaneous model values and measurements of  $SO_2$  at 3 sites in the Netherlands (from the national monitoring network of air pollution) and the average daily cycle for August 1997. The solid line is the observations, the dotted line model run A4 and the dashed line model run A5. Times are in GMT. Each station is in a different model grid since there is an intersection of 4 grid cells at  $52.5^\circ N$  and  $6.25^\circ E$ .

using the CORINAIR emissions, but is with a value of 0.39 still rather low.

Agreement between model and observations is much better for sulfate, the reaction product of  $SO_2$ . As is shown in Figure 5.12, both model runs simulate the day-to-day variability as well as the absolute magnitude of the concentrations well. At the sites where  $SO_2$  was overestimated by a factor 5 to 10 (e.g. Langenbrugge, Tange) sulfate is within 10 to 20% of the observations. Best agreement is clearly obtained with simulation A5. This is also confirmed by the improved statistics in Table 5.5.

Figure 5.16 shows that nitrate may constitute a large fraction of the TM3 aerosol

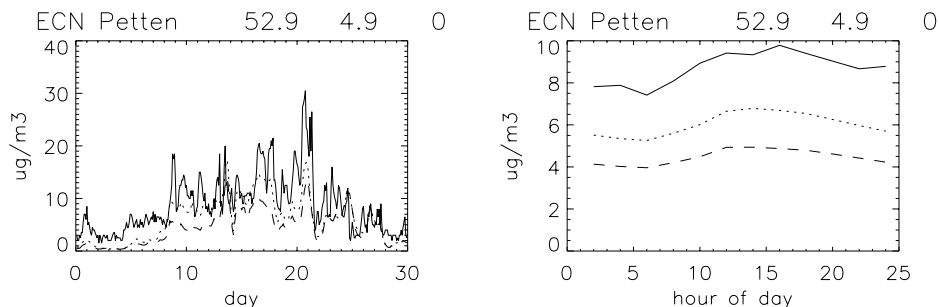


Figure 5.18: Comparison of instantaneous model values and measurements of  $\text{SO}_4^{2-}$  for Petten (The Netherlands) and the average daily cycle for August 1997. The solid line is the observations, the dotted line model run A4 and the dashed line model run A5. Correlation=0.78 and 0.71 and the average difference 2.2 and 4.2 for A4 and A5 respectively. Times are in GMT

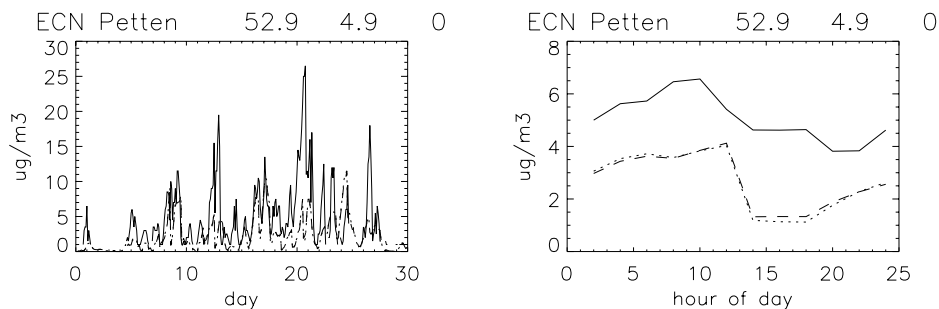


Figure 5.19: Comparison of instantaneous model values and measurements of  $\text{NO}_3^-$  for Petten (The Netherlands) and the average daily cycle for August 1997. The solid line is the observations, the dotted line model run A4 and the dashed line model run A5. Correlation=0.41 and 0.42 and the average difference 2.6 and 2.6 for A4 and A5 respectively. Times are in GMT

surface concentration (nitrate + sulfate) over large parts of Europe. Results for particulate nitrate of 4 of the 12 available EMEP sites are shown in Figure 5.13. Nitrate is difficult to model since its formation strongly depends on humidity, temperature and the concentrations of sulfate and ammonia. If the ammonia concentrations do not exceed the sulfate concentrations, no nitrate can partition to the aerosol. For Ispra in Italy, Kollummerwaard in the Netherlands and Leba in Poland, model values are in reasonable agreement with the observations. At Liesek in Slovakia no particulate nitrate is generated by the model. There is no significant difference between model simulations A4 and A5, neither for the statistical parameters shown in Table 5.5. While, particulate nitrate is on average too low, the sum of nitrate plus nitric acid is too high compared to the observations at the 8 sites that measure the sum of these components. This indicates, that the availability of  $\text{HNO}_3$  is not limiting the formation of nitrate aerosol.

	N	Correlation		Average difference(O-M)	
		A4	A5	A4	A5
SO <sub>2</sub>	1868	0.36	0.39	-4.2 ± 5.4	-2.7 ± 4.3
SO <sub>4</sub> <sup>2-</sup>	2059	0.56	0.58	-0.3 ± 1.8	0.0 ± 0.8
NH <sub>x</sub>	956	0.66	0.66	-0.5 ± 1.7	-0.40 ± 1.7
XNO <sub>3</sub>	884	0.60	0.61	-0.5 ± 0.9	-0.5 ± 0.9
NO <sub>3</sub>	401	0.66	0.66	0.3 ± 0.3	0.3 ± 0.3

Table 5.5: Correlations and average differences observation-model ( $\mu\text{g m}^{-3}$ ) based on daily averages for all available EMEP stations for August 1997. XNO<sub>3</sub> is the sum of NO<sub>3</sub><sup>-</sup> and HNO<sub>3</sub> and NH<sub>x</sub> of NH<sub>3</sub> and NH<sub>4</sub><sup>+</sup>.

The sum of ammonium and ammonia is measured at about 24 sites. Ammonium concentrations are strongly correlated with sulfate (e.g. Tange, Denmark). As was the case for sulfate, agreement between model and observations is very good (see also Table 5.5). Ammonia is a difficult species to model due to its short lifetime and heterogeneous sources. However, based on this result, there seems to be no reason to doubt about the quality of the NH<sub>3</sub> emissions in TM3. As is indicated in Figure 5.15 the the fraction ammonia in NH<sub>x</sub> is on average 50% over the European continent at surface level. Co-located ammonia measurements would however be needed to find out about the fraction ammonia in measured NH<sub>x</sub>. It is important to model this fraction correctly, since the pH of cloud water and therefore the cloud reaction rates strongly depend on the concentrations of NH<sub>4</sub><sup>+</sup>.

As has been done for radon in Chapter 4, we also compared the simulated daily variability of sulfate, nitrate and SO<sub>2</sub> with sites in the Netherlands, for which we have a detailed set of measurements. Results are shown in Figure 5.17 to 5.19. Modeled SO<sub>2</sub> concentrations exhibit a similar daily cycle as radon with accumulation of SO<sub>2</sub> in the stable boundary layer during the night and a steady decrease during the day. The measurements, however show a rather different diurnal cycle. Modeled radon concentrations agreed well with measurements indicating a good representation of the diurnal cycle in the boundary layer mixing. For SO<sub>2</sub> the situation is much more complicated. There is an indication, that there is a diurnal cycle in the emissions, which is not accounted for in the model. Observational sites are usually at rural sites away from major sources and therefore advective transport processes rather than local vertical mixing determines the daily cycle in observed SO<sub>2</sub>. In the model, however, the emissions are grid box averages. Nevertheless, the variability over the whole month is well captured by the model with both simulations generally overestimating the concentrations.

Sulfate does not show such a strong diurnal cycle (Figure 5.18). However, the correlation between both model runs and the observations is high. Both simulation A4 and A5 underestimate the sulfate levels for Petten by 25 and 50% respectively. The episodic nature of elevated sulfate concentrations is well simulated by the model.

The daily cycle of nitrate seems to be too strong in the model (Figure 5.19). Especially in the afternoon nitrate concentrations are too low. Although there must be ammonia in excess in the Netherlands, nitrate concentrations are about 50% underestimated.

The simulation of the day-to-day and diurnal variation of aerosol species provide



a severe test for the model. Given the highly variable nature of aerosols and the limited resolution of the model (e.g. The Netherlands covers a little more than one grid cell only), model simulated aerosol concentrations agree surprisingly well with the measurements.

SO<sub>2</sub> is difficult to simulate by the model due to its short lifetime and strong dependence on emissions. Using the CORINAIR emissions instead of the EDGAR emissions results in a clear improvement of not only SO<sub>2</sub> but also of sulfate and ammonium. As was the case for the comparison of monthly averages in section 5.3.1 also for August 1997 simulated SO<sub>2</sub> concentrations are too high even with reduced emissions. However, because of the ever-present emission sources within a coarse resolution grid cell, measurements which are usually performed at “regionally” remote sites might systematically underestimate the grid cell average. Clearly more attention needs to be given to modeling and validation of SO<sub>2</sub> emissions.

## 5.4 Comparison of the simulated AOD with satellite measurements

Ground-based experiments can provide detailed information on the aerosol size distribution and chemical composition. However, most of these measurements are point measurements near the surface, and may not be representative for the aerosol throughout the boundary layer and free troposphere, as we have seen in section 5.2.3. Aircraft observations are very expensive and therefore not suitable for long-term monitoring. Satellite remote sensing on the other hand can provide daily measurements of column integrated aerosol properties, such as the spectral aerosol optical depth (AOD), on spatial scales ranging from a few kilometers to global. The spectral AOD potentially holds information on the aerosol load and on the aerosol size distribution [Tanré *et al.*, 1996], and limited information can be derived on the chemical composition. The disadvantages of satellite remote sensing measurements are the lack of profile information, and the relatively large time span (usually more than 24 hrs) between two successive satellite overpasses over an area.

Combination of aerosol satellite remote sensing and transport modeling can be applied for interpretation of observed spatial aerosol distributions, as observed from the satellite. At present we have available the AOD derived from observations from the Global Ozone Monitoring Experiment (GOME) in the wavelength range between 0.340 and 0.400  $\mu\text{m}$  and from the Along Track Scanning Radiometer 2 (ATSR-2), at 0.555  $\mu\text{m}$ . Both instruments fly on board of the European ERS-2 satellite. In this section the satellite derived AOD is compared with calculations from the TM3 model. The comparison is made for a scenario over Europe, for August 1997. The total AOD is estimated from the column burden of the sum of sulfate, nitrate and associated aerosol water. Since it is well known from measurements [Ten Brink *et al.*, 1996b] that a significant fraction of the aerosol consists of additional aerosol species, e.g. carbonaceous or seasalt aerosol, we concentrate on spatial patterns rather than absolute values of AOD. Organic aerosols are partly resulting from anthropogenic activities. Therefore it seems reasonable to assume a correlation between the total AOD and the AOD of sulfate plus nitrate.

### 5.4.1 Satellite data

Data from ATSR-2 have been used to derive the spatial distribution of the aerosol optical depth (AOD) over Europe for August 1997 [Robles-Gonzalez *et al.*, 2000]. The ATSR-2 is a radiometer with seven wavelength bands, four of these bands are in the visible and near infrared (effective wavelengths 0.555, 0.659, 0.865 and 1.6  $\mu\text{m}$ ) and potentially useful for aerosol retrieval. A unique feature of the ATSR-2 is the dual-view capability providing two views of each region: first a forward view (zenith angle approximately  $55^\circ$  and about 2 minutes later a nadir view. The AOD is retrieved in cloud free areas using the dual-view algorithm [Veefkind and de Leeuw, 1998]. This algorithm uses both the two-angle view and the spectral information of the ATSR-2 measurements to distinguish between top of the atmosphere and surface contributions to the backscattered radiation. In contrast with most other existing aerosol retrieval methods the dual-view algorithm can in principle be used both over land and over the ocean. Over coastal waters, however, the algorithm still experiences some problems because of the complex determination of the angular dependence of the surface albedo when sediment is visible. Once the atmospheric contribution is determined, the AOD is computed using a two-mode aerosol size distribution. The ratio between these modes is derived from the spectral behavior of the atmospheric radiance contribution.

The dual-view algorithm was validated by comparison with ground based sun photometer data for the east coast of the USA [Veefkind *et al.*, 1998] and for north-western Europe [Veefkind, 1999]. These comparisons show that the satellite retrieved AOD is well within 0.1 of the co-located sun photometer data. This result yields confidence that the algorithm can be applied over most of western Europe, except possibly over highly reflecting surfaces, such as those covered with snow and semi-arid areas.

From the GOME data the AOD was derived in the wavelength range between 0.342 and 400  $\mu\text{m}$ . As shown by Herman and Celarier [1997] the albedo of most land surfaces is between 0.02 and 0.04 in this wavelength range. Because of the low albedo most of the radiation reaching the satellite is due to scattering in the atmosphere. Five spectral bands (0.342, 0.355, 0.368, 0.388 and 0.400  $\mu\text{m}$ ) with widths of 1 nm were selected from the GOME spectra. The atmospheric and surface reflection contributions are separated using a prescribed value for the surface albedo. The AOD is computed by fitting a two-mode aerosol model through the spectral data. Since this method is based on aerosol scattering, it differs from the TOMS UV aerosol index [Herman *et al.*, 1997] which detects mainly absorbing aerosol. In comparison with ATSR-2 the GOME algorithm does not experience problems with land-sea changes. However, with a resolution of 40 times 320 km the GOME pixels are very likely to be contaminated by clouds, resulting in only few available measurements.

### 5.4.2 Modeling the aerosol optical depth

The TM3 model provides the spatial and temporal distribution of the mass of sulfate and nitrate aerosol. The aerosol mass and chemical composition is also dependent on the amount of ammonium present in the aerosol. This fraction is explicitly calculated by the aerosol equilibrium module of TM3 (see section 5.2.2).

To derive the AOD of the sulfate/nitrate aerosol, assumptions are made on the

aerosol size distribution. Other aerosol species, such as organic aerosols contribute significantly to the total AOD. Additional assumptions could be made to account for the contribution of these “missing” aerosol species. Studies in the Netherlands in the 1980s and 1990s for instance showed that the contributions of sulfates and nitrates to aerosol scattering are comparable [Diederen *et al.*, 1985; Ten Brink *et al.*, 1996b]. Large parts of the fine particle mass could not be identified, and were presumed to be carbonaceous material. Ten Brink *et al.* [1996b] speculated that the contribution of sulfate to particle scattering was between 30 and 40%. Diederen *et al.* [1985] found that sulfate scattering contributed 38% to the total aerosol extinction. These fractions which pertain to the Netherlands may be significantly different elsewhere. A complication is that the optical properties of especially organic aerosols are not well known. We therefore ignore this unknown aerosol fraction from the calculation of the AOD and focus on spatial patterns in the AOD field.

Following the approach of Kiehl and Briegleb [1993], the AOD is expressed as:

$$AOD(\lambda) = f(RH, \lambda)\alpha_{SO_4}(\lambda)B_{SO_4} \quad (5.5)$$

where:  $\alpha_{SO_4}$  is the mass extinction efficiency of sulfate; i.e. extinction coefficient per unit of mass  $SO_4^{2-}$  at relative humidity (RH) < 40%;  $B_{SO_4}$  is the sulfate column burden; and  $f(RH, \lambda)$  is the relative increase of the scattering coefficient at given RH to the scattering at low (<40%) RH. In Equation 5.5  $\alpha_{SO_4}$  and  $f(RH)$  depend on the aerosol size distribution and chemical composition of the particles. The aerosol size distribution was assumed to be lognormal, with a geometric mean radius of 0.05  $\mu\text{m}$  and a geometric standard deviation of 2.0. The dry density of the particles was taken as 1.7  $\text{g cm}^{-3}$ .  $\alpha_{SO_4}$  was evaluated using a Mie code.

Using the above assumptions, the AOD by sulfate/nitrate aerosol at low RH is calculated from the model predicted sulfate, nitrate and ammonium mass and the sulfate mass extinction efficiency. This implies that for nitrate aerosol the same mass extinction efficiency is assumed as for sulfate aerosol.

Most aerosol particles absorb water vapor when exposed to increasing RH. The particle growth results in more scattering by the aerosol particles, and consequently a higher AOD. To account for the increase of aerosol extinction with increasing RH, the factor  $f(RH, \lambda)$  is used in Equation 5.5. This factor is the ratio between aerosol extinction at given RH to aerosol extinction at low RH (<40%). The increase of the scattering coefficient with increasing RH can be measured by humidity controlled nephelometry. Veeffkind *et al.* [1996] have measured  $f(RH)$  in the Netherlands in November 1993, for days with a continental airmass. A polynomial fit to these experimental data is used to describe  $f(RH)$ . Mie calculations showed that the wavelength dependence of  $f(RH)$  can be ignored. To compute the humidity effect on the AOD in TM3 the polynomial fit is used together with 3-dimensional relative humidity fields which are calculated every 6 hours based on ECMWF temperature and specific humidity fields.

The calculation of the AOD is done every time step (=40 minutes) on-line in TM3 for the spatial resolution of  $2.5^\circ$  by  $2.5^\circ$  and 31 levels. By using the derivative of the tracer mass field in all spatial directions, which is calculated and stored in the advection module of TM3, we output the model AOD on a higher resolution of  $1.25^\circ$  by  $1.25^\circ$ . Note that the higher resolution structures obtained in this way are a result of advective transport processes only.

### 5.4.3 Results

First we compare the AOD of the TM3 aerosol field with the AOD of ATSR-2 at  $0.555\mu\text{m}$ . For this purpose all available cloud free ATSR-2 pixels for August 1997 are combined into a monthly averaged composite field for Europe. Such a composite field presents a rather biased view of the monthly averaged aerosol field. For instance over England and Scotland the average consist of a few points in time only, while for other more sunny areas each overpass might be included. Under cloudy conditions the AOD is probably lower, as a result of wet scavenging. Therefore the high values of the ATSR-2 composite field (5.20 upper panel) probably show an upper limit for the aerosol pollution over Europe.

In this section again we focus on two model simulations, A4 and A5 (Table 5.3). It is investigated whether the change in the input emissions is visible in the simulated AOD patterns. The model simulations were allowed one month spin-up time, by starting at July 1st. Model output was generated at 11 UTC, the approximate time of overpass for ATSR-2 over Europe. AOD fields from both model simulations are interpolated to the high resolution of the ATSR-2 data. Next, the composite average is calculated for the cloud-free ATSR-2 pixels, in order to get a comparable average as for ATSR-2. Two model simulations have been compared with the satellite image: one simulation (**A4**) used the EDGAR data as emission source for SO<sub>2</sub> and the other one (**A5**) the CORINAIR data.

Figure 5.20 shows that model captures the main features observed by ATSR-2, like the maxima over the Po valley and the south of Italy, the Barcelona area, the maximum over the Netherlands, and the urban areas along the Scandinavian coast. Especially noteworthy are the well-simulated peak values over England, as they are an average of one or two overpasses only. Also the low AOD values over north Scandinavia are simulated well.

The variability in the satellite data is not quite reproduced by the model simulations. Of course it can not be expected that the small scale variability is resolved by the relatively coarse grid model. However, at large scales also some important sources of aerosols seem to be missing, especially over southern France, Spain, eastern Europe and the Balkan. Possible explanation for these missing aerosol sources could be the production of large amounts of secondary organic aerosols resulting from biogenic and anthropogenic sources [Kanakidou *et al.*, 2000]. This secondary production might be enhanced under photo-chemical smog conditions with high ozone levels [Griffin *et al.*, 1999]. For the south of Europe in addition dust aerosol originating from the Sahara or locally produced may play a role.

The narrow colored borders at the land-sea boundaries, which are clearly visible in the ATSR-2 image is not represented by the model. Sea salt aerosol, which is also not simulated by the model, may explain this difference. Also the retrieval algorithm is expected to experience problems in simulating land sea changes.

Model simulation **A5** in general is not much different from **A4**. The AOD pattern over Spain seems to be slightly better simulated when using the CORINAIR emissions for SO<sub>2</sub>. Also the maximum over the Netherlands is less pronounced which is in better agreement with ATSR-2. Due to the much lower sulfur emissions, the AOD for **A5** is on average about 0.03 lower than for **A4**. So the difference between **A4** and **A5** is much less than the factor 2, which is the difference in emissions of SO<sub>2</sub>. This again indicates that the amount of sulfate aerosol produced is relatively insensitive to the

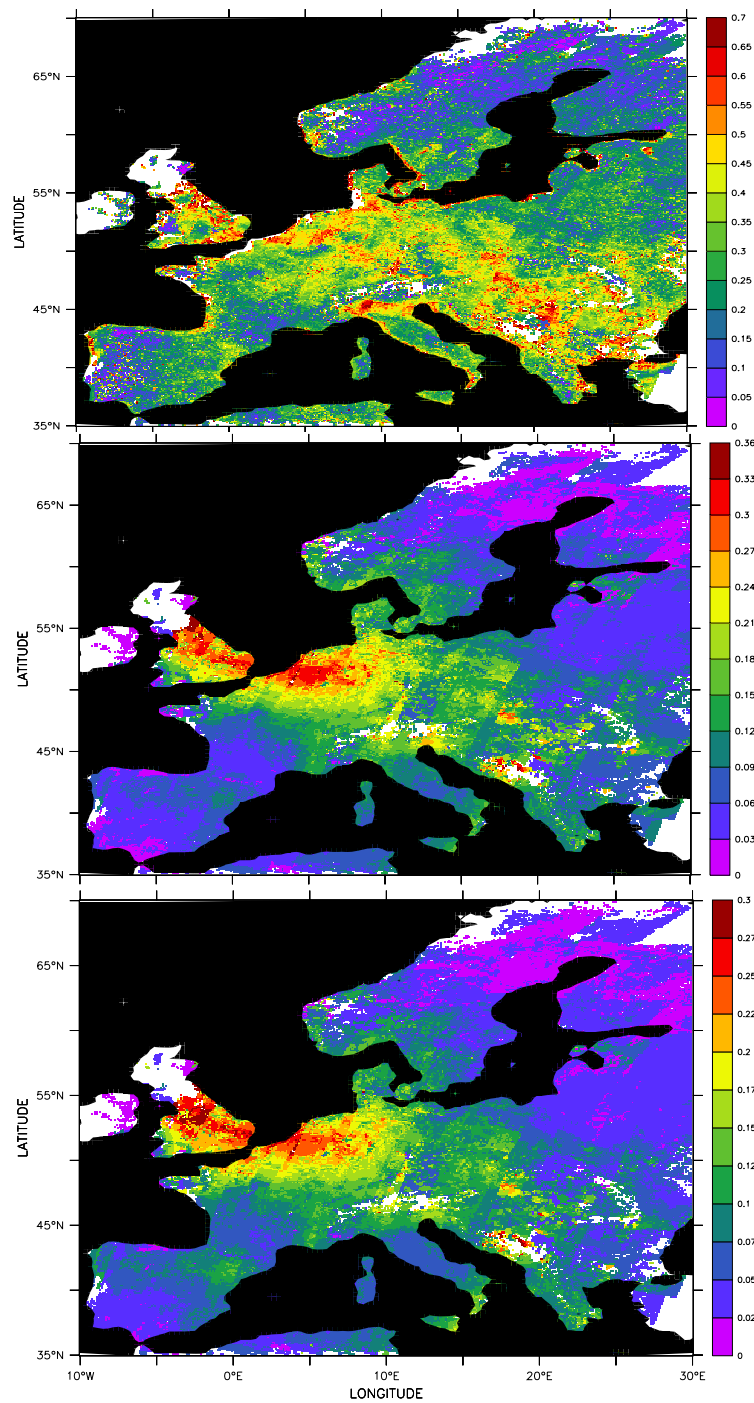


Figure 5.20: Composite (only data for cloud free pixels have been used) monthly averaged field of the AOD at 555nm for Europe August 1997. Upper panel is ATSR-2, middle and lower panels are TM3 simulations A4 and A5 (Table 5.3).

source of its precursor.

On average there is a difference between the model simulations and ATSR-2 in the AOD of 0.2. This is demonstrated in Figure 5.21, which shows the zonal and meridional averages of Figure 5.20. We simply added 0.2 to the model AOD values, which results in a surprisingly good agreement between model and satellite. The question is how this offset of 0.2 should be interpreted. We should not forget that the TM3 model with its coarse resolution only simulates the water soluble aerosol species  $\text{SO}_4$  and  $\text{NO}_3$  and the complex mix of various other aerosol species is not included. The ATSR-2, on the other hand observes the whole aerosol burden. Particularly in the east-west direction the model simulations correlate well with the ATSR-2 AOD. The apparently constant offset suggest that the missing part in AOD is some sort of background aerosol which is well mixed. However, the north-south gradient in AOD from  $60^\circ$  to  $70^\circ\text{N}$  is not so well simulated by the model. Apparently a constant offset of 0.2 is not appropriate for the North of Europe. Emission and formation of organic aerosol are temperature dependent processes. It seems therefore reasonable to assume that there is a north-south gradient in organic aerosol production. In addition desert dust influences over Europe strongly decrease from south to north. Also Figure 5.20 does not really support the suggestion of an additional well mixed layer.

To conclude this section we present a case for the 21st of August. For this day we were also able to produce a relatively complete track of GOME AOD (due to its large pixel size it is difficult to find cloud free pixels). Since GOME is using a fundamentally different retrieval algorithm and has a much larger pixel size, it is interesting to compare with both.

Figure 5.22 shows that the model simulations, reproduce the observed maximum over the Netherlands and the strong gradient herein. The maximum over the gulf of Bothania and southern Sweden is also simulated by the model. The maximum over eastern Germany is almost completely absent in the model results. However, considering that this comparison only presents a snapshot, agreement between the model simulations and the satellite measurements is good. Figure 5.22 also shows that, although the ATSR-2 image exhibits a lot more fine scale structure, agreement between ATSR-2 and GOME AOD patterns is very good. This lends additional confidence to the quality of the satellite retrievals.

## 5.5 Discussion, conclusion and outlook

In the previous two sections we have evaluated the sulfur cycle included in the TM3 model, by considering variations on different temporal and spatial scales. The influence of model changes in vertical diffusion, below cloud scavenging and emissions has been evaluated.

Annual averaged global budgets show that when the new diffusion parameterization, which produces on average more vertical diffusion, is used more  $\text{SO}_2$  is oxidized and less of it is deposited at the earth's surface. Below cloud scavenging appears to be an effective sink for  $\text{SO}_2$ , however associated with large uncertainties. Changes in the global  $\text{SO}_2$  and sulfate burden are, however, very small due to feed back processes. For instance, the increase of sulfate production in clouds is partly compensated by the increased wet scavenging. This explains the only small improvements of model results compared with measurements of  $\text{SO}_2$  and sulfate at various remote sites around

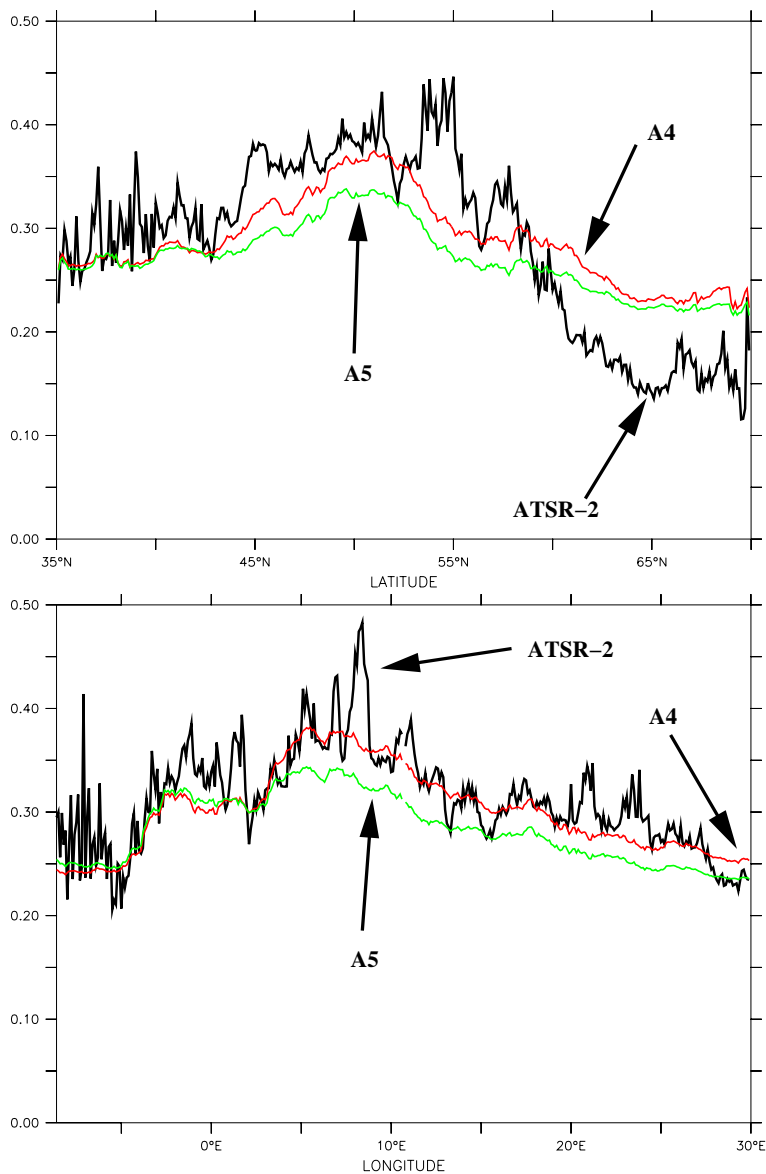


Figure 5.21: *Composite zonal and monthly average for August 1997 for Europe (upper panel and meridional average (lower panel) for model runs A4 and A5 (+0.2) and ATSR-2.*

the globe. For radon concentrations, which is a much simpler tracer, generally much larger effects of the change in vertical diffusion scheme were found (see Chapter 4). Thus, due to the strong coupling between upward mixing, oxidation and scavenging in the clouds and dry deposition at the surface it is difficult to achieve substantial changes in the calculated concentrations of sulfate and  $\text{SO}_2$ .

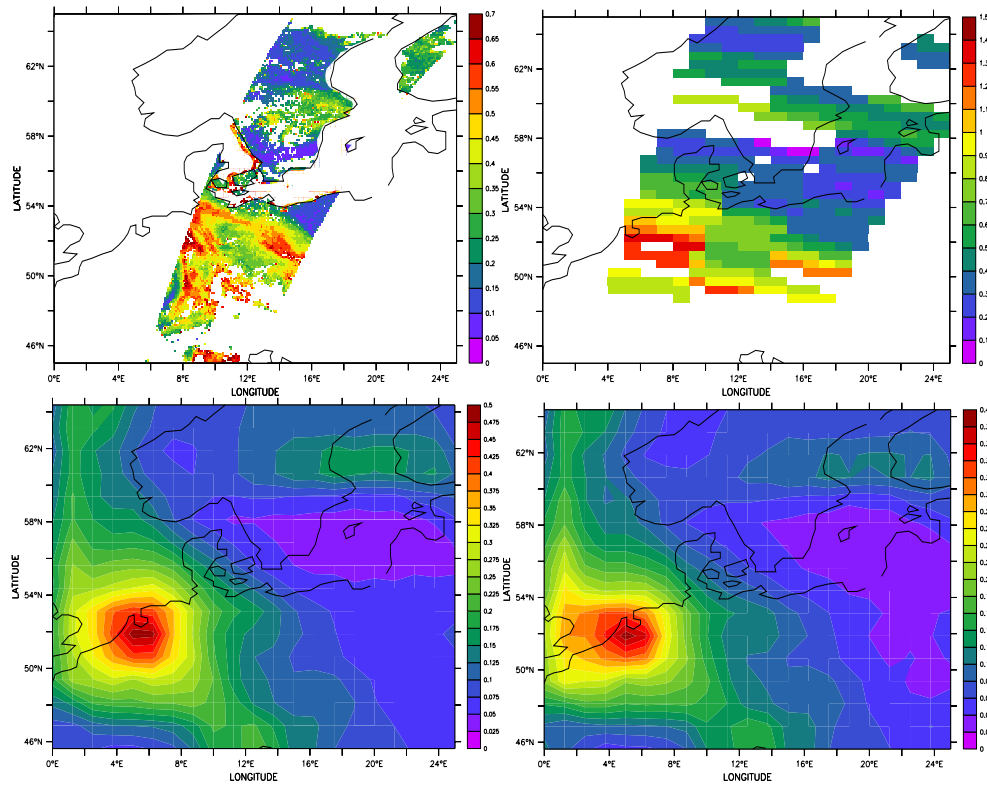


Figure 5.22: AOD for 21st August 1997 for ATSR-2 (upper left), GOME (upper right), model run A4 (lower left) and model run A5 (lower right). Note that the AOD for ATSR-2 and the model is for  $0.555\mu\text{m}$  and the AOD of GOME for  $0.342\text{-}0.4\mu\text{m}$ .

Nevertheless, results for sulfate are quite satisfactory. In summer the observed surface concentrations are well simulated, while in winter at high latitudes it is underestimated.  $\text{SO}_2$  surface concentrations, on the contrary, are strongly overestimated by TM3 especially in winter. This is a well known problem in most global sulfur models [Barrie *et al.*, 2000]. The combination of too low sulfate and too high  $\text{SO}_2$  concentrations, indicates that in the model in winter oxidation processes are a limiting factor. Further research is needed on this topic. In addition the overestimation of  $\text{SO}_2$  is larger than the underestimation of sulfate. This might be an indication that non-chemical sinks for  $\text{SO}_2$ , other than sulfate production, are too small or that the emissions are too large.

This latter argument has been investigated in section 5.3.3. The agreement between model results and observations for Europe indeed improves when lower emission estimates are used. Since the below cloud scavenging of  $\text{SO}_2$  probably is on the high side already, it should be considered that the dry deposition in the model is too small.

Comparison of simulated profiles with aircraft measurements shows that the agreement between model and measurements is good for  $\text{H}_2\text{O}_2$  and reasonable for  $\text{SO}_2$  and sulfate. The observed high variability in the vertical of  $\text{SO}_2$  and sulfate is not al-



ways reproduced by the model. This demonstrates that it is difficult for a coarse grid model to simulate the detailed processes causing this variability. One example is cloud processing which in reality acts on much smaller spatial scales than included in our  $3.75^\circ$  by  $5^\circ$  resolution model. Over eastern Canada, north of Toronto we find consistently too high  $\text{SO}_2$  and too low sulfate concentration in the boundary layer for March 1990, probably related to the before mentioned limitation of oxidation. The profiles also show that elevated levels of  $\text{SO}_2$  and sulfate do not exclusively exist in the boundary layer, stressing that by surface measurements alone the characterization of the vertical aerosol burden, needed e.g. for the calculation of the radiative forcing, can not be well established. There are too little profile measurements available to be able to systematically validate simulated vertical aerosol distributions.

With the high resolution version of TM3 ( $2.5^\circ$  by  $2.5^\circ$  and 31 levels in the vertical) we obtain very good agreement between simulated and observed day-to-day variability of sulfate and ammonium and to a lesser extent nitrate concentrations in Europe. It is also shown that  $\text{SO}_2$  concentrations strongly depend on the distribution and magnitude of emissions. Pronounced differences, up to a factor 2, exist between commonly used emission data bases for Europe. It is possible that comparable differences can be found elsewhere. For Europe, it is likely that the CORINAIR data provide a more accurate estimate of the real emissions than the EDGAR data, based on the knowledge that for 1997 the EDGAR data have been extrapolated using energy statistics without taking into account the increase of the emission factors from 1990 to 1997. Results for  $\text{SO}_2$  also confirm this. The average overestimation of surface concentrations is reduced by almost a factor two. However, the simulated concentrations remain too high. Also the results for sulfate improve considerably, by using the CORINAIR emissions. Whereas a factor two in emissions also results in a factor two difference in simulated  $\text{SO}_2$  concentrations, the absolute magnitude of sulfate is relatively insensitive, indicating again that the production of  $\text{SO}_4^{2-}$  is not only limited by the supply of  $\text{SO}_2$ .

The comparison of simulated  $\text{SO}_2$  concentrations and observations for Europe is strongly hampered by the presence of sources within the same model grid cell as the measurement site. This is the case for a large part of the EMEP sites, when using a model with a grid cell size of approximately 250 by 250 km. In the model instant mixing of emissions is assumed within a grid cell. In reality emission sources and measurement sites are at some distance from each other. Whereas the model provides an estimate of the gridbox averaged concentration, which is strongly influenced by the emission sources, the measurement may provide an estimate of a sort of local background concentration or vice versa is rather influenced by a nearby source. In addition, under stable conditions, a strong gradient in the  $\text{SO}_2$  concentration might exist between the measurement height (e.g. EMEP standard is 3.6m) and the average height of the lowest model level ( $\pm 30\text{m}$ ). For a depositing component like  $\text{SO}_2$  this implies that using the model 30 meter concentration may give an overestimation compared to an observation obtained at 3.6 meter, at least when there are no nearby low-altitude sources. Therefore, the representativity of the measurement sites for  $\text{SO}_2$  should be better established, by better selecting measurements, using information on local sources and measurement height. In addition a zoom version of the TM3, currently under development, which has a higher resolution than currently used, would further facilitate comparison between model and observations.

Although the representativity of the measurement locations presents a problem, it

is remarkable that at some stations there is good agreement (e.g. Preila, Shepeljevo in Figure 5.11) between modeled and measured  $\text{SO}_2$  and at others  $\text{SO}_2$  is strongly overestimated. There seems to be no reason that model physics would be better or worse for different areas. Therefore this might be an indication that over some parts of Europe emissions are still overestimated. Another aspect is the temporal variation of emissions. The model only takes into account seasonal variations. It should, however, be investigated how  $\text{SO}_2$  emissions vary on shorter time scales. Since boundary layer mixing has a strong diurnal cycle, especially diurnal variations in emissions might be important.

From the comparison between the model simulated and the satellite measured aerosol optical depth, it appears that the observed patterns are well represented by the model but that an important part of about 0.2 in AOD is missing. Surprisingly, the results in first instance suggest that this part is fairly constant over most of Europe, indicating a well mixed background aerosol. Aerosol types, which are not included in the model, like organic aerosol and desert dust are typically not so well mixed. A better explanation would be given by stratospheric aerosol which is not accounted for in the model. However, in periods without major volcanic eruptions, the stratospheric AOD does not exceed 0.01 at 555nm [Sato *et al.*, 1993].

To be able to compare model and satellite AOD more quantitatively, missing aerosol species should be included in the model. In addition to facilitate comparison of model and satellite data both the model and the retrieval algorithm should use the same assumptions on the optical properties of the aerosol.

We have seen that when using lower emission estimates of  $\text{SO}_2$  the agreement between model and measurements at the surface improve for sulfate. Based on the comparison of the simulated column integrated AOD with satellite measurements, no such improvement is obtained. This could indicate that free tropospheric sulfate is underestimated. However, we must also realize that there are too many unknown factors too support this conclusion.

To summarize, the major uncertainties in the modeling of the sulfur cycle are:

1. **Emissions** of  $\text{SO}_2$  are a major uncertainty in the model and more accurate and temporally better resolved estimates are needed.
2. Due to the strong coupling between **Vertical mixing** and in-cloud oxidation of  $\text{SO}_2$ , the parameterization of vertical diffusion in sulfur simulating models plays an important role. As indicated in Chapter 4 and in this chapter the vertical mixing in TM3 over the continents is probably still underestimated. Increased mixing would bring  $\text{SO}_2$  surface concentrations in better agreement with observations and lead to extra oxidation, which especially in winter could also lead to higher sulfate levels, provided that the oxidation is not limited by the availability of  $\text{H}_2\text{O}_2$  or presence of clouds.
3. Various **chemical factors** can play a role. For instance heterogeneous reactions on aerosol could provide an additional sink for  $\text{SO}_2$  when no clouds are present. Mineral aerosol could have an influence on the cloud acidity and in this way influence  $\text{SO}_2$  oxidation rates. The few measurements in this chapter showed that in general  $\text{H}_2\text{O}_2$  is well simulated by the model. However, more validation is needed, especially for the winter season, to be more conclusive about the problem of oxidant limitation.

4. Wet and dry **deposition** have been modeled fairly detailed in TM3. Based on results of  $^{210}\text{Pb}$  and the comparison of simulated sulfate profiles for the NARE and EMEFSII campaigns, we get the impression that wet deposition may be too effective. On the other hand extra oxidation of  $\text{SO}_2$  via one of the above mentioned mechanisms would also lead to higher aerosol concentrations. Dry deposition of  $\text{SO}_2$  is very much dependent on surface characteristics. Since the effective solubility of  $\text{SO}_2$  is high, especially the wetness of the surface could be an important factor. In TM3 the wetness of the surface is prescribed with climatological values. It should be investigated what effect the temporal variation of the surface wetness would have on dry deposition of  $\text{SO}_2$ .

All measurements used in this chapter have been from different periods and for different regions, and have given us useful hints. To find a more conclusive answer, simultaneous high quality measurements of profiles, column burden and surface measurements for a variety of regions, covering at least a full seasonal cycle, are highly needed.

Given all uncertainties, we obtain reasonable agreement for sulfate between TM3 model simulations and observations from various platforms and on various times scales. This gives us confidence that the changes to the model i.e. the better description of the boundary layer diffusion, the detailed description of wet scavenging processes and the parameterization of gas-aerosol partitioning, have resulted in a clear improvement of the model's ability to simulate global aerosol fields.

Combination of remote sensing of aerosols and transport models should be considered for data assimilation. In data assimilation the satellite measured aerosols fields can be used as input for the transport models which then provide "smart" interpolations to fill the (spatial and temporal) gaps between satellite overpasses. Data assimilation can be used to predict the evolution of the aerosol field. This information can be used as a first guess for the aerosol retrieval algorithms for the next overpass and it will improve the quality of the retrieval. In addition data assimilation allows for a critical review of the importance of the different processes involved.

## Chapter 6

# Conclusions and Outlook

The general aim of this thesis is to evaluate global chemistry and climate models by using measurements and data assimilation techniques. By confronting the model with measurements, model weaknesses can be revealed and the impact of model changes can be assessed. More specifically, this thesis aims at applying and developing data assimilation methods, at performing model-observation comparisons but also at developing improved parameterizations for the TM3 model. This is an iterative process. Model changes should be re-evaluated using measurements, which in turn leads to new insights and new adaptations. Also new measurements, from other platforms or at other locations may lead to new insights. Model evaluation or validation is not a goal by itself, but merely an essential step to gain confidence in the models used in atmospheric chemistry and climate research. By validating the models that describe atmospheric processes, we learn to understand these processes and in this way are better able to draw conclusions about major climate and atmospheric chemistry issues.

The climate model ECHAM was developed from the ECMWF weather prediction model to be used for climate predictions. Like weather prediction models a climate model diverges quickly from the actual atmospheric conditions due to its chaotic nature. Therefore its output can not be directly compared with instantaneous measurements but only with climatologies of measurements. For many model variables such climatologies are not available. Valuable measurements from campaigns can not be used for validation since they are only available for short time-scales. Therefore in chapter 2 a method has been developed enabling comparison of output of the ECHAM model with measurements for specific periods.

Newtonian relaxation, a simple data assimilation method, has been used to force the evolution of the vorticity, divergence, temperature and surface pressure in the ECHAM model towards the observed evolution of these quantities. The meteorological analysis from the ECMWF numerical weather prediction model are used as observational fields. It appeared that by using relaxation times in the order of a few hours to a few days, the ECHAM model is able to follow the observed state of the atmosphere well. High correlations were obtained between observed and modeled meteorological fields, especially in the extra-tropics. Care has to be taken, however, that the forcing by Newtonian relaxation is not too strong because the intensity of parameterized physical processes might be reduced. It was for instance shown that

by increasing the relaxation coefficients, the vertical exchange via boundary layer diffusion and via moist convective processes is reduced. Recently the method has been successfully applied in several model studies in which the ECHAM model has been compared with observations.

Ozone is one of the most important components in atmospheric chemistry. For this reason it is continuously monitored by satellite instruments. In Chapter 3 an optimal interpolation (OI) data assimilation method has been presented for the assimilation of total ozone measurements from the TIROS Operational Vertical Sounder (TOVS) in the 3-dimensional chemistry transport model TM3. Differences between observed and modeled ozone columns had to be distributed in the vertical direction in the model. For this purpose three different methods for specifying the vertical weight functions have been tested. It is concluded from an independent comparison with TOMS data that modeled ozone columns have improved by the assimilation of the TOVS observations and being in closer agreement with the TOMS data than the TOVS data itself. Synoptic features present in the high resolution ozone data are well represented by the model. From comparisons with ozone sondes it is concluded that the model correctly simulates dynamical features in the ozone profiles. Due to the small model column error compared to the observation error, corrections to the model resulting from the assimilation are relatively small. Distributed in the vertical, these corrections are even smaller. Therefore only little impact is noticed of the data assimilation on the vertical ozone distribution and three rather different vertical weight functions give very similar results.

Besides that the data assimilation has enabled the construction of three dimensional synoptic maps of ozone it has also provided insight about the performance of the model in simulating the transport and chemistry of ozone. Systematic differences between model and observations were revealed, leading to the conclusion that the model vertical resolution in the stratosphere is too coarse and that a more realistic ozone chemistry for troposphere and stratosphere is required for a better simulation of ozone profiles.

Atmospheric aerosols are important components in the atmosphere since they have a strong impact on the radiation balance and thus on climate. Sulfate, ammonium and to a lesser extent nitrate are important aerosol components. Therefore these components have been included in the TM3 model, together with their sources and sinks. The high variability of aerosols and its precursors puts high demands on the model. For short-lived components like  $\text{SO}_2$  and  $\text{NH}_3$  with large and heterogeneous emission sources within the boundary layer, vertical mixing should be well represented in the model. For water soluble components and cloud condensation nuclei, scavenging processes should be well simulated by the model. In Chapter 4, therefore, an improved vertical diffusion and precipitation scavenging parameterization was described.

To exclude effects of chemistry, deposition and wet scavenging, the radio nuclide radon ( $^{222}\text{Rn}$ ) has been used to test the influence of the new vertical diffusion scheme in TM3. Simulated radon concentrations from a model run with and one without the new parameterization were compared with measurements. It was concluded that mainly due to the better temporal resolution of 3 hours instead of 6 used for the new scheme the diurnal cycle in radon surface concentrations is much better resolved by

---

the model. In addition also the absolute concentrations were better simulated with the new diffusion scheme but were still somewhat overestimated by the model indicating that mixing remains underestimated. It was suggested that the parameterization of vertical diffusion is sensitive to the resolution of the meteorological input data which is lower than the original resolution of the ECMWF model. Due to interpolation of the ECMWF wind and temperature fields to the input resolution of TM3, profiles become smoother and more stable resulting in less mixing. It is therefore recommended that diffusion coefficient are calculated at a resolution as close as possible to the original ECMWF resolution.

Instead of using a climatology of the vertical distribution of precipitation rates, in the new proposed scavenging scheme the generation of precipitation is calculated in TM3 itself from the cloud liquid and ice content obtained from ECMWF. In this way a three-dimensional distribution of precipitation was obtained which was applied to remove gases and aerosol by large scale precipitation. The removal of tracers in convective clouds has been parameterized as a function of the updraft mass flux. The radio active decay daughter of radon  $^{210}\text{Pb}$  was used to test the new scheme. Since  $^{210}\text{Pb}$  attaches indiscriminately to aerosol particles and has no further sinks than wet and dry deposition it is a good tracer to validate the removal of aerosols by precipitation scavenging. It was concluded that in comparison with the old scavenging scheme used in TM3,  $^{210}\text{Pb}$  was removed by precipitation much more effectively, especially at high latitudes. In comparison with measurements the new scheme performed somewhat better. However, in wintertime there seems to be a slight overestimation of observed  $^{210}\text{Pb}$  surface concentrations.

The changes in vertical diffusion and precipitation scavenging were included in the tropospheric chemistry version of TM3. In addition the chemistry of sulfur and reduced nitrogen species and a thermodynamical equilibrium parameterization, describing the partitioning of ammonia and nitric acid between aerosol and gas phase, were added to TM3. With this model version various simulations were performed and model output was compared with measurements on different temporal and spatial scales. The main conclusion was that sulfate aerosol distributions, are well simulated by the model. Both the absolute magnitude and the seasonal and day-to-day variability agreed well with observations.

$\text{SO}_2$  emissions appear to be the most uncertain factor in the modeling of the sulfur cycle. The sum of all emission in the CORINAIR data set for Europe is a factor two lower than that of the default data set in TM3. By applying this CORINAIR data set in TM3,  $\text{SO}_2$  surface concentrations for August 1997 were reduced by almost a factor two but appeared to be still much too high. Therefore more attention should be directed towards more accurate estimates of emissions. However, too high  $\text{SO}_2$  surface concentrations also seems to be a more fundamental problem in TM3 as well as in most global sulfur models. In winter, in addition this leads to too low sulfate levels. Partly based on the findings of the radon simulations, it was concluded that an increase in vertical mixing under stable conditions in combination with an extra oxidation mechanism would be the most likely solution to reduce the systematic overestimation of  $\text{SO}_2$ .

With surface measurements alone, the complex mechanisms and feed backs within the sulfur cycle can not be fully understood. A clear lack of profile measurements

has been pointed out. These profiles are necessary to understand what is happening above the boundary layer where, according to the model and a few measured profiles, a major fraction of sulfate and  $\text{SO}_2$  resides.

It has been shown that with satellite measurements of the aerosol optical depth (AOD), patterns in the modeled aerosol column burden can be analyzed. TM3 simulated aerosol patterns correlate well with the patterns observed by the ATSR-2 instrument. About 40% of the measured AOD could be explained by the aerosol and associated water simulated by the model. However, large uncertainties remain in the modeling and retrieval of the AOD. Additional aerosol species should be included in the model and the model and retrieval algorithm should use the same assumption about the optical properties of the aerosol. To understand discrepancies better, additionally profiles at representative locations should be measured.

In general, it is shown that by comparing model and measurements or more systematically by assimilating measurements, the insight in modeled atmospheric and chemical processes has improved.

## Outlook

Both the climate model ECHAM and the chemistry transport model TM3 will continue to be valuable tools within the research field of atmospheric chemistry and climate in the future.

With the possibility of direct comparison of model output and observations offered by the Newtonian relaxation techniques, chemical modules in the ECHAM model can be validated. In addition, the interaction between chemistry and the model processes of cloud formation and radiation scattering and absorption can be studied with a climate model like ECHAM. Due to the strong coupling between model dynamical variables, which are adapted by Newtonian relaxation, and physical parameterizations of for instance cloud convective and boundary layer processes, special care should be taken when Newtonian relaxation is used for validation of these parameterizations. Therefore, for the tropics, where dynamics play a relatively minor role, more research is needed on the use of the Newtonian relaxation technique.

The coarse resolution in chemical tracer transport models can be a problem for the calculation of cloud processes, boundary layer diffusion and convection. For this reason in the future more attention should be focussed on the dependence of parameterizations on the spatial and temporal resolution. An important development for TM3 is the recent availability of a “zoom” version of the model. With the “zoom” option, the model can run with a higher resolution for selected areas, in this way greatly enhancing the capability for comparisons between model and measurements.

With the available measurements it appears still difficult to obtain complete understanding of the sulfur cycle. The knowledge about other aerosol components and their interactions is even more immature. There is an urgent need for more measurements especially about the vertical distribution of aerosol components.

Atmospheric chemistry research can learn from the experience in the numerical weather prediction community. The standardized measurement networks, the quality control of data and the systematic confrontation of model and data within data assimilation systems could serve as an example. It is therefore recommended to expand

the global network of ozone soundings especially in the tropics where measurements are scarce, possibly under the auspices of WMO. Furthermore it is recommended to modernize the global precipitation network by including high quality chemical measurements of dissolved gases and aerosol components. Measurements of aerosol composition and optical properties, done within various research groups around the world could be better coordinated. It would be useful that more global compilations of available measurements are put together and made available to modelers.

With more satellite measurements of chemical tracers coming available in the future, chemical transport models and coupled chemistry-climate models should be used for data assimilation and chemical forecasts. In this way optimal use will be made of both model and measurements and the daily confrontation of the model with measurements will reveal shortcomings in the modeling of sources and sinks of chemical tracers. Besides satellite measurements, in situ measurements from automated networks comparable to the EMEP network and ozone sondes could be used in such a assimilation and forecast system.





# Bibliography

- Adams, P. J., J. H. Seinfeld, and D. M. Koch, Global concentrations of tropospheric sulfate, nitrate and ammonium aerosol simulated in a general circulation model, *J. Geophys. Res.*, *104*, 13,791–13,823, 1999.
- Albrecht, B. A., Aerosols, cloud microphysics, and fractional cloudiness, *Science*, *262*, 226–229, 1989.
- Andres, R. J., and A. D. Kasgnoc, A time-averaged inventory of aerial volcanic sulfur emissions, *J. Geophys. Res.*, *103*, 25,251–25,261, 1998.
- Arpe, K., The hydrological cycle in the ECMWF short range forecast, *Dyn. Atmos. Oceans*, *16*, 33, 1991.
- Balkanski, Y. J., D. J. Jacob, G. M. Gardner, W. C. Graustein, and K. K. Turekian, Transport and residence times of tropospheric aerosols inferred from a global three-dimensional simulation of  $^{210}\text{Pb}$ , *J. Geophys. Res.*, *98*, 20,573–20,586, 1993.
- Banic, C. M., W. R. Leitch, G. A. Isaac, M. D. Couture, L. I. Kleinman, S. R. Springston, and J. I. MacPherson, Transport of ozone and sulfur to the North Atlantic atmosphere during the North Atlantic Regional Experiment., *J. Geophys. Res.*, *101*, 29,091–29,104, 1996.
- Barrie, L. A., et al., A comparison of large scale atmospheric sulphate aerosol models (COSAM): overview and highlights., *Tellus B*, *submitted*, 2000.
- Beljaars, A. C. M., Numerical schemes for parameterizations, in *Proceedings of the ECMWF seminar on numerical methods in atmospheric models*, vol. II, pp. 1–42, ECMWF, 1991.
- Beljaars, A. C. M., and P. Viterbo, Role of the boundary layer in a numerical weather prediction model, in *Clear and cloudy Boundary layers*, edited by A. A. M. Holtslag and P. G. Duynkerke, pp. 85–110, Koninklijke Nederlandse Akademie van Wetenschappen, 1998.
- Benkovitz, C. M., C. M. Berkowitz, R. C. Easter, S. Nemesure, R. Wagener, and S. E. Schwartz, Sulfate over the North Atlantic and adjacent continental regions: Evaluation for October and November 1986 using a three-dimensional model driven by observation-derived meteorology, *J. Geophys. Res.*, *99*, 20,725–20,756, 1994.

- Benkovitz, C. M., M. T. Scholtz, J. Pacyna, L. Tarrason, J. Dignon, E. C. Voldner, P. A. Spiro, J. A. Logan, and T. E. Graedel, Global gridded inventories of anthropogenic emissions of sulfur and nitrogen, *J. Geophys. Res.*, *101*, 29,239–29,253, 1996.
- Brasseur, Atmospheric chemistry and global change, Oxford Univ. Press, New York, 1999.
- Brill, K., L. Uccellini, J. Manobianco, P. Kocin, and J. Homan, The use of successive dynamic initialization by nudging to simulate cyclogenesis during GALE IOP, 1, *Meteorol. Atmos. Phys.*, *45*, 15, 1991.
- Brinkop, S., and E. Roeckner, Cloud turbulence interactions: Sensitivity of a general circulation model to closure assumptions, *Tellus*, *47A*, 197, 1995.
- Burrows, J., et al., The global ozone monitoring experiment (GOME): mission concept and first scientific results, *J. Atmos. Sci.*, *56*, 151–175, 1999.
- Cariolle, D., and M. Déqué, Southern Hemisphere medium-scale waves and total ozone disturbances in a spectral general circulation model, *J. Geophys. Res.*, *91*, 10825, 1986.
- Cess et al., R. D., Intercomparison and interpretation of climate feedback processes in seventeen atmospheric general circulation models, *J. Geophys. Res.*, *95D*, 16,601, 1990.
- Chapman, S., On ozone and atomic oxygen in the upper atmosphere, *Phil. Mag.*, *10*, 369, 1930.
- Chin, M., D. J. Jacob, G. M. Gardner, M. S. Foreman-Fowler, and P. A. Spiro, A global three-dimensional model of tropospheric sulfate, *J. Geophys. Res.*, *101*, 22,869–22,889, 1996.
- Claussen, M., U. Lohmann, E. Roeckner, and U. Schulzweida, A global data set of land-surface parameters, *Tech. Rep. Report 135*, Max Planck Institut für Meteorologie, Hamburg, 1994.
- Cooke, W. F., and J. J. N. Wilson, A global black carbon aerosol model, *J. Geophys. Res.*, *101*, 19,395–19,409, 1996.
- Crutzen, P., The influence of nitrogen oxide on the atmospheric ozone content, *Quart. J. Roy. Met. Soc.*, *96*, 320, 1970.
- Crutzen, P., A discussion of the chemistry of some minor constituents in the stratosphere and troposphere, *Pure Appl. Geophys.*, *106*, 1385, 1973.
- D. J. Jacob et al., Evaluation and intercomparison of global atmospheric models using  $^{222}\text{Rn}$  and other short-lived tracers., *J. Geophys. Res.*, *102*, 5953–5970, 1997.
- Daley, R., Atmospheric data analysis, Cambridge Univ. Press, New York, 1991.
- Daley, R., and K. Puri, Four-dimensional data assimilation and the slow manifold, *Mon. Wea. Rev.*, *108*, 88, 1980.

- Dana, M. T., and J. M. Hales, Statistical aspects of the washout of polydisperse aerosols, *Atmos. Environ.*, *10*, 45–50, 1991.
- Davies, H. C., and R. Turner, Updating prediction models by dynamical relaxation: An examination of the technique, *Q. J. R. Meteorol. Soc.*, *103*, 225, 1977.
- de Laat, A. T. J., M. Zachariasse, G. J. Roelofs, P. V. Velthoven, R. R. Dickerson, K. P. Rhoads, S. J. Oltmans, and J. Lelieveld, Tropospheric O<sub>3</sub> distribution over the Indian Ocean during spring 1995 evaluated with a chemistry-climate model, *J. Geophys. Res.*, *104*, 13,881–13,893, 1999.
- Deardorff, J. W., The counter-gradient heat flux in the lower atmosphere and in the laboratory, *J. Atmos. Sci.*, *23*, 503–506, 1966.
- Dentener, F., and P. J. Crutzen, Reaction of N<sub>2</sub>O<sub>5</sub> on tropospheric aerosols: Impact on the global distributions of NO<sub>x</sub>, O<sub>3</sub> and OH, *J. Geophys. Res.*, *98*, 7149–7163, 1993.
- Dentener, F., and P. J. Crutzen, A global 3D model of the ammonia cycle, *J. Atmos. Chem.*, *19*, 331–369, 1994.
- Dentener, F., J. Feichter, and A. Jeuken, Simulation of the transport of Radon<sup>222</sup> using on-line and off-line global models at different horizontal resolutions: a detailed comparison with measurements, *Tellus*, *51B*, 573–602, 1999.
- Dibb, J. E., R. W. Talbot, K. I. Klemm, G. L. Gregory, H. B. Singh, J. D. Bradshaw, and S. T. Sandholm, Asian influence over the western north pacific during the Fall season: Inferences from Lead 210, soluble ionic species and ozone, *J. Geophys. Res.*, *101*, 1779–1792, 1996.
- Dibb, J. E., R. W. Talbot, B. L. Lefer, E. Scheuer, G. L. Gregory, H. B. Singh, J. D. Bradshaw, and S. T. Sandholm, Distribution of <sup>7</sup>Be, <sup>210</sup>Pb, and soluble aerosol-associated ionic species over the Western Pacific: PEM West B February-March 1994, *J. Geophys. Res.*, *102*, 28,287–28,302, 1997.
- Diederer, H., R. Guicherit, and J. Hollander, Visibility reduction by air pollution in the netherlands, *Atmos. Environ.*, *19*, 377–383, 1985.
- Douglas, S. G., and T. T. Warner, Utilization of VAS satellite data in the initialization of an oceanic cyclogenesis simulation, *Mon. Wea. Rev.*, *115*, 2996, 1987.
- Elbern, H., H. Schmidt, and A. Ebel, Variational data assimilation for tropospheric chemistry modeling, *J. Geophys. Res.*, *102*, 15,967, 1997.
- EMEP, Transboundary acidifying air pollution in Europe, *Tech. Rep. MSC-W Status Report 1998 - Part 1*, EMEP/MS-C-W, NMI, Oslo, Norway, 1998.
- Engelen, R. J., Satellite measurements of ozone, Ph.D. thesis, University of Utrecht, 1996.
- Eskes, H., and A. Jeuken, Assimilation of TOVS and GOME total ozone with the tm3 model, in *Chemical Data Assimilation, proceedings of the the SODA workshop held 9-10 December 1998*, pp. 77–81, KNMI, De Bilt, The Netherlands, 1999.

- Eskes, H. J., A. Pitters, P. Levelt, M. Allaart, and H. Kelder, Variational assimilation of ozone total column satellite data in a 2D lat-lon tracer-transport model, *J. Atmos. Sci.*, *56*, 3560, 1999.
- Fehsenfeld, F. C., P. Daum, W. R. Leitch, M. Trainer, D. D. Parrish, and G. Huebler, Transport and processing of O<sub>3</sub> and O<sub>3</sub> precursors over the North Atlantic: An overview, *J. Geophys. Res.*, *101*, 28,877–28,891, 1996.
- Feichter, J., and U. Lohmann, Can a relaxation technique be used to validate clouds and sulphur species in a GCM?, *Q. J. R. Meteorol. Soc.*, *125*, 1277–1294, 1999.
- Feichter, J., E. Kjellström, H. Rodhe, F. Dentener, J. Lelieveld, and G.-J. Roelofs, Simulation of the tropospheric sulfur cycle in a global climate model, *Atmosph. Environ.*, *30*, 1693–1707, 1996.
- Fischer, M., and D. J. Lary, Lagrangian four-dimensional variational data assimilation of chemical species, *Q. J. R. Meteorol. Soc.*, *121*, 1681, 1995.
- Fortuin, J. P. F., An ozone climatology based on ozone sonde measurements, *Tech. Rep. KNMI WR 96-07*, Kon. Ned. Meteorol. Inst., De Bilt, Netherlands, 1996.
- Fortuin, J. P. F., and H. Kelder, An ozone climatology based on ozonesonde and satellite measurements, *J. Geophys. Res.*, *103*, 31,709–31,734, 1998.
- Fouquart, Y., and B. Bonnel, Computations of solar heating of the earth's atmosphere: A new parameterization, *Beitr. Phys. Atmos.*, *53*, 35, 1980.
- Ganzeveld, L., J. Lelieveld, and G.-J. Roelofs, Dry deposition parametrization of sulfur oxides in a chemistry and general circulation model, *J. Geophys. Res.*, *103*, 5679–5694, 1998.
- Gery, M. W., G. Z. Whitten, J. P. Killus, and M. Dodge, A photo-chemical kinetics mechanism for urban and regional scale computer modeling, *J. Geophys. Res.*, *94*, 925–956, 1989.
- Gesell, T. F., Background atmospheric <sup>222</sup>Rn concentrations outdoors and indoors: a review, *Health Phys.*, *45*, 289–302, 1983.
- Gong, S. L., L. A. Barrie, J. Prospero, D. L. Savoie, G. P. Ayers, J.-P. Blanchet, and L. Spacek, Modeling seasalt aerosol in the atmosphere, part 2: Atmospheric concentrations and fluxes, *J. Geophys. Res.*, *102*, 3819–3830, 1997.
- Griffin, R. J., D. R. Cocker, R. C. Flagan, and J. H. Seinfeld, Organic aerosol formation from the oxidation of biogenic hydrocarbons, *J. Geophys. Res.*, *104*, 3555–3567, 1999.
- Guelle, W., Y. J. Balkanski, J. E. Dibb, M. Schulz, and F. Dulac, Wet deposition in a global size-dependent aerosol transport model: 1. comparison of a 1 year <sup>210</sup>Pb simulation with ground measurements, *J. Geophys. Res.*, *103*, 11,429–11,445, 1997a.
- Guelle, W., Y. J. Balkanski, J. E. Dibb, M. Schulz, and F. Dulac, Wet deposition in a global size-dependent aerosol transport model: 2. influence of the scavenging scheme on <sup>210</sup>Pb vertical profiles, surface concentrations and deposition, *J. Geophys. Res.*, *103*, 28,875–28,891, 1997b.

- Haywood, J. M., R. J. Stouffer, R. T. Wetherald, S. Manabe, and V. Ramaswamy, Transient response of a coupled model to estimated changes in greenhouse gas and sulfate concentrations, *Geophys. Res. Lett.*, *24*, 1335–1338, 1997.
- Heimann, M., The global atmospheric tracer model tm2, *Tech. Rep. Technical Report 10*, Deutsches Klima Rechenzentrum, Modellbetreuungsgruppe, Hamburg, 1995.
- Heimann, M., and C. D. Keeling, A three-dimensional model of atmospheric CO<sub>2</sub> transport based on observed winds, 2, Model description and simulated tracer experiments, in *Aspects of climate variability in the Pacific and Western Americas*, *Geophys. Monogr. Ser.*, edited by D. H. Peterson, vol. 55, pp. 237–275, AGU, 1989.
- Hein, R., P. J. Crutzen, and M. Heimann, An inverse modeling approach to investigate the global atmospheric methane cycle, *Global Biogeochem. Cycles*, *11*, 43, 1997.
- Herman, J. R., and E. A. Celarier, Earth surface reflectivity climatology at 340–380 nm from TOMS data, *J. Geophys. Res.*, *102*, 28,003–28,011, 1997.
- Herman, J. R., P. K. Barthia, O. Torres, C. Hsu, C. Seftor, and E. A. Celarier, Global distributions of uv-absorbing aerosols from nimbus 7/toms data, *J. Geophys. Res.*, *102*, 16,911–16,922, 1997.
- Heymsfield, A. J., and L. J. Donner, A scheme for parametrizing ice-cloud water content in general circulation models, *J. Atmos. Sci.*, *47*, 1865–1877, 1990.
- Hoell, J. M., D. D. Davis, S. C. Liu, R. E. Newell, H. Akimoto, R. J. McNeal, and R. J. Bendura, The Pacific Exploratory Mission-West Phase B: February-March, 1994, *J. Geophys. Res.*, *102*, 28,223–28,239, 1997.
- Hoke, J. E., and A. Anthes, The initialization of numerical models by a dynamic-initialization technique, *Mon. Wea. Rev.*, *104*, 1551, 1976.
- Holopainen, E., Recent estimates of diabatic forcing on the planetary scale: A review, *Tech. rep.*, Eur. Cent. Meteorol. Weather Forecasting, Reading, England, 1987.
- Holtlag, A. A. M., and B. A. Boville, Local versus nonlocal boundary-layer diffusion in a global climate model, *J. Climate*, *6*, 1825–1842, 1993.
- Holtlag, A. A. M., and C. Moeng, Eddy diffusivity and countergradient transport in the convective atmospheric boundary layer, *J. Atmos. Sci.*, *48*, 1690–1698, 1991.
- Houweling, S., F. Dentener, and J. Lelieveld, The impact of nonmethane hydrocarbon compounds on tropospheric chemistry, *J. Geophys. Res.*, *103*, 10,673–10,696, 1998.
- IPCC, IPCC second scientific assessment of climate change, p. 572, Cambridge UP, Cambridge, UK, 1995.
- Issac, G. A., Vertical profiles and horizontal transport of atmospheric aerosols and trace gases over central Ontario, *J. Geophys. Res.*, *103*, 22,015–22,037, 1998.
- Jaenicke, R., Landolt-Börnstein Zhalenwerte und Funktionen aus Naturwissenschaften und Technik. Band 4: Meteorologie, Teilband B: Physikalische und chemische Eigenschaften der Luft, pp. 391–457, Springer, Berlin, 1988.

- Jeuken, A., P. Siegmund, L. Heijboer, J. Feichter, and L. Bengtsson, On the potential of assimilating meteorological analyses in a global climate model for the purpose of model validation, *J. Geophys. Res.*, *101*, 16939–16950, 1996.
- Johnston, H. S., Reduction of stratospheric ozone by nitrogen ozone catalysts from supersonic transport exhausts, *Science*, *173*, 517, 1971.
- Kalman, R. E., A new approach to linear filtering and prediction problems, *Trans. ASME J. Basic Eng.*, *82*, 35–45, 1960.
- Kanakidou, M., K. Tsigaridis, F. Dentener, and P. Crutzen, Human activity enhances the formation of organic aerosols by biogenic hydrocarbon oxidation., *J. Geophys. Res.*, *accepted*, 2000.
- Kasibhatla, P., W. L. Chameides, and J. S. John, A three-dimensional global model investigation of seasonal variations in the atmospheric burden of anthropogenic sulfate aerosols, *J. Geophys. Res.*, *102*, 3737–3759, 1997.
- Kaufman, Y. J., Remote sensing of direct and indirect aerosol forcing, in *Aerosol forcing of Climate*, edited by R. J. Charlston and J. Heintzenberg, pp. 297–332, John Wiley, 1995.
- Kettle, A. J., M. O. Andreae, and many others, A global database of sea surface dimethylsulfide (DMS) measurements and a procedure to predict sea surface DMS as a function of latitude, longitude and month, *Global Biogeochem. cycles*, *13*, 399–444, 1999.
- Khattatov, B. V., J. C. Gille, L. V. Lyjak, G. P. Brasseur, V. L. Dvortsov, A. E. Roche, and J. W. Waters, Assimilation of photochemically active species and a case analysis of uars data, *J. Geophys. Res.*, *104*, 18,715–18,737, 1999.
- Kiehl, J. T., and B. P. Briegleb, The relative roles of sulfate aerosols and greenhouse gases in climate forcing, *Science*, *260*, 311–314, 1993.
- Koch, D., D. Jacob, I. Tegen, D. Rind, and M. Chin, Tropospheric sulfur simulation and sulfate direct radiative forcing in the Goddard Institute for Space Studies GCM., *J. Geophys. Res.*, *104*, 23,799–23,822, 1999.
- Krishnamurti, T. N., H. S. Bedi, W. Heckley, and K. Ingles, Reduction of the spin-up time for evaporation and precipitation in a spectral model, *Mon. Wea. Rev.*, *116*, 907, 1988.
- Krishnamurti, T. N., J. Xue, H. Bedi, K. Ingles, and D. Oosterhof, Physical initialization for numerical weather prediction over the tropics, *Tellus*, *43AB*, 53, 1991.
- Kritz, M. A., S. W. Rosner, and D. Z. Stockwell, Validation of an off-line 3-d chemical transport model using observed radon profiles - part i: Observations, *J. Geophys. Res.*, *103*, 8425–8432, 1997.
- Krol, M., and M. van Weele, Implication of variation of photodissociation rates for global atmospheric chemistry, *Atmosph. Environ.*, *31*, 1257–1273, 1997.

- Kuo, Y. H., and Y. R. Guo, Dynamic initialization using observations from a network of profilers and its impact on short-range numerical weather prediction, *Mon. Wea. Rev.*, *117*, 1975, 1989.
- Langner, J., and H. Rodhe, A global three-dimensional model of the tropospheric sulfur cycle, *J. Atm. Chem.*, *13*, 225–263, 1991.
- Larsen, R. J., C. G. Sanderson, and J. Kada, EML surface air sampling program 1990-1993 data, *Tech. Rep. EML-572*, Environ. Meas. Lab., US Dep. of Energy, 1995.
- Lary, D. J., M. Chipperfield, J. A. Pyle, W. A. Norton, and L. P. Riishøjgaard, Three-dimensional tracer initialization and general diagnostics using equivalent pv latitude-potential-temperature coordinates, *Q. J. R. Meteorol. Soc.*, *121*, 187, 1995.
- Leaitch, W. R., et al., Physical and chemical observations in marine stratus during 1993 NARE: Factors controlling cloud droplet number concentrations., *J. Geophys. Res.*, *101*, 29,043–29,060, 1996.
- Lee, H. N., and R. J. Larsen, Vertical diffusion in the lower atmosphere using aircraft measurements of  $^{222}\text{Rn}$ , *J. Appl. Meteorol.*, *36*, 1262–1270, 1997.
- Lefèvre, F., D. Cariolle, S. Muller, and F. Karcher, Total ozone from TIROS operational vertical sounder during the formation of the 1987 ozone hole, *J. Geophys. Res.*, *96*, 12,893, 1991.
- Lelieveld, J., and P. J. Crutzen, The role of clouds in tropospheric photochemistry, *J. Atmos. Chem.*, *12*, 229–267, 1991.
- Lelieveld, J., and F. Dentener, What's controlling tropospheric ozone, *J. Geophys. Res.*, *105*, 3531, 2000.
- Levelt, P. F., M. A. F. Allaart, and H. M. Kelder, On the assimilation of total-ozone satellite data, *Ann. Geophys.*, *14*, 1111, 1996.
- Liousse, C., J. E. Pennner, C. Chuang, J. J. Walton, H. Eddleman, and H. Cachier, A global three-dimensional model study of carbonaceous aerosols, *J. Geophys. Res.*, *101*, 19,411–19,432, 1996.
- Liss, P., and L. Merlivat, Air-sea gas exchange rates: Introduction and synthesis, in *The Role of Sea-Air Exchange in Geochemical Cycling*, edited by P. Menard, pp. 113–127, Reidel, Dordrecht, 1986.
- Lohmann, U., et al., Comparison of the vertical distribution of sulfur species from models participated in the COSAM exercise with observations, *J. Geophys. Res.*, *submitted*, 1999.
- Lorenc, A. C., Optimal nonlinear objective analysis, *Q. J. R. Meteorol. Soc.*, *114*, 205, 1988.
- Louis, J. F., A parametric model of vertical eddy fluxes in the atmosphere, *Boundary-Layer Meteorol.*, *17*, 187–202, 1979.



- Louis, J. F., M. Tiedtke, and J. F. Geleyn, A short history of PBL parameterization at ECMWF, in *Proceedings of the ECMWF workshop on boundary-layer parameterization*, pp. 59–79, 1982.
- Lyne, W. H., R. Swinbank, and T. N. Birch, A data assimilation experiment and the global circulation during fgge special observing periods, *Q. J. R. Meteorol. Soc.*, *108*, 575, 1982.
- Mahowald, N. M., P. J. Rasch, and R. G. Prinn, Cumulus parametrizations in chemical transport models, *J. Geophys. Res.*, *100*, 26,173–26,189, 1995.
- Mason, B. J., *The physics of clouds*, p. 671, Clarendon, Oxford, 1971.
- Metzger, S., Gas-aerosol equilibria, Ph.D. thesis, University of Utrecht, 2000.
- Metzger, S., F. Dentener, and J. Lelieveld, Aerosol multiphase chemistry - a parameterization for global modeling, *Tech. Rep. Internal Report No. 99-12*, Institute for Marine and Atmospheric Research Utrecht (IMAU), Princetonplein 5, NL-3584 CC Utrecht, Netherlands, 1999a.
- Metzger, S., F. Dentener, and J. Lelieveld, Gas-aerosol equilibrium parameterization for atmospheric chemistry models, *J. Geophys. Res.*, *submitted*, 1999b.
- Mitchell, J. F. B., T. J. Johns, J. M. Gregory, and S. F. B. Tett, Transient climate response to increasing sulphate aerosol and greenhouse gases, *Nature*, *376*, 501–504, 1995.
- Morcrette, J.-J., Radiation and cloud radiative properties in the ECMWF operational weather forecast model, *J. Geophys. Res.*, *96D*, 9121, 1991.
- Nenes, A., C. Pilinis, and S. N. Pandis, Isorropia: A new thermodynamic model for multiphase multicomponent inorganic aerosols, *Aquatic Geochemistry*, *4*, 123–152, 1998.
- Newell, R. E., J. W. Kidson, D. G. Vincent, and G. J. Boer, *The general circulation of the tropical atmosphere and interactions with extra tropical latitudes*, vol. 2, MIT press, 1974.
- Olivier, J., Description of EDGAR version 2.0, *Tech. Rep. 771060002*, RIVM, Bilthoven, Netherlands, 1996.
- Olson, J., J. A. Watts, and L. J. Allison, Carbon inlive vegetation of major world ecosystems, *Tech. Rep. ORNL-5862*, Oak Ridge National Laboratory, Oak Ridge, Tennessee, 1983.
- Parrish, D. F., and J. Derber, The national meteorological center's spectral statistical-interpolation analysis system, *Mon. Wea. Rev.*, *120*, 1747, 1992.
- Pham, M., J.-F. Müller, G. P. Brasseur, C. Granier, and G. Mégie, A three-dimensional study of the tropospheric sulfur cycle, *J. Geophys. Res.*, *100*, 26,061–26,092, 1995.

- Planet, W. G., D. Crosby, J. Lienisch, and M. Hill, Determination of total ozone amount from TIROS radiance measurements, *J. Appl. Meteorol.*, *23*, 308, 1984.
- Potukuchi, S., and A. S. Wexler, Predicting vapor pressures using neural networks, *Atmos. Environ.*, *31*, 741–753, 1997.
- Preiss, N., M.-A. Mélières, and M. Pourchet, A compilation of data on lead 210 concentration in surface air and fluxes at the air-surface and water-sediment interfaces, *J. Geophys. Res.*, *101*, 28,847–28,862, 1996.
- Ramamurthy, M. K., and F. H. Carr, Four-dimensional data assimilation in the monsoon region, i: Experiments with wind data, *Mon. Wea. Rev.*, *115*, 1679, 1987.
- Rasch, P. J., and D. L. Williamson, Computational aspects of moisture transport in global models of the atmosphere, *Q. J. R. Meteorol. Soc.*, *116*, 1071, 1990.
- Rasch, P. J., N. M. Mahowald, and B. E. Eaton, Representations of transport, convection, and the hydrological cycle in chemical transport models: Implications for the modeling of shortlived and soluble species, *J. Geophys. Res.*, *102*, 28,127–28,138, 1997.
- Regener, E., Ozonschicht und Atmosphärische Turbulenz, *Ber. Deutch. Wetterdien. US-Zone*, *11*, 45, 1949.
- Rehfeld, S., and M. Heimann, Three dimensional atmospheric transport simulation of the radioactive tracers  $^{210}\text{Pb}$ ,  $^7\text{Be}$ ,  $^{10}\text{Be}$ , and  $^{90}\text{Sr}$ , *J. Geophys. Res.*, *100*, 26,141–26,161, 1995.
- Riishøjgaard, L. P., A GCM simulation of the Northern Hemisphere ozone field in early february 1990, using satellite total ozone for model initialization, *Ann. Geophys.*, *10*, 54, 1992.
- Riishøjgaard, L. P., On four-dimensional variational assimilation of ozone data in weather-prediction models, *Q. J. R. Meteorol. Soc.*, *122*, 1545, 1996.
- Robles-Gonzalez, C., J. P. Veefkind, and G. de Leeuw, Aerosol optical depth over Europe in august 1997, *Geophys. Res. Let.*, *accepted for publication*, 2000.
- Roeckner, E., L. Bengtsson, J. Feichter, J. Lelieveld, and H. Rodhe, Transient climate change simulations with a coupled atmosphere ocean GCM including the tropospheric sulfur cycle, *Tech. Rep. MPI-report 264*, Max-Planck Institute for Meteorology, Hamburg, 1998.
- Roeckner, E., et al., Simulation of the present day climate with the ECHAM model: Impact of model physics and resolution, *Tech. Rep. MPI-report 93*, Max-Planck Institute for Meteorology, Hamburg, 1993.
- Roelofs, G.-J., and J. Lelieveld, Distribution and budget of  $\text{O}_3$  in the troposphere calculated with a chemistry general circulation model, *J. Geophys. Res.*, *100*, 20,983–20,998, 1995.

- Roelofs, G.-J., J. Lelieveld, and L. Ganzeveld, Simulation of global sulfate distribution and the influence on effective cloud drop radii with a coupled photochemistry-sulfur cycle model, *Tellus*, 50B, 224–242, 1998.
- Roelofs, G.-J., et al., Analysis of regional budgets of sulfur species modeled for the COSAM exercise, *Tellus B*, *submitted*, 2000.
- Rudolf, B., Die Bestimmung der zeitlich-räumlichen Struktur des globalen Niederschlags, *Tech. Rep. 196*, Ber. Deutsch. Wetterdien., Offenbach, Germany, 1995.
- Russell, and A. Lerner, A finite difference scheme for the tracer transport equation, *J. Appl. Meteorol.*, 20, 1483, 1981.
- Sato, M., J. E. Hansen, M. P. McCormick, and J. B. Pollack, Stratospheric aerosol optical depths, 1850-1990., *J. Geophys. Res.*, 98, 22,987–22,994, 1993.
- Schwartz, S. E., The whitehouse effect- shortwave radiative forcing of climate by anthropogenic aerosols, an overview, *J. Aerosol Sci.*, 27, 359–382, 1996.
- Seinfeld, J. H., Atmospheric chemistry and physics of air pollution, John Wiley and Sons, New York, 1986.
- Siegmund, P. C., Cloud diabatic forcing of the atmosphere, estimated from simultaneous ECMWF diabatic heating and ISCCP cloud amount observations, *J. Clim.*, 6, 2419, 1993.
- Simmons, A. J., Orography and the development of the ECMWF forecast model, in *Proceedings of 1986 ECMWF Seminar on Observation, Theory and Modelling of orographic effects, vol. 2*, Reading, England, 1987.
- Spiro, P. A., D. J. Jacob, and J. A. Logan, Global inventory of sulfur emissions with  $1^\circ \times 1^\circ$  resolution, *J. Geophys. Res.*, 97, 6023–6036, 1992.
- Stauffer, and J.-W. Bao, Optimal determination of nudging coefficients using the adjoint equations, *Tellus*, 45A, 358–369, 1993.
- Stauffer, and N. Seaman, Use of four-dimensional data assimilation in a limited area mesoscale model part ii: Effects of data assimilation within the planetary boundary layer, *Mon. Wea. Rev.*, 119, 734, 1990.
- Stoffelen, A., and H. Eskes, Satellite ozone data assimilation, *Tech. rep.*, European Union project, De Bilt, The Netherlands, 1999.
- Sundquist, H., A parameterization scheme for non-convective condensation including prediction of cloud water content, *Q. J. R. Meteorol. Soc.*, 104, 677, 1978.
- Sundquist, H., E. Berge, and J. E. Kristjansson, Condensation and cloud parametrization studies with a mesoscale numerical prediction model, *Mon. Wea. Rev.*, 117, 1641–1657, 1989.
- Sutton, R. T., H. Maclean, R. Swinbank, A. O'Neill, and F. Taylor, High-resolution stratospheric tracer fields estimated from satellite observations using lagrangian trajectory calculations, *J. Atmos. Sci.*, 51, 2995, 1994.

- Tanré, D., M. Herman, and Y. J. Kaufman, Information on aerosol size distribution contained in solar reflected radiances, *J. Geophys. Res.*, *101*, 19,043–19,060, 1996.
- Tegen, I., and I. Fung, Modeling of mineral dust in the atmosphere: Sources, transport and optical thickness, *J. Geophys. Res.*, *99*, 22,897–22,914, 1994.
- Ten Brink, H. M., C. Kruisz, G. P. A. Kos, and A. Berner, Composition of the light-scattering aerosol in the Netherlands, *Atmos. Environ.*, *31*, 3955–3962, 1996a.
- Ten Brink, H. M., J. P. Veefkind, A. Waaijers-IJpelaan, and J. C. H. van der Hage, Aerosol light-scattering in the Netherlands, *Atmos. Environ.*, *30*, 4251–4261, 1996b.
- Tiedtke, M., A comprehensive mass flux scheme for cumulus parametrization in large scale models, *Mon. Wea. Rev.*, *117*, 1641, 1989.
- Tiedtke, M., Representation of clouds in large-scale models, *Mon. Wea. Rev.*, *121*, 3040–3061, 1993.
- Turekian, K. K., Y. Nozaki, and L. Benninger, Geochemistry of atmospheric radon and radon products, *Ann. Rev. Earth Planet. Sci.*, *5*, 227–255, 1977.
- Van Aardenne, J. A., F. J. Dentener, C. G. M. K. Goldewijk, J. Lelieveld, and J. G. J. Olivier, A high resolution data set of historical anthropogenic trace gas emissions for the period 1890-1990, *Global Biogeochem. Cycles*, *submitted*, 1999.
- Van der A, R. J., R. F. van Oss, and H. M. Kelder, Ozone profile retrieval from gome data, in *Satellite remote sensing of clouds and the atmosphere II*, edited by J. E. Russell, vol. 3495, pp. 77–81, SPIE, 1998.
- Van der Hurk, B., P. Viterbo, A. Beljaars, and A. Betts, Offline validation of the ERA40 surface scheme, *Tech. Rep. Tech. memo 295*, ECMWF, 1999.
- van Dorland, R., Radiation and climate, Ph.D. thesis, University of Utrecht, 1999.
- Veefkind, J. P., Aerosol satellite remote sensing, Ph.D. thesis, University of Utrecht, 1999.
- Veefkind, J. P., and G. de Leeuw, A new algorithm to determine the spectral aerosol optical depth from satellite radiometer measurements, *J. Aerosol Sci.*, *29*, 1237–1248, 1998.
- Veefkind, J. P., J. C. H. van der Hage, and H. M. Ten Brink, Nephelometer derived and directly measured aerosol optical depth of the atmospheric boundary layer, *Atmos. Res.*, *41*, 217–228, 1996.
- Veefkind, J. P., G. de Leeuw, and P. A. Durkee, Retrieval of aerosol optical depth over land using two-angle view satellite radiometry during TARFOX, *Geophys. Res. Lett.*, *25*, 3135–3138, 1998.
- Velders, G. J. M., L. C. Heijboer, and H. Kelder, The simulation of transport of aircraft emissions by a three-dimensional global model, *Ann. Geophysicae*, *12*, 385–393, 1994.

- Velthoven, P. F. J. V., and H. Kelder, Estimates of stratosphere-troposphere exchange: sensitivity to model formulation and horizontal resolution, *J. Geophys. Res.*, *101*, 1429, 1996.
- Vogelezang, D. H. P., Evaluation and model impacts of alternative boundary-layer height formulations, *Boundary-Layer Meteorol.*, *81*, 245–269, 1996.
- Wang, C.-H., and W. John, Characteristics of the Berner impactor for sampling inorganic ions, *Aerosol Science and Technology*, *8*, 157–172, 1988.
- Wang, K.-Y., J. A. Pyle, M. G. Sanderson, and C. Bridgeman, Implementation of a convective atmospheric boundary layer scheme in a tropospheric chemistry transport model, *J. Geophys. Res.*, *104*, 23,729–23,745, 1999.
- Wang, W. C., D. J. Wuebbles, W. M. Washington, R. G. Isaacs, and G. Molnar, Trace gases and other potential perturbations to global climate, *Rev. Geophys.*, *24*, 110, 1986.
- Wauben, W. M. F., P. V. Velthoven, and H. Kelder, A 3D chemistry transport model study of changes in atmospheric ozone due to aircraft NO<sub>x</sub> emissions., *Atmos. Environ.*, *31*, 1819–1836, 1997.
- Wauben, W. M. F., J. Fortuin, P. V. Velthoven, and H. Kelder, Comparison of modeled ozone distributions with sonde and satellite observations, *J. Geophys. Res.*, *103*, 3511, 1998.
- Xing, L., and W. L. Chameides, Model simulations of rainout and washout from a warm stratiform cloud, *J. Atmos. Chem.*, *10*, 1–26, 1990.
- Zaucker, F., P. H. Daum, U. Wetterauer, C. Berkowitz, B. Kromer, and W. Broecker, <sup>222</sup>Rn measurements during the nare intensive, *J. Geophys. Res.*, *101*, 29,149–29,164, 1996.
- Zou, X., I. Navon, and F. Ledimet, An optimal nudging data assimilation scheme using parameter estimation, *Q. J. R. Meteorol. Soc.*, *118*, 1163, 1992.

# Samenvatting

Ozon en aerosolen zijn atmosferische bestanddelen die belangrijk zijn voor de stralingsbalans en de chemie van de atmosfeer. Antropogene emissies veroorzaken waarneembare veranderingen in de hoeveelheid en verdeling van ozon en aerosolen. Om de invloed van deze veranderingen op de samenstelling van de atmosfeer en op het klimaat te berekenen, wordt gebruik gemaakt van mondiale chemie- en klimaatmodellen. Met het oog op de waarde van voorspellingen en het belang voor beleidsmakers, is het vereist dat modeluitkomsten uitvoerig geverifieerd worden met metingen. De vergelijking tussen modelresultaten en metingen is dan ook de belangrijkste doelstelling in dit proefschrift. Door het model te confronteren met metingen kunnen zwakke onderdelen aan het licht komen en kan het effect van modelveranderingen worden bepaald. Data-assimilatie gaat een stap verder dan het direct vergelijken van model en metingen. Data-assimilatie is een techniek waarmee de meest waarschijnlijke ruimtelijke verdeling of toestand van een gegeven grootte kan worden bepaald op basis van metingen en de fysische vergelijkingen beschreven in een model. In een data-assimilatiesysteem wordt een gewogen gemiddelde bepaald tussen modelvoorspellingen en metingen binnen een bepaald tijdsbestek waarbij rekening gehouden wordt met foutenschattingen voor model en meting. Op deze manier kan uit onregelmatig verdeelde metingen met het model een gelijkmatige verdeling in ruimte en tijd berekend worden. Doordat in een model verschillende variabelen aan elkaar zijn gekoppeld kan assimilatie van metingen van een grootte er ook voor zorgen dat de beschrijving van andere modelgrootheden verbeterd wordt.

In dit proefschrift wordt gebruik gemaakt van twee mondiale modellen. Het ECHAM model en het TM3 model. ECHAM is het klimaatmodel van het Max Planck Instituut voor Meteorologie in Hamburg en is een van de meest geavanceerde globale circulatie modellen (GCM) ter wereld. Het model is gebaseerd op het weersverwachtingsmodel van het Europees Centrum voor de Weersverwachting op de Middellange Termijn (ECMWF). Het ECHAM model wordt gebruikt om de invloed van natuurlijke en menselijke factoren op het klimaat te berekenen. Het chemisch transport model (CTM) TM3 is geschikt om de samenstelling van de atmosfeer en het verloop hiervan in de tijd te berekenen. De meteorologische velden om onder andere het transport, het oplossen in wolken en de verwijdering door neerslag van chemische componenten te kunnen berekenen worden voorgeschreven en zijn afkomstig van het ECMWF.

Een klimaatmodel als ECHAM berekent een gemiddeld weer, oftewel klimaat, dat representatief is voor periodes van meerdere jaren. Om zulke klimatologische resultaten te verifiëren, zijn waarnemingen nodig over eveneens vele jaren. Voor veel belangrijke modelvariabelen zoals wolkeneigenschappen of voor chemische componenten, bestaan zulke waarnemingen niet. In hoofdstuk 2 van dit proefschrift wordt

daarom een data-assimilatie methode, Newtoniaanse relaxatie genaamd, gebruikt om het ECHAM model bij te sturen met pseudo waarnemingen van wind, temperatuur en luchtdruk. Als pseudo waarnemingen dienen analyses van het ECMWF model, die een van de beste beschrijvingen geven van de toestand van de atmosfeer. Bij Newtoniaanse relaxatie wordt de sterkte van de modelbijsturing bepaald door de waarde van tijdsconstanten, oftewel relaxatieconstanten. Het blijkt dat als tijdsconstanten van de orde van enkele uren tot dagen gebruikt worden, het ECHAM model goed in staat is om de waargenomen toestand van de atmosfeer te simuleren. Hoge correlaties met ECMWF analyses worden vooral in gebieden buiten de tropen gevonden. Bij een te sterke relaxatie blijkt de verticale uitwisseling in de grenslaag en het verticale transport in convectieve bewolking sterk af te nemen.

Omdat ozon een belangrijke rol speelt in de chemie en stralingshuishouding van de atmosfeer, wordt ozon veelvuldig gemeten door satellietinstrumenten. In hoofdstuk 3 wordt een data-assimilatie methode gepresenteerd om metingen van ozonkolommen van de TIROS Operational Vertical Sounder (TOVS) te assimileren in het 3-dimensionale chemie transport model TM3. Een versie van TM3 met sterk vereenvoudigde stratosferische ozonchemie is hiervoor gebruikt. Om 2-dimensionale metingen te assimileren in een 3-dimensionaal model moeten verschillen tussen geobserveerde en gemodelleerde ozonkolommen verdeeld worden over de verticale modellagen van TM3. Drie verschillende gewichtsfuncties gebaseerd op de verticale massaverdeling, de variantie in de tijd, en covarianties van voorspelfouten in ozon zijn hiervoor gebruikt. Uit een vergelijking met metingen van een onafhankelijk satellietinstrument kan geconcludeerd worden dat de analyse van model en TOVS metingen samen beter is dan zowel de oorspronkelijke model resultaten als de oorspronkelijke metingen. De vergelijking met metingen van ozonsondes leert dat het TM3 model de dynamische structuren in ozon goed representeert. Behalve dat TM3 met data-assimilatie de ozonverdeling goed weergeeft, verschaft het inzicht in de kwaliteit van het model met betrekking tot de simulatie van de chemie en het transport van ozon. Systematische verschillen tussen model en metingen, aan het licht gekomen door de data-assimilatie, wijzen er op dat de verticale model resolutie in de stratosfeer te grof is en dat een meer uitvoerige ozon chemie nodig is om ozon profielen beter te kunnen simuleren.

Aerosolen kaatsen zonlicht terug en hebben hierdoor een significant koelend effect op de atmosfeer. De onzekerheden in de schattingen van de hoeveelheid straling die wordt teruggekaatst zijn echter groot, veel groter bijvoorbeeld dan de onzekerheden in de rol van  $\text{CO}_2$ . Het eerste probleem vormt de samenstelling van de aerosolen. Sulfaat, ammonium en in mindere mate nitraat zijn belangrijke bestanddelen van atmosferisch aerosol. Deze componenten en hun bronnen en putten zijn gemodelleerd in TM3. De grote variabiliteit van aerosolen en gassen die leiden tot aerosolvorming stelt hoge eisen aan het model. Voor gassen met een korte levensduur zoals zwavel dioxide en ammoniak, die grote en heterogene bronnen in de grenslaag hebben, moet de verticale menging nauwkeurig gemodelleerd worden. Voor oplosbare componenten en aerosolen die dienen als condensatiekernen, moet uitregening goed gesimuleerd worden in het model. De bestaande model beschrijving van verticale menging in de grenslaag en uitregening was niet adequaat genoeg om toepassing op aerosolen toe te staan. Daarom worden in hoofdstuk 4 veranderingen in deze modelonderdelen voorgesteld, toegepast en getoetst.

De kleinschalige verticale menging van een component wordt in modellen meestal

beschreven als het produkt van de verticale gradient in deze component en een diffusiecoëfficiënt. In de oude TM3 versie werd de diffusiecoëfficiënt berekend als een functie van de lokale verticale wind gradient, een typische lengte schaal voor turbulente wervels en de lokale atmosferische stabiliteit. Uit modelsimulaties bleek dat deze methode leidde tot een onderschatting van de verticale menging. Daarom is in TM3 een nieuwe methode gebruikt, vergelijkbaar met de methode die gehanteerd wordt in het ECMWF weersverwachtingsmodel. Hierbij wordt voor stabiele omstandigheden een lokale diffusiecoëfficiënt berekend op basis van lokale grootheden. Maar in vergelijking met het oude model is de stabiliteits afhankelijke functie zo veranderd dat er meer uitwisseling plaatsvindt. Voor onstabiele omstandigheden is een fundamenteel andere benadering gekozen. Niet de lokale gradienten in wind en temperatuur bepalen de menging, maar de grootschalige wervels die gegenereerd worden aan het oppervlak en zich kunnen uitstrekken over de gehele grenslaagdiepte. In deze aanpak wordt eerst een grenslaaghoogte berekend en vervolgens afhankelijk van deze hoogte een profiel van diffusiecoëfficiënten berekend. Ook de tijdstap in de verticale diffusie in TM3 is teruggebracht van 6 tot 3 uur waardoor een betere tijdsoplossing van grenslaaggroei en menging mogelijk is.

Het niet-reactieve sporegas radon is gebruikt om de invloed van het nieuwe verticale diffusie schema op het vertikaal transport in TM3 te testen. Model simulaties met het oude en het nieuwe schema zijn vergeleken met metingen. Het blijkt dat de dagelijkse gang in radon concentraties aan het oppervlak veel beter beschreven wordt met het nieuwe schema. Ook absolute waarden van de concentraties stemmen beter overeen met de waarnemingen, ofschoon ze nog steeds enigszins worden overschat dichtbij het oppervlak. De resultaten suggereren ook dat de resolutie waarop de diffusie coëfficiënten worden berekend van invloed is op uiteindelijke menging in het model vooral in stabiele omstandigheden. Daarom wordt aanbevolen om de coëfficiënten te berekenen op een resolutie die zo dicht mogelijk ligt bij de oorspronkelijke resolutie van het ECMWF model.

In plaats van een klimatologie te gebruiken voor de verticale verdeling van de neerslagvorming, zoals in de oude methode, wordt in de nieuwe methode de vorming van neerslag berekend in TM3 zelf, gebruikmakend van wolkenijs- en wolkenwaterconcentraties uit het ECMWF model. Op deze manier wordt een 3-dimensionale verdeling van de neerslag verkregen die toegepast kan worden om gassen en aerosol te verwijderen via synoptische neerslag. De verwijdering van stoffen in convectieve wolken is geparameteriseerd als een functie van de verticale “updraft” luchtmassafflux. Op deze manier kan snelle uitregening die zich uitstrekt over meerdere verticale lagen in onweerswolken beter worden beschreven. Het radioactieve vervalprodukt van radon, lood, is gebruikt om dit nieuwe schema te testen. Omdat lood zich in de atmosfeer hecht aan aerosol deeltjes en geen andere verliesprocessen kent dan de verwijdering door droge en natte depositie is het geschikt om de verwijdering van aerosolen door neerslag te onderzoeken. Modelsimulaties met het oude en nieuwe natte verwijderingsschema zijn vergeleken met metingen van lood. Het blijkt dat met het nieuwe schema lood veel efficiënter uitregent en dat dit leidt tot een veel betere overeenstemming met de metingen. In de winter lijkt echter de uitregening op hoge breedtegraden te worden overschat.

De veranderingen in verticale diffusie en verwijdering door neerslag zijn ook geïmplementeerd in een versie van TM3 met volledige troposferische chemie. Zoals in hoofdstuk 5 beschreven wordt, zijn aan het model de chemie van zwavel en geredu-



ceerde stikstof componenten toegevoegd, alsmede een thermodynamische aerosol parameterisatie, die de verdeling van nitraat beschrijft tussen gas en aerosol fase. Met deze modelversie zijn verscheidene simulaties uitgevoerd en de uitkomsten hiervan zijn vergeleken met metingen uitgevoerd met verschillende methodes en op verschillende tijdschalen. De voornaamste conclusie uit deze vergelijking luidt dat de sulfaataerosol concentratie goed wordt gesimuleerd door het model, zowel in absolute waarde als wat betreft de dagelijkse en jaarlijkse gang. Emissies van zwaveldioxide blijken de meest onzekere factor in de modellering van de zwavelcyclus. De som van alle emissies in een andere veelgebruikte emissiedataset voor Europa blijkt een factor twee kleiner te zijn dan in de dataset die standaard wordt gebruikt in TM3. Door deze andere dataset te gebruiken, blijken ook de zwaveldioxide concentraties aan het oppervlak in Europa met een factor twee af te nemen. Echter, zelfs met veel lagere emissies worden de oppervlakte concentraties nog steeds overschat. Er moet dus meer aandacht geschonken worden aan het nauwkeurig schatten van emissies. Zeer waarschijnlijk duiden de te hoge oppervlakte concentraties van zwaveldioxide op een meer fundamenteel probleem in TM3 en veel andere globale zwavelmodellen. In de winter leiden te hoge zwaveldioxide concentraties ook nog eens tot te lage sulfaat niveaus. Mede op basis van de resultaten voor radon, is de conclusie gerechtvaardigd dat een toename van de verticale menging onder stabiele omstandigheden, eventueel in combinatie met een extra oxidatiemechanisme voor  $\text{SO}_2$ , zal leiden tot een betere overeenstemming met metingen voor zowel  $\text{SO}_2$  als sulfaat. Echter met alleen oppervlakte metingen kunnen de complexe mechanismen en terugkoppelingen in de zwavelcyclus niet volledig worden getoetst. Daarom is er een duidelijke behoefte aan profielmetingen zodat begrepen kan worden wat er boven de oppervlakte- en grenslaag, waar een groot deel van het aerosol zich bevindt, gebeurt.

Voor de maand augustus 1997 zijn satellietmetingen van de aerosol optische dikte (AOD) vergeleken met berekende waarden voor Europa. Het blijkt dat gesimuleerde patronen hierin goed overeen komen met de gemeten patronen. Ongeveer 40 procent van de gemeten AOD kan verklaard worden uit de berekende aerosol hoeveelheden en de berekende wateropname door dit aerosol. Aangezien oppervlakteconcentraties van sulfaat en nitraat vrij goed overeen komen met metingen betekent dit dat ofwel de vrije troposfeer concentraties onderschat worden ofwel dat belangrijke aerosol componenten zoals mineraal en organisch aerosol meegenomen moeten worden. Uit metingen en andere studies blijkt dat het laatste in ieder geval waar is.

In dit proefschrift is aangetoond dat we door modellen en metingen te vergelijken een beter beeld krijgen van de kwaliteit van de modellen en dat we hierdoor ook meer inzicht krijgen in de relevante processen zelf. In de komende decade zullen veel metingen van de atmosferische samenstelling vanuit satellieten beschikbaar komen en zal assimilatie in chemische transport- en klimaatmodellen een steeds belangrijkere rol gaan spelen. Daarbij is het goed dat modelleers leren van de ervaring die met data-assimilatie, validatie en kwaliteitscontrole van metingen is opgedaan in numerieke weersverwachtings centra.

# Nawoord

Nog een paar dagen en dan gaat het proefschrift naar de drukker. Een mooie afsluiting van zes jaar onderzoek bij het KNMI. In het hiernavolgende wil ik een overzicht geven van deze tijd en de betrokken personen bedanken.

Eind 1993 kwam ik via een gelukkige samenloop van omstandigheden bij het Koninklijk Meteorologisch Instituut terecht. Ik werd reeds verwacht als dienstplichtige bij een tankbataljon in Amersfoort. Via Laurens Ganzeveld en Jos Lelieveld hoorde ik op de valreep dat bij het KNMI een reserve officier academisch gevormd gezocht werd om namens de luchtmacht onderzoek uit te voeren naar de effecten van vliegverkeer op de atmosfeer. Na een uniek sollicitatiegesprek bij luitenant-kolonel Verhoeven, waarbij beide sollicitanten aanwezig waren, ben ik aangenomen en snel overgeplaatst van de landmacht naar de luchtmacht. Na een verkorte militaire opleiding van 4 weken kon ik vervolgens in december naar het KNMI.

Hennie Kelder en wijlen Lodewijk Heijboer ontvingen mij met enthousiaste verhalen over “nudging” in globale circulatie modellen. Voor iemand die net afgestudeerd is aan de Landbouw Universiteit Wageningen en zich voornamelijk bezig gehouden heeft met planten en luchtverontreiniging in de grenslaag op regionale schaal, een groot onbekend gebied. Maar dankzij de deskundige begeleiding van Lodewijk had ik de materie toch redelijk snel door. Daarom is een postume dankbetuiging hiervoor op zijn plaats. Na het tragisch overlijden van Lodewijk zaten we even in een impasse, hoe nu verder met het “nudgings” project? Een bezinningsperiode volgde, gedurende welke ik kennis maakte met het TMK-model. In korte tijd heb ik hiermee simulaties van de verspreiding van aerosol afkomstig van de Pinatubo vulkaan uitbarsting uitgevoerd. Bij het werk met het TMK model en sowieso in mijn begintijd bij het KNMI heb ik veel steun gehad van Wiel Wauben, een stille, betrouwbare en efficiënte onderzoeker. Wiel Bedankt!

Toen werd weer besloten om het “nudgings” project voort te zetten met extra steun vanuit het Max Planck instituut in Hamburg. Peter Siegmund werd ook bij het project betrokken. Many times I traveled to Hamburg and each time I returned full of inspiration to continue my work. I want to thank Ulrich Schlese for his introduction to ECHAM and Hans Feichter and Lennart Bengtsson for their support and the instructive discussions. Peter Siegmund bleek een ideale begeleider. Zijn gestructureerde manier van werken, zijn heldere uitleg en duidelijke formuleringen hebben in grote mate bijgedragen aan een succesvolle afronding van het project. Ook Peter bedankt hiervoor.

Na “nudging” volgde meer data-assimilatie. Satelliet metingen van ozon zouden hiervoor gebruikt worden en een “zoom” versie van TM3, binnen een project gefinancierd door de Beleids Commissie Remote Sensing (BCRS). Het betrof een project

in samenwerking met TNO en de vakgroep luchtkwaliteit van de LUW. Met behulp van Peter van Velthoven en in goede samenwerking met Martin Heimann en Stefan Rehfeld heb ik eerst het TMK model en de meteorologische preprocessing hiervoor omgezet naar TM3. Michel Ramonet heeft me zijn versie van het “zoom” model van TM2 gegeven. Het is me echter niet gelukt om een goedlopende versie hiervan voor TM3 maken. Een project waar ik veel tijd in heb gestoken maar waar ik me uiteindelijk toch bij neer heb moeten leggen. Ook daar leer je van. Samen met kamergenoot Elias heb ik het binnen onze sectie nagenoeg onbekende terrein van data-assimilatie verkend. Een taaie tak van wetenschap! Het was dan ook niet vreemd dat we zo nu en dan moesten bijkomen van de inspanningen op onze mooie sofa. Henk Eskes, die wel wat taaie materie gewend was vanuit de vaste stof fysica, volgde Elias waardig op. Uiteindelijk zijn we er met z’n drieën in geslaagd om een goed verhaal over data-assimilatie in TM3 op te schrijven. Elias en Henk bedankt voor jullie goede samenwerking.

Als derde en laatste project heb ik gewerkt aan de modellering van aerosolen in TM3 binnen een project gefinancierd door het Nationaal Onderzoeks Programma (NOP) van het ministerie van VROM. Binnen het project is samengewerkt met het ECN, RIVM, TNO-FEL en het IMAU. Bij aanvang van dit project werd duidelijk dat het einddoel een promotie zou zijn. Veel dank ben ik verschuldigd aan mijn copromotor en geestverwant Frank Dentener. Frank, met jou hulp zijn we er uiteindelijk in geslaagd het model aanzienlijk te verbeteren. Van je kennis op het gebied van de atmosferische chemie en je praktische inzicht heb ik veel geleerd. Verder wil ik met name noemen de goede en leuke samenwerking met ook bijna doctor Laurens Ganzeveld (vriend en droge depositie expert), kersverse doctor Sander Houweling (mede TM3-pionier), Swen Metzger (mooi werk verricht op gebied van nitraat-aerosol modellering), Hans Cuijpers (voor de hulp bij het grenslaagschema), Pepijn Veefkind (aerosol-retrieval pionier) en Dominik Brunner (beiden hielden we al van Jazz, vervolgens verruimde jij mijn blikveld met Hiphop).

Mijn promotoren Hennie Kelder en Jos Lelieveld wil ik bedanken voor het in mij gestelde vertrouwen. Hennie jij hebt me alle vrijheid gegeven om onderzoek te doen en op het juiste moment heb je de regie wat strakker in handen genomen zodat ik op tijd het proefschrift kon afleveren. Jos, bij jou kon ik altijd binnen lopen om de inhoud van het onderzoek en de te volgen koers te bespreken zodat ik met een goed gevoel weer verder kon. Peter van Velthoven, begeleider en bewaker van zovele projecten binnen de sectie AS wil ik ook graag bedanken voor de betrokkenheid en begeleiding. Alle mensen die mijn concept proefschrift gelezen en becommentarieerd hebben wil ik eveneens bedanken.

Een leukere werkomgeving dan de sectie AS is moeilijk voor te stellen. Op de interessante discussies en onzinverhalen tijdens koffie en lunchpauzes kijk ik met plezier terug. Alle collega’s daarom bedankt voor jullie gezelligheid!

Tenslotte had ik dit werk nooit kunnen voltooien als ik thuis niet de nodige afleiding zou hebben gevonden. Mede dankzij jou Lian heb ik nooit enige moeite gehad om werk en privé gescheiden te houden.

# Curriculum Vitae

Ad Jeuken is geboren op 5 oktober 1968 in Venlo. In het nabij gelegen Tegelen groeide hij op. In 1987 behaalde hij het diploma gymnasium  $\beta$  aan het Collegium Marianum in Venlo. Vanaf 1987 tot 1993 volgde hij de studie Milieuhygiëne aan de Landbouw Universiteit Wageningen met als specialisatie Luchtkwaliteit en Meteorologie. Afstudeervakken werden gedaan aan achtereenvolgens de vakgroepen Luchtkwaliteit, Meteorologie en Geografische informatie systemen. In 1994 vervulde hij zijn dienstplicht als reserve officier academisch gevormd (ROAG) voor de luchtmacht bij het KNMI. Daarna heeft hij van 1995 tot en met 1999 als projectmedewerker op verschillende projecten gewerkt bij de sectie Atmosferische samenstelling binnen de afdeling Klimaat onderzoek en Seismologie van het KNMI. Aan de faculteit Technische Natuurkunde van de Technische Universiteit Eindhoven heeft hij begin 2000 zijn proefschrift kunnen afronden.